UNIVERSITAT POLITÈCNICA DE VALÈNCIA

Departamento de Máquinas y Motores Térmicos
and
von Karman Institute for Fluid Dynamics

DOCTORAL THESIS:

"Experimental Aerothermal Performance of Turbofan Bypass Flow Heat Exchangers"

Author: Dña. Laura Villafañe
Supervisors: Dr. D. José María Desantes
Dr. D. Guillermo Paniagua

Valencia, December 2013

DOCTORAL THESIS

"Experimental Aerothermal Performance of Turbofan Bypass Flow Heat Exchangers"

AUTHORS

Written by: Dña. Laura Villafañe
Supervised by: Dr. D. José María Desantes
Dr. D. Guillermo Paniagua

DEFENSE COMMITTEE

Chairman: Dr. D. Jose Ramón Serrano
Members: Dr. D. Damian Vogt
Dr. D. Jean-François Cori

DISSERTATION READERS

Dr. D. Giacomo Persico
Dr. D. Juan Pedro Solano
Dr. D. Damian Vogt

Abstract

The path to future aero-engines with more efficient engine architectures requires advanced thermal management technologies to handle the demand of refrigeration and lubrication. Oil systems, holding a double function as lubricant and coolant circuits, require supplemental cooling sources to the conventional fuel based cooling systems as the current oil thermal capacity becomes saturated with future engine developments. The present research focuses on air/oil coolers, which geometrical characteristics and location are designed to minimize aerodynamic effects while maximizing the thermal exchange. The heat exchangers composed of parallel fins are integrated at the inner wall of the secondary duct of a turbofan. The analysis of the interaction between the three-dimensional high velocity bypass flow and the heat exchangers is essential to evaluate and optimize the aero-thermodynamic performances, and to provide data for engine modeling. The objectives of this research are the development of engine testing methods alternative to flight testing, and the characterization of the aerothermal behavior of different finned heat exchanger configurations.

A new blow-down wind tunnel test facility was specifically designed to replicate the engine bypass flow in the region of the splitter. The annular sector type test section consists on a complex 3D geometry, as a result of three dimensional numerical flow simulations. The flow evolves over the splitter duplicated at real scale, guided by helicoidally shaped lateral walls. The development of measurement techniques for the present application involved the design of instrumentation, testing procedures and data reduction methods. Detailed studies were focused on multi-hole and fine wire thermocouple probes.

Two types of test campaigns were performed dedicated to: flow measurements along the test section for different test configurations, i.e. in the absence of heat exchangers and in the presence of different heat exchanger geometries, and heat transfer measurements on the heat exchanger. As a result contours of flow velocity, angular distributions, total and static pressures, temperatures and turbulence intensities, at different bypass duct axial positions, as well as wall pressures along the test section, were obtained. The analysis of the flow development along the test section allowed the understanding of the different flow behaviors for each test configuration. Comparison of flow variables at each measurement plane permitted quantifying and contrasting the different flow disturbances. Detailed analyses of the flow downstream of the heat exchangers were assessed to characterize the flow in the fins' wake region. The aerodynamic performance of each heat exchanger configuration was evaluated in terms of non dimensional pressure losses. Fins convective heat transfer characteristics were derived from the infrared fin surface temperature measurements through a new methodology based on inverse heat transfer methods coupled with conductive heat

flux models. The experimental characterization permitted to evaluate the cooling capacity of the investigated type of heat exchangers for the design operational conditions. Finally, the thermal efficiency of the heat exchanger at different points of the flight envelope during a typical commercial mission was estimated by extrapolating the convective properties of the flow to flight conditions.

Resumen

En el ámbito del transporte comercial aéreo, los avances en turbofanes de alta relación de derivación están dirigidos a la disminución del consumo específico y peso de motor, y a la reducción de las emisiones de sustancias contaminantes y acústicas. Para alcanzar dichos objetivos nuevos diseños están enfocados a incrementar las eficiencias propulsivas y del ciclo térmico, así como a desarrollar sistemas de gestión térmica y subsistemas de motor más eficientes. El desarrollo de sistemas avanzados de gestión térmica es esencial para cubrir la alta demanda de refrigeración y lubricación a la que los sistemas de aceite están sometidos. La capacidad térmica de los sistemas de aceite en los motores de aviación actuales está limitada principalmente por la máxima temperatura del combustible, fuente primaria de evacuación de la carga térmica. Nuevos desarrollos de motor están asociados a arquitecturas con alta complejidad mecánica, y al incremento de sistemas eléctricos y automáticos, causando un aumento de las fuentes de calor y la necesidad de lubricación. Al mismo tiempo, la incorporación de materiales compuestos limita la máxima temperatura del combustible y su capacidad térmica. Por tanto, el desarrollo de sistemas que aumenten la evacuación de calor del sistema de aceite es imperativo para la evolución de este tipo de motores.

En la presente investigación se propone el uso de intercambiadores de calor aire/aceite integrados en la superficie interior del conducto del flujo secundario (splitter), diseñados para minimizar la resistencia aerodinámica al mismo tiempo que maximizar el intercambio de calor. Los intercambiadores de calor propuestos están formados por aletas orientadas en la dirección del flujo, y su diseño es compatible con las nuevas arquitecturas de motor investigadas para la mejora de la eficiencia. El análisis de la interacción entre el flujo transónico y tridimensional en el conducto secundario del motor y los intercambiadores de calor es esencial para evaluar su comportamiento y desarrollar modelos optimizados. No existen trabajos previos que hayan planteado la utilización de intercambiadores de calor en flujos a alta velocidad, o el estudio detallado del flujo secundario en turbofanes.

Dos son los objetivos principales de esta investigación: el diseño de procedimientos de ensayo para el estudio del flujo secundario en turbofanes, y el análisis del flujo y su interacción con diferentes geometrías de intercambiadores de calor de aletas

Se ha diseñado un banco de ensayos que reproduce el flujo secundario en el punto de diseño aerodinámico: condiciones de flujo de crucero (velocidades transónicas) en tierra (condiciones atmosféricas). El nuevo túnel de viento se caracteriza por una sección de ensayos tridimensional de tipo sector anular cuyo diseño ha sido basado en simulaciones numéricas 3D. Igualmente se han desarrollado diferentes técnicas de medida optimizadas para esta aplicación que permiten caracterizar el comportamiento aero-térmico con precisión.

Dos tipos de ensayos fueron realizados: dirigidos a la caracterización del

flujo en la presencia de diferentes geometrías de intercambiadores, y orientados a la caracterización térmica de las aletas. Con el fin de entender el comportamiento del flujo y cuantificar las perturbaciones creadas por las diferentes configuraciones, se han realizado medidas de las variables fluidas en diferentes secciones a lo largo de la sección de ensayos tanto en la configuración convencional (sin intercambiadores), como en la presencia de intercambiadores. Las alteraciones del flujo introducidas por las diferentes geometrías fueron cuantificadas en términos de velocidad y dirección de flujo, turbulencia, y temperatura, así como su efecto en las distribuciones de presión a lo largo de la superficie del splitter. El comportamiento aerodinámico de los diferentes intercambiadores fue caracterizado mediante distribuciones de coeficientes de pérdida de presión, derivados de balances a la entrada y salida de las aletas. Las características adiabáticas de transferencia de calor del tipo de intercambiador investigado fueron derivadas de los resultados experimentales de termografía infrarroja mediante una nueva metodología basada en métodos inversos de transferencia de calor. Basándose en estos resultados, la capacidad de evacuación de calor del intercambiador fue analizada para diferentes condiciones de vuelo en una misión típica.

Resum

En l'àmbit del transport aeri comercial, els avanços en turbofans d'alta relació de derivació estan orientats a la disminució del consum específic i pes de motor, i a la reducció de les emissions de substàncies contaminants i acústiques. Per tal d'aconseguir aquests objectius, nous dissenys estan enfocats a incrementar les eficiències propulsives i del cicle tèrmic, així com a desenvolupar sistemes de gestió tèrmica i subsistemes de motor més eficients. El desenvolupament de sistemes avançats de gestió tèrmica és essencial per a cobrir l'alta demanda de refrigeració i lubricació a la qual els sistemes d'oli estan sotmesos. La capacitat tèrmica dels sistemes de lubricació en els motors d'aviació actuals està principalment limitada per la màxima temperatura del combustible, font primària d'evacuació de la càrrega tèrmica. Nous desenvolupaments de motor estan associats a arquitectures d'alta complexitat mecànica, i al increment de sistemes elèctrics i automàtics, provocant un augment de les fonts de calor i la necessitat de lubricació. Al mateix temps, la incorporació de compòsits limita la màxima temperatura del combustible i la seua capacitat tèrmica. Per tant, el desenvolupament de sistemes que augmenten l'evacuació de calor del sistema d'oli és imperatiu per a l'evolució d'aquest tipus de motors.

En la present recerca es proposa l'ús de bescanviadors de calor aire/oli integrats en la superfície interior del conducte del flux secundari (splitter), dissenyats per a minimitzar la resistència aerodinàmica, al temps que maximitzen l'intercanvi de calor. Els bescanviadors de calor proposats estan formats per aletes orientades en la direcció del flux, i el seu disseny és compatible amb les noves arquitectures de motor investigades per a la millora de l'eficiència. L'anàlisi de la interacció entre el flux transsònic i tridimensional en el conducte secundari del motor i els bescanviadors de calor és essencial per a avaluar el seu comportament i desenvolupar models optimitzats. No existeixen treballs previs que hagen plantejat l'ús de bescanviadors de calor en fluxos a alta velocitat, o l'estudi detallat del flux secundari en turbofans.

Dos són els objectius principals d'aquesta investigació: el disseny dels procediments d'assaig per a l'estudi del flux secundari en turbofans, l'anàlisi del flux i la seua interacció amb diferents geometries de bescanviadors de calor d'aletes.

S'ha dissenyat un banc d'assajos que reprodueix el flux secundari en el punt de disseny aerodinàmic: condicions de flux de creuer (velocitats transsòniques) a terra (condicions atmosfèriques). El nou túnel de vent es caracteritza per una secció d'assajos tridimensional del tipus sector anullar, el disseny del qual ha sigut basat en simulacions numèriques 3D. Així mateix, s'han desenvolupat diferents tècniques de mesura optimitzades per a aquesta aplicació, que permeten caracteritzar el comportament aero-tèrmic amb precisió.

Dos tipus d'assajos foren realitzats: dirigits a la caracterització del flux

en la presència de diferents geometries de bescanviadors, i orientats a la caracterització tèrmica de les aletes. Amb la finalitat d'entendre el comportament del flux i quantificar les pertorbacions creades per les diferents configuracions, s'han realitzat mesures de les variables fluïdes en diferents seccions al llarg de la secció d'assajos tant en la configuració convencional (sense bescanviadors), com en la presència de bescanviadors. Les alteracions del flux introduïdes per les diferents geometries foren quantificades en termes de velocitat i direcció de flux, turbulència, i temperatura, així com el seu efecte en les diferents distribucions de pressió al llarg de la superfície del splitter. El comportament aerodinàmic dels diferents bescanviadors va ser caracteritzat mitjançant distribucions de coeficients de pèrdua de pressió, derivats de balanços a l'entrada i a l'eixida de les aletes. Les característiques adiabàtiques de transferència de calor del flux del tipus de bescanviador investigat foren derivades dels resultats experimentals de termografia infraroja mitjançant una nova metodologia basada en mètodes inversos de transferència de calor. Basant-se en aquests resultats, la capacitat d'evacuació de calor del bescanviador va ser analitzada per a diferents condicions de vol en una missió típica.

Contents

Nomenclature

Roman Symbols

A	area	[m^2]
cp	five-hole probe pressure coefficient	
C_p	isobaric specific heat	[$Jkg^{-1}K^{-1}$]
d	diameter	[m]
h	convective heat transfer coefficient	[$Wm^{-2}K^{-1}$]
h_{ad}	adiabatic convective heat transfer coefficient	[$Wm^{-2}K^{-1}$]
k	thermal conductivity	[$Wm^{-1}K^{-1}$]
l	wire length (junction to support)	[m]
l_c	$\sqrt{k_w d_w / 4h}$ reference wire length	[m]
M	Mach number	
$\dot{m}$	mass flow rate	[kg s^{-1}]
Nu	Nusselt number	
P	pressure	[Pa]
Q	heat flux	[Wm^{-2}]
R	specific gas constant of air	[J kg^{-1} K^{-1}]
R	radius	[m]
Re	Reynolds number	
r	regression coefficient	
r	radius	[m]
r_a	adiabatic recovery factor	
S	transversal area	[m^2]
T	temperature	[K]
t	time	[s]
V	absolute flow speed	[ms^{-1}]
V	volume	[m^3]
x	axial coordinate	[m]
x'	local coordinate, perpendicular to stem axis	[m]
Y	temperature	[K]
y	normal coordinate (wire direction, fin height)	[m]
y'	local coordinate, stem axis	[m]
z	axial coordinate	[m]
z	complex frequency	
Z	overall recovery factor	
Z_a	overall adiabatic recovery factor	

Greek Symbols

α	yaw angle	[degrees]
β	pitch angle	[degrees]
ε	threshold	
γ	specific heat ratio	
μ	dynamic viscosity	[Pa·s]
σ	standard deviation	
ϕ	diameter	
ϕ	probe rotation around the stem axis	[degrees]
ρ	density	[kgm^{-3}]
τ	characteristic time constant	[s]
φ	probe rotation around the test section axis	[degrees]

Subscript

ad	non dimensional quantity
ad	adiabatic
atm	atmospheric conditions
ave	averaged
aw	adiabatic wall
d	deposit
f	fin, final
fp	flow-probe axes
fg	flow-global axes
i	index of five-hole probe (1-5)
i	initial conditions
in	inlet
in	internal
is	isentropic
j	junction
ref	reference value
s	static quantity
sc	settling chamber
sp	support
t	total quantity
ts	test section
v	valve
w	wall, wire
0	total quantity
∞	free stream conditions

Acronyms

ACOC	Air Cooled Oil Cooler
AD	Adiabatic
BPR	Bypass Ratio
CHT	Conjugate Heat Transfer
DAQ	Data Acquisition System
IGV	Inlet Guide Vanes
IHCM	Inverse Heat Conduction Method
ISO	Isothermal
LE	Leading Edge
MP	Measurement Plane
SFC	Specific Fuel Consumption
TE	Trailing Edge
TU	Turbulence Intensity
VKI	von Karman Institute for Fluid Dynamics

Chapter 1

Introduction

High bypass ratio turbofan engines are the preferred solution in medium to long range civil aircrafts for the next decades. Developments are motivated by the reduction of burned fuel per unit payload and the stringent limitations on noise and air pollution. The path to future aero-engines with improved specific fuel consumption (SFC) and weight, requires improvements in thermal and propulsive efficiencies, along with advanced thermal management solutions and system developments.

Efforts to increase thermal efficiencies are directed to reduce the cooling air bled from the compressor and to improved materials. Minor improvements can be obtained by further increasing pressure ratios and burner exit temperatures, or component efficiencies, without modifying the thermodynamic cycle [1, 2]. The addition of a recuperator enhances the fuel efficiency by using part of the exhaust gasses' energy to heat the flow prior to the combustor. An intercooler lowers the amount of power needed in the compression system by reducing the core flow temperature. Both technologies, used in land based gas turbines, are under research in aircraft applications [3–6]. The SFC improvement through propulsive efficiency is linked with the increase of bypass ratio and simultaneous reduction in the outer fan pressure ratio. However difficulties arise with the implicit increase of engine diameter, drag, and weight. Different turbofan engine architectures are considered, namely mixed or separate flow turbofans; conventional or geared turbofans. The arguments for the design selection must account for the particular aircraft mission. Geared turbofans are attractive for bypass ratios larger than 11, allowing to reduce the number of low pressure turbine stages, hence the engine weight, at the expenses of introducing an additional gear box. For bypass ratios larger than 16-18 unducted engine architectures with counter-rotating propellers are under development.

1.1 Heat exchangers for high-bypass turbofan engines

Advanced thermal management solutions are of particular relevance to cope with the increasing cooling and lubrication demands. Independently of the cooling by high pressure air bled from the compressor, the oil system is responsible of cooling and lubricating mechanical components such as bear-

ings, gears and carbon seals, and cooling of electronic devices such as generators, electric motors and power electronics. Oil systems also hold the functions of damping bearings reducing vibrational energy, limiting friction between solids, and providing hydraulic energy for actuation systems and pressurized fluid for meters. Efficient oil heat removal is essential to ensure the oil system operation during the different temperature conditions encountered during the flight mission. Fuel is the primary heat sink for the lubrication oil, but also for the hydraulic and integrated drive generator (IDG) oil systems. Different designs of aero-engine oil cooling circuits are described by Linke-Diesinger [7]. Fuel/oil heat exchangers are more compact than air/oil, do not cause particular integration problems, no drag increase and no aerodynamic engine performance loss. However the capacity of the fuel as a heat sink is temperature limited, and additional air/oil heat exchangers are generally included to complement fuel/oil coolers. Actual air/oil heat exchangers (plate or tube types) involve adverse effects on the engine performances when driven by bleed air or fan airstream, or result in increased drag in the case they are installed in the nacelle. To prevent fuel degradation, vapor locking within the fuel pump as well as combustion instabilities, air is required as an additional heat sink during certain engine operations. Improvements in the oil system could diminish the demand of fuel cooling and reduce the adverse effects of existent air/oil heat exchangers. Those improvements are imperative as the current oil thermal capacity becomes saturated in future engine developments. Engine architectures with increasing bypass ratios tend to raise the mechanical complexity by introducing additional transmission components, or through more compact gas generators. This yields to higher oil lubrication and cooling demands, and augmented solicitations for oil heat removal. The oil heat loads tend also to be increased given the growing importance of electronic devices and automated controls within the engine systems [8, 9]. Additionally, the integration of lighter composite materials on the wings skin, with lower temperature limits and heat conductivity, further limits the fuel heat removal through convective cooling, thus its contribution to the fuel/oil heat exchange.

The present research focuses on air/oil coolers, which geometrical characteristics and location within the engine are designed to minimize aerodynamic effects while maximizing thermal exchange. Air Cooled Oil Coolers (ACOC) composed of parallel fins are integrated at the inner wall of the secondary duct of a turbofan, downstream of the core/bypass splitter nose, as displayed in Fig. 1.1. This heat exchanger configuration introduces less aerodynamic perturbations than current plate/tubes heat exchanger modules. The proposed oil heat removal alternative can be coupled with the engine architectures under development like intercooler and recuperators, geared turbofans and unducted engines. The analysis of the interaction between the three dimensional high velocity bypass flow and the heat exchangers is essential to evaluate and optimize the aero-thermodynamic performances, and to provide data for engine modeling. The present inves-

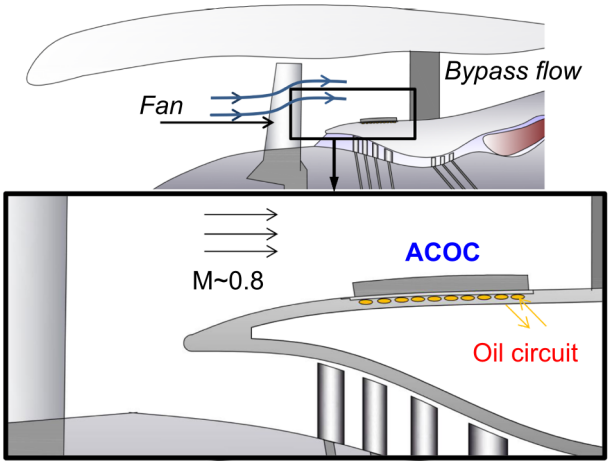

Figure 1.1: *Air Cooled Oil Cooler location within the turbofan bypass duct.*

tigation is directly related to three research topics: thermal management systems, turbofan bypass flows, and forced convection on heat exchangers in high velocity flows.

1.2 Objectives of the work

The development of integrated thermal management systems is a main subject for air vehicle designers. A general discussion on the interaction and heat generation mechanisms of fuel and oil systems has been presented by Streifinger [10]. Investigations on oil system's architectures and on the development of new components to improve the efficiency of oil systems have been carried out at MTU Aero Engines [11] in the framework of European and German funded projects.

Public research on turbofan bypass flows is scarce and no data is available regarding aerodynamic performances of bypass duct geometries. Investigations addressing the impact of outlet guide vanes and exhaust nozzle geometries on inlet fan performances and acoustic effects have been carried out at NASA Glenn Research Center [12, 13]. Few works have presented numerical calculations including bypass flow modeling with the purpose of predicting engine performances [14] and analyzing fan/splitter flow interaction effects on core and bypass flows [15].

The literature is also scarce on heat transfer and aerodynamic effects on heat exchangers at high Reynolds and high Mach number flows. By contrast, multiple studies have been focused on the performance and optimization of heat exchangers at low Reynolds and Mach numbers with applications on industrial, electronic or internal cooling systems. Most of the works deal

with fully shrouded heat sinks, optimizing the geometry of the fins and the arrays. Sparrow and Grannis [16, 17], presented investigations on diamond-shaped pin fin arrays, Metzger et al.[18] on oblong fins at various angles of attack, Ota and Nishiyama [19] , and Li et al. [20] provided results on elliptical fins, and Chen et al.[21] on drop-shaped pin fins. Heat sinks in ducted flows with tip and/or lateral clearances have been thoroughly researched for electronic applications. The effect of tip and lateral bypass on pressure drops and thermal performances of plate fin and pin heat sinks has been addressed by Sparrow and Beckey [22] and Lee et al. [23] among others. Numerically, the ability of methods to predict the bypass performance has also been examined. Many authors have worked on the development of correlations [24, 25] and analytical models [26–28]. However, an analytical model is not yet available to be used in an optimization procedure for heat sink design, and each different design and test case requires dedicated experimental and numerical evaluation. Even though the utilization of air heat exchangers in high Reynolds number flows, and particularly within the fan airstream in turbofans, has not been subjected to public investigation, several patents [29–36] have proposed their implementation in similar contexts.

The present work studies the aerothermal behavior of different geometries of finned air/oil heat exchangers within an engine representative bypass flow environment. Two main objectives have been pursued within this investigation:

- the development of engine testing methods alternative to flight testing,
- the analysis of the transonic bypass flow interaction with finned heat exchanger geometries.

Besides the growing power of Computational Fluid Dynamics (CFD) tools and the cost reduction involved by their introduction in the engine design process, experimental test data continues being the fundamental data source for new technologies and novel aerodynamic developments, for the understanding of complex flows, for validation of CFD methods and tools, as well as for final product certification. Furthermore, the behavior of complex flows and of integrated component systems is essentially characterized by performance maps and correlations derived from experimental data. However, flight testing is expensive and the development of alternative testing methodologies able to provide engine representative results at a reduced cost is crucial. In this context, a key objective of the present work was the **development of an experimental approach able to reproduce the engine bypass flow environment representative of the most critical conditions for the ACOCs under investigation**. It corresponds, both for the aerodynamic flow effects and for the oil heat loads, to cruise flow velocities and take off (zero altitude) ambient conditions. The precise duplication of the flow structure is essential to address the aerodynamic and

heat transfer phenomena. The reproduction of the three-dimensional transonic bypass flow, characterized by swirl angles ranging between 40 and 50 degrees, as it evolves over the splitter duplicated at real scale, makes the new ground testing environment a unique substitute to flight experiments.

The understanding of the bypass flow behavior in the presence of arrays of fins is of main importance to develop efficient heat exchangers to improve the oil system capabilities causing minimum aerodynamic penalties. **Evaluation of the global and local flow modifications introduced by different finned heat exchanger geometries is targeted for a better understanding of the flow-fins interaction.** Quantification of the aerodynamic and thermal performances with respect to the conventional bypass flow without heat exchangers was intended in order to evaluate the potential of the investigated cooling solution. Pressure loss balances contain information of the magnitude of the flow disturbances , and can be used to estimate global effects on the engine performances. To analyze the thermal capabilities, the experimental determination of the convective heat transfer characteristics should be addressed. This information should be combined with conductive heat transfer models on the heat exchanger, to evaluate the cooling capabilities and to estimate the sensitivity of the heat exchanger to other operational points within an aircraft flight envelope.

1.3 Research methodology

The research approach for the present work consisted of three successive steps: design and development of the experimental tools, test, and data analysis.

From the definition of the target research model and engine operational conditions, the design comprised the development of a test rig and optimized measurement techniques for the type of flow under investigation. The investigated region of the turbofan bypass duct is comprised between the fan trailing edge and the leading edge of the outlet guide vanes. Interest was focused on the precise flow duplication, allowing engine representative aerodynamic and thermal measurements. The design methodology for the development of a new wind tunnel comprised different phases, from the conceptual wind tunnel design based on analytical modeling, trough schematic zero-dimensional modeling, to the detailed component design assisted by 2D and 3D numerical computations. In particular, the test section design was optimized through iterative 3D Navier Stokes flow simulations to ensure the matching between the test section flow and the bypass flow. The final test section design consists in a complex helicoidal geometry in which the flow is guided by 3D shaped walls.

The development of measurement techniques involved works on the specific design of instrumentation, testing procedures and data reduction methods. The design of tools and experimental procedures was dictated by the

requirements of the flow phenomena to be characterized, with the constrains imposed by the wind tunnel geometrical and operating characteristics. The influence of blockage effects was studied through numerical computations. Detailed studies were focused on multi-hole and fine wire thermocouple probes. The data reduction methodology used to compute flow variables from the five-hole probe is of main importance to the accuracy of the results. The characterization of the five-hole probe included the evaluation of the different error sources and the global uncertainty associated to the measurements. The design of high accuracy thermocouple probes requires the understanding of the heat transfer processes within the probe, for each particular application and probe design, and precise probe characterizations. A numerical procedure outperforming previous experimental approaches was proposed to analyze thermocouple responses and to evaluate the contribution of the individual error sources to the global error on the temperature readings. It is based on conjugate heat transfer simulations. Its capabilities were analyzed based on the fine wire shielded thermocouple design developed for the present work. Finally, a new methodology based on numerical inverse heat transfer methods coupled with conductive heat flux models was applied to determine the convective heat transfer characteristics of the heat exchanger, from surface temperature measurements. Infrared imaging was used to provide the surface temperature data.

Experimental procedures were designed for two types of test campaigns, dedicated to:

- flow measurements along the test section for different test configurations, i.e. in the absence of heat exchangers, and in the presence of different heat exchanger geometries,
- heat transfer measurements on the heat exchanger.

For both types of tests the wind tunnel was operated at nominal conditions, providing a steady flow during the blow-down time. To evaluate the flow evolution along the test section, five measurement planes at different axial positions upstream and downstream of the location of the heat exchangers were defined. A single blow-down test was required to obtain contour measurements at one axial position, with one type of probe and one test configuration. Extensive testing was required given the number of measurement planes, probes, and test configurations. This type of tests included also wall pressure measurements along the midline of the test section channel and circumferentially at the location of the measurement planes. An automated control system was designed to synchronize different data acquisition systems and a two axis traverse mechanism responsible of the instrumentation displacement within the measurement planes. The objective of the second type of tests was to record the surface temperature evolution of the heat exchanger as it was cooled down by the transonic flow at steady conditions. In order to increase the accuracy of the convective heat transfer calculations,

interest was focused on maximizing the temperature gradient on the array of fins. For this purpose the fins were heated up to high temperatures in the absence of flow, the initial transient during the wind tunnel start was minimized and the surface temperature evolution was recorded in the absence of external input power.

The analysis of the large amount of experimental data required the development of specific post-processing tools, in order to obtain from each test set of data the correspondent flow variable contour. Data processing tools included coordinate systems transformations, spatial interpolation routines and area averaging procedures within the distorted measurement planes. Data processing methodologies for the thermal tests included coupling of a minimization technique based on conjugate gradient methods, with a 3D conduction solver, through an iterative procedure. As a result contours of flow velocity, angular distributions, total and static pressures, temperatures and turbulence intensities, at different bypass duct axial positions, as well as wall pressures along the test section were obtained. The analysis of the flow evolution along the different measurement planes allowed the understanding of the different flow behaviors for each test configuration. Comparison of flow variables at each measurement plane permitted quantifying and contrasting the different flow disturbances. Area average balances between different planes were assessed to evaluate the aerodynamic performance of each heat exchanger configuration in terms of non dimensional pressure losses. The convective heat transfer characteristic derived from the experiments permitted to evaluate the cooling capacity of the investigated type of heat exchangers for the design operational conditions. The three dimensional conduction within the heat exchanger model was numerically solved for this purpose. Finally, by scaling the convective properties of the flow to the characteristics of the bypass flow environment during a typical commercial aircraft mission, the thermal efficiency of the heat exchanger at different points of the flight envelope was predicted. The extrapolation was based on turbulent Nusselt correlations, and results from a turbofan engine model.

1.4 Thesis outline

The description of the work and research results are organized in five chapters:

The first chapter explores the current developments under research on the field of engines for commercial aircrafts of mid-large range, and defines the motivation of the present work within that framework. The main objectives of the research activity are presented and the research approach driving the investigation is introduced.

The second chapter describes the design of a new wind tunnel that replicates the flow conditions encountered in a turbofan bypass duct at the

aerodesign operational conditions. The criteria leading the design are analyzed and the different design phases and tools employed described.

In the third chapter attention is paid to the development of measurement techniques, and in particular to multi-hole and fine wire thermocouple probes. Five-hole probes design considerations, sensitivity to flow orientation, data reduction methodologies and measurement procedures within the environment of this research are presented. A new procedure based on conjugate heat transfer simulations to analyze thermocouple responses and to evaluate the influence of the different error sources for a given design is described. The uncertainties associated to the current measurements for both probes are discussed, as well as an overview of the design considerations for intrusive instrumentation.

The fourth chapter describes the experimental and data reduction procedures. It addresses separately the tools and methodologies applied for the thermal and aerodynamic test campaigns.

Results are presented in the fifth chapter. The characteristics of the flow along the test section and its interaction with the heat exchangers are analyzed. Thermal results are presented characterizing the convective heat transfer between the flow and the arrays of fins. Finally in this chapter, the aerodynamic and thermal implications of this type of heat exchangers in turbofan engines are evaluated.

The main conclusions of the current investigation are discussed in the last chapter.

Chapter 2

Bypass flow channel facility

The aim of a wind tunnel design is to provide an airstream flowing under the required controlled conditions, so that the subject of interest can be experimentally addressed within the test section. High speed wind tunnels are often of the intermittent type given the large power and setting time requirements involved in continuous wind tunnels when high compression ratios are required. With the development of high frequency sensors, intermittent wind tunnels became an alternative to long testing operation.

The test section design is determined by the flow phenomena under investigation. Systematic research in several simplified test sections allows to identify the different relevant mechanisms driving an aerothermal phenomena. Linear cascades are common due to their simplicity, flexibility and clean optical path. However, they do not permit the reproduction of the radial equilibrium laws on axial engines. Such economic solution, usually combined with large models, represents the first degree of sophistication. The single component can then be coupled with generators of thermal fields, unsteadiness, or other upstream flow effects at a reduced cost. Annular test sections enable the simulation of the engine radial pressure gradients fundamental to reproduce secondary flows, and the investigation of components in rotation; hence centrifugal and coriolis forces can be reproduced. An important distinction between linear and annular cascades is that in annular test sections a fully periodic environment is easily achieved. A compromise solution, that combines advantages of linear and annular test sections, is the annular sector geometry, allowing the simulation of engine representative flow fields at lower testing costs. Nevertheless it is relatively uncommon due to design challenges. Annular sector cascades have been used in the past in heat transfer and film cooling investigations in HP turbine vanes, as described by Gladden and Gauntner [37]. Another example of an existing annular sector cascade is the facility developed at KTH (Wiers and Fransson [38–40]) to study airfoil film cooling. Vogt and Fransson [41] applied also annular sector cascade testing to aeromechanical research by employing semi-flexible inlet and outlet ducting sidewalls which allowed some controlled deformation in order to maintain the periodicity and radial pressure gradients established in the test section. A different approach to establish the back pressure boundary conditions in the test section on a transonic annular cascade was employed by Povey et al. [42], for assessing turbine cooling system performances [43]. They developed an annular sector cascade of high pressure

turbine vanes, where flow conditioning was achieved by an annular sector of deswirl vanes downstream of the test section. The periodic transonic flow was demonstrated by comparison with results from an equivalent fully annular cascade.

In the present investigation the three dimensional nature of the bypass flow in the region of the air splitter nose imposes the necessity of duplicating radial and axial flow gradients for an accurate investigation on the heat exchanger aero-thermodynamic performances. Thus an annular sector type test section was designed. The uniqueness of the present test section with respect to the few existing annular sector facilities lies in the significantly larger dimensions of the research domain. The three dimensional flow is to be duplicated along a certain axial length simulating the flow downstream of the inlet fan, the bifurcation core/bypass flow, and the bypass flow development over the splitter. This requirement adds further complexity to the commonly addressed difficulties on the design of annular sector test sections, primarily azimuthal periodicity, and deswirl or flow evacuation respecting test section flow distributions.

Design considerations and methodology are described in this section. The final design consists on an intermittent facility of helicoidally shaped test section. Distorted annular sectors define the transversal sections of the 3D geometry, along a length six times larger than the characteristic transversal dimension. The flow downstream of the engine fan is reproduced at the entrance of the test section by means of an array of airfoils. Numerical flow analyses were used to guide the design of the complete wind tunnel. Zero-dimensional models were developed to recreate the wind tunnel behavior on the initial design stages. Two and three dimensional computations were performed to optimize the test section and the inlet guide vanes.

2.1 Design considerations

Figure 2.1-a displays the region of the turbofan under investigation. It is the portion of the engine comprised between the fan trailing edge and the leading edge of the outlet guide vanes. The air flow conditions to be reproduced corresponded to the aerodesign point: cruise operation at sea level pressure and temperature. The flow characteristics along the region of interest were known from a calibrated non viscous through-flow computation of the real engine.

Four control planes were defined within the research domain to assist the comparison of engine/test section numerical flow results during the design. They are indicated in Fig. 2.1-b. The heat exchanger is integrated on the splitter surface in the region bounded by planes P3 and P4. Thus, correct flow reproduction is of main importance in those regions. Planes P1 and P2 were set right downstream of the fan and upstream of the splitter nose respectively. They were essential to ensure downstream of the wind tun-

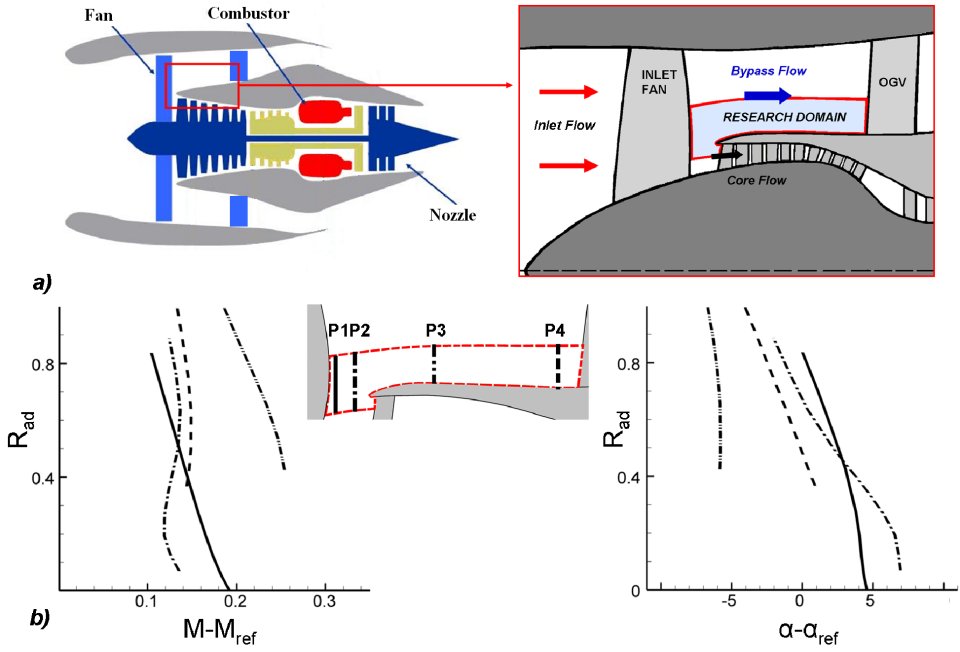

Figure 2.1: *a) Heat exchanger location and research domain. b) Radial Mach number and flow angle distributions from through-flow computations on a calibrated engine model.*

nel inlet vanes the replication of the mean flow distributions downstream of the inlet fan (P1), and the flow effects at the bifurcation core/bypass (P2). Radial distributions in terms of Mach number and flow angle at the four control planes are shown in Fig. 2.1-b. Table 2.1 indicates the variation of static temperature and pressure, Mach number and flow angle along the radial direction at the location of plane P1. The maximum variation of Mach number within the domain is ΔM=0.22, and Reynolds numbers based on a standard heat exchanger fin height of 15 mm vary between $2.7{\cdot}10^5$ and $3{\cdot}10^5$.

$\Delta T_s\%$	$\Delta P_s\%$	$\Delta M\%$	$\Delta\alpha\%$
3	13	11	10

Table 2.1: *Maximum radial variations of flow properties downstream of inlet fan, from through-flow computations on a calibrated engine model.*

The aim of the present wind tunnel design was to reproduce the required flow test conditions characterizing the engine bypass flow within the test

section, i.e. Reynolds number, Mach number, turbulence intensity and flow angles. General wind tunnel design rules are given by reference textbooks on experimental aerodynamics [44–46] and technical reports [47–49]. Along with flow requisites, test rigs ought to minimize power consumption, manufacturing and life costs of components, as well as space required for the installation. Furthermore, the wind tunnel should provide stable conditions during the test duration and minimize installation effects such as end-wall effects.

A blowdown type wind tunnel was preferred for the present application. It is driven by a pressurized storage of 72 m^3 at 40 bar and ambient temperature. The compliance of the following flow requisites guided the wind tunnel design:

- Mach and Reynolds number effects play a dominant role for assessing the heat exchanger performances at the transonic engine bypass flow conditions

- Downstream of the inlet fan the tangential flow velocity is of the same order of magnitude as the axial component. Moreover variations of flow angle and Mach number along the radial direction are comparable to those encountered along the axial bypass flow evolution, as depicted in Fig. 2.1. Radial velocity components are not negligible within the studied region. Surface heat transfer rate distributions are strongly influenced by secondary flows driven by radial gradients. Under those considerations, the replication of three dimensional effects is of main importance.

- The heat exchanger is integrated in the splitter surface. The boundary layer developing from the splitter nose requires to be duplicated in order to study the aerodynamic perturbations introduced.

The three dimensional flow effects are replicated thanks to an optimized test section geometry. The overall wind tunnel configuration was justified by the following considerations:

- The operational Mach number can be kept stable within a test through the control of the total to static pressure ratio by means of an inlet pressure regulation valve.

- Reynolds numbers can be reproduced during the blowdown without the need of inlet temperature control mechanisms. Maximum variations of Reynolds number were estimated lower than 25% for a test duration about six minutes.

- Flow conditions at the test section are dependant on the exhaust architecture. The installation of an efficient deswirl duct and diffuser

downstream of the test section is preferred to the utilization of a second throat. It reduces the exhaust pressure losses and ensures the preservation of the required radial and azimuthal profiles within the test section.

- Maximization of testing times is desired for detailed map measurements. Test durations in an intermittent facility are determined by the operational flow conditions, the air storage characteristics, the transversal dimensions of the wind tunnel components, the pressure losses along the system and the exhaust pressure.

- Turbulence intensity and homogeneity of test section inlet flow are imposed by an appropriate settling chamber design and selection of series of screens and honeycombs.

2.2 Wind tunnel design

2.2.1 Design methodology

The design process evolved through different phases starting by the conceptual wind tunnel sketch definition. Simplified governing equations of the main components were first used to analyze the temporal evolution of the flow parameters along the wind tunnel using estimative dimensions and safety coefficients. Schematic modeling of the facility was performed using Ecosimpro mathematical tool in combination with the ESPSS libraries [50]. Zero dimensional modeling allowed predefining characteristic components dimensions as a compromise with testing time. It served to validate the feasibility of the installation, to analyze the temporal evolution of the flow variables in the different components, and to study their sensitivity to geometrical changes and estimated losses.

The next step consisted in the detailed component design. It can be divided in three blocks: settling chamber, test section, and exhaust. Flow distributions at the test section inlet depend on the settling chamber and intermediate contraction design. A set of inlet profiles (Inlet Guide Vanes, IGVs) was designed to reproduce at the inlet of the test section the flow downstream of the engine fan. Hub and casing test section end-walls were optimized through axisymmetric computations. The last step of the test section design was the definition of the lateral walls. They were defined with the help of 3D computational tools. Numerical tools guided also the design of the exhaust, consisting on a vaneless deswirl stage followed by a straight diffuser of rectangular transversal section. Mechanical design followed the aerodynamic conception ensuring the structural resistance but also test section accessibility and modularity.

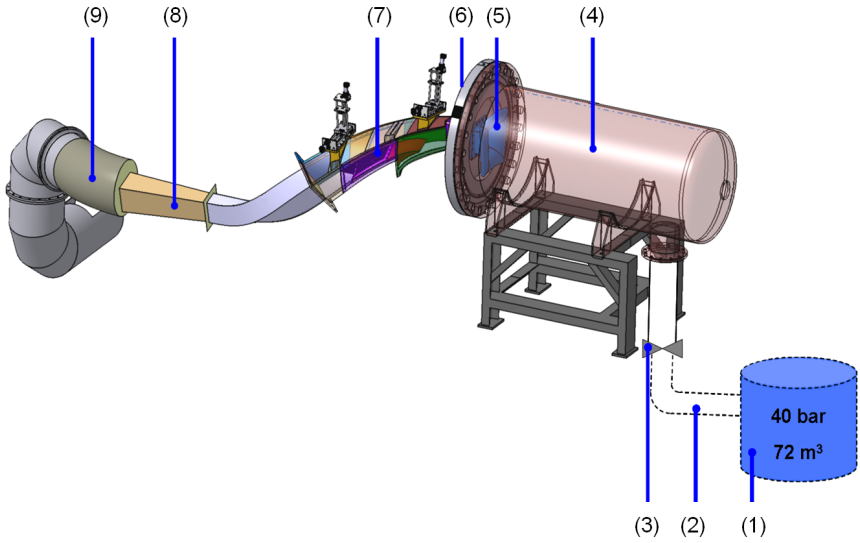

Figure 2.2: *Wind tunnel sketch.*

2.2.2 Blow-down wind tunnel model

A schematic representation of the wind tunnel is shown in Fig. 2.2. It is driven by compressed air from a 72 m^3 tank (1) initially at 40 bar and ambient temperature, guided along a high pressure line (2) to the settling chamber (4). A control pressure valve (3) between tank and settling chamber is operated to keep the Mach number in the test section constant. The turbulence intensity of the flow is established in the settling chamber by the selected series of screens and honeycombs. Grid selection is treated in detail in a number of technical reports [51–53]. From the settling chamber the air is first accelerated in a contraction (5), which also increases the uniformity of the flow and decreases the turbulence in longitudinal direction. The Inlet Guide Vanes (6) turn and accelerate the flow to reproduce the radial distributions of Mach number and flow angle downstream of the engine fan. Downstream, the flow evolves along the three-dimensional test section (7), where it is bifurcated into core and bypass flow at the splitter leading edge. The air under the splitter is evacuated through a variable area restriction, allowing the control of the mass flow and hence the pressure distribution around the stagnation nose. The main bypass flow is straightened in a deswirl duct, later expanded in a diffuser (8) and exhausted through the discharge circuit (9) to the atmosphere.

The regulation valve between the storage tank and the settling chamber allows to keep the desired Mach number during the test when it is progressively opened at the correct rate. If it is held fixed, the wind tunnel

stagnation pressure drops as the pressure in the storage tank decreases.

A simplified mathematical model describing the temporal evolution of the thermodynamic variables within the wind tunnel can be written considering two control volumes: the air storage tank and the settling chamber. Let us assume that:

(a) Thermodynamic processes are isentropic.

(b) Air is a perfect gas.

(c) Pressure and temperature in the storage tank are uniform

(d) The discharge is an adiabatic process (fast discharge) without heat exchange.

(e) The energy loss through the control valve is negligible.

Under these hypotheses the conservation of mass and the conservation of energy are expressed by Eqs. 2.1.

$$\frac{d\rho_d}{dt} = -\frac{1}{V_d}\dot{m}_v \qquad \text{and} \qquad \frac{dP_d}{dt} = -\gamma\frac{R}{V_d}\dot{m}_v T_d \tag{2.1}$$

The mass flow rate across the valve depends on the valve position. Above a tank to settling chamber pressure ratio the flow in the valve remains chocked. For the chocked condition the mass flow rate across the valve is given by Eq. 2.2.

$$\dot{m}_v{}^* = \left(\frac{2}{\gamma+1}\right)^{\frac{\gamma+1}{2(\gamma-1)}}\sqrt{\gamma P_d \rho_d}A_v(t) \tag{2.2}$$

The air flows then into the settling chamber and is subsequently vented into the test section through a contraction. Conservation of mass and energy equations yields:

$$\frac{d\rho_{sc}}{dt} = \frac{1}{V_{sc}}(\dot{m}_v - \dot{m}_{ts}) \tag{2.3}$$

$$\frac{dP_{sc}}{dt} = \gamma\frac{R}{V_{sc}}(\dot{m}_v T_d - \dot{m}_{ts}T_{ts}) \quad \text{with } T_d = T_{ts}, \quad \frac{dP_{sc}}{dt} = \gamma\frac{RT_d}{V_{sc}}(\dot{m}_v - \dot{m}_{ts}) \tag{2.4}$$

Neglecting pressure losses and heat transfer, total quantities in the test section are equivalent to the data in the settling chamber. The mass flow into the test section can be expressed in function of the reference area, the pressure and the temperature in the settling chamber and the static pressure

in the test section, by means of a reference Mach number, Eq. 2.5.

$$\dot{m}_{ts} = \sqrt{\gamma P_{sc} \rho_{sc}} A_{ts} M (1 + \frac{\gamma - 1}{2} M^2)^{-\frac{\gamma+1}{2(\gamma-1)}} \quad \text{and} \quad M = \sqrt{\frac{2}{\gamma - 1}[(\frac{P_{sc}}{p_{ts}})^{\frac{\gamma-1}{\gamma}} - 1]} \tag{2.5}$$

Equations 2.1 and 2.4 become three first order non linear ordinary differential equations in three state variables P_d, ρ_d, and P_{sc}. The inputs to this system are the reference test section Mach number, the valve position A_v and the static pressure in the test section (function of the diffuser efficiency and exhaust losses). The temporal law of the valve position that closes the system of equations can be mathematically determined adding a control system.

This simplified model helps the analysis of the wind tunnel behavior. During a tunnel run and vessel discharge the stagnation temperature decreases due to the expansion of air. Tests last until the pressure in the tank decreases to the value that unchocks the regulating valve.

2.2.3 Component sizing

The transversal area of the test section was a compromise between test duration (limited by compressed air tank capacity) and the convenience of big areas to reduce the influence of wall and instrumentation blockage effects. From Eq. 2.5 a maximum critical area of 0.021 m^2 was fixed considering engine flow specifications, safety coefficients, and a maximum mass flow rate of 6 kg/s.

Zero dimensional schematic models were programmed in order to check the validity of the design, to refine the characteristic dimensions, and to analyze the sensitivity of the thermodynamic variables to geometrical characteristics and pressure losses. A proportional-integral-derivative (PID) control system was included to keep constant the ratio total to static pressure in the test section. The constants of the controller were tuned manually. The mathematical tool used is Ecosimpro simulation tool in combination with the ESPSS libraries [50].

Two models were used depending on the control strategy and the variables of interest. The one represented in Fig. 2.3 is based on the control of the isentropic Mach number in the test section. It includes the air bifurcation within the test section to the correspondent discharge circuits. A simpler one eluding the consideration of two flow streams was also modeled based on the control of the isentropic Mach number upstream of the IGVs. Once the later is calibrated it is most suitable for wind tunnel control analyses, avoiding the complexity of the former one with more parameters to be tuned.

Results obtained from the model sketched in Fig.2.3 are represented in Fig. 2.4. Particularly, temporal evolutions of non dimensional valve aperture, Mach number and static pressure at different wind tunnel locations, and test section Reynolds number variation (based on a heat exchanger fin height

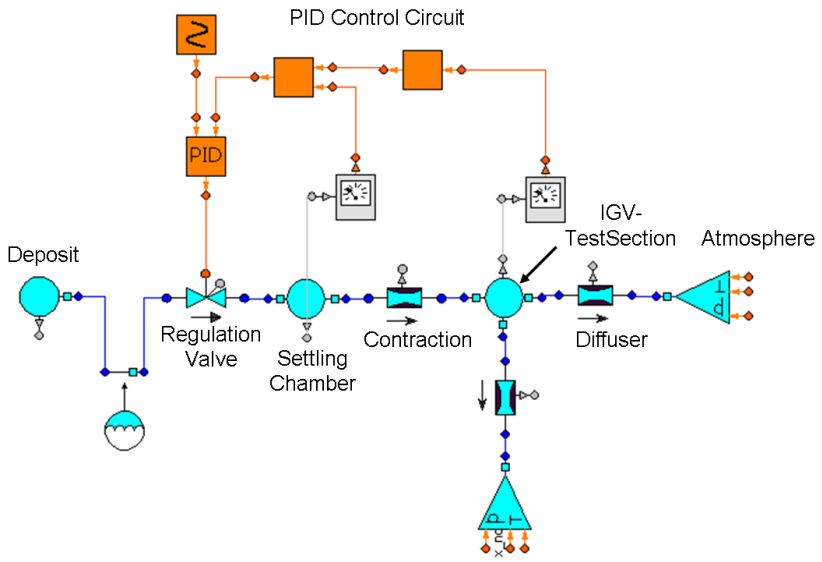

Figure 2.3: *Schematic model for the control of M_{is} within the test section.*

of 15 mm). The static pressure and Mach number are shown to remain constant in time while the aperture of the valve is able to keep the pressure ratio imposed. The Reynolds number increases with the continuous decay of temperature, proportionally to $(\mu\sqrt{T_s})^{-1}$. The evolution of the test section Reynolds number is plotted during the first six minutes, which was the estimated test duration, resulting in an approximate change of 24%. The mass flow in the test section increases with time proportionally to $(\sqrt{T_s})^{-1}$. Variations of pressure levels, and hence the test duration, accounting for valve and duct losses were analyzed. In agreement with Fung and Ray [54] the optimum PID constants for each condition were found to vary slightly. Constant values can be taken without penalizing significantly the control process.

2.3 Aerodynamic design and test section optimization

An helicoidally shaped test section was designed to duplicate the three dimensional turbofan bypass flow. Numerical simulations were used for its aerodynamic optimization through different design phases. The final configuration is sketched in Fig.2.5 where the real geometry of the splitter separating engine core and bypass flow is included. The 3D test section channel

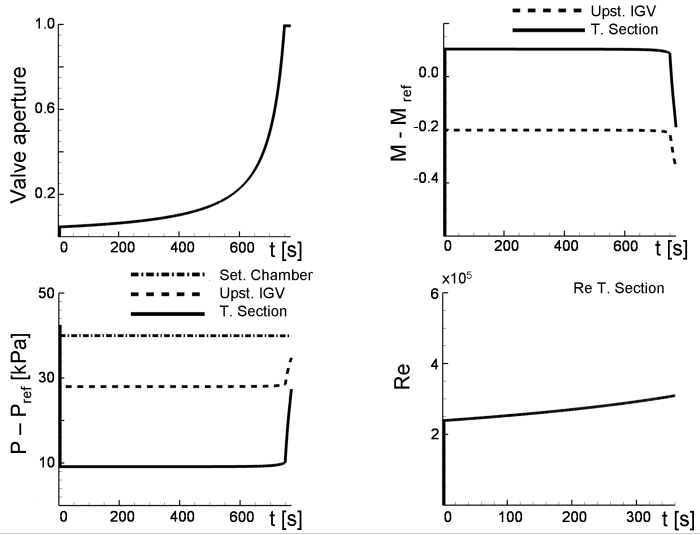

Figure 2.4: *Computed temporal evolution of static pressure, Mach number, valve position and Reynolds number.*

is defined by transversal distorted annular sectors turning around the engine axis.

Boundary conditions for the numerical flow simulations were imposed in terms of total pressure and temperature at the inlet of the domains and static pressures at the outlet section, such as to match the target flow velocities. Since the test section static pressures are dependent on the exhaust recovery, sensitivity analysis were performed for different inlet/outlet pressure boundary conditions.

2.3.1 Inlet Guide Vanes

The time averaged radial flow distributions of Mach number and flow angle encountered downstream of the engine inlet fan are replicated at the test section inlet by a set of inlet guide vanes placed downstream of the contraction following the settling chamber. The design of the IGVs [55] followed various steps starting from 2D airfoil profile optimizations, from which also the optimum pitch to chord ratio was defined. This was followed by iterative 3D numerical flow simulations, performed for the optimization of the 3D airfoils required to match the engine flow distributions. Different sets of 3D vanes were modeled considering in each case a different axial chord value, and thus a different number of airfoils within a fixed angular sector. Compromise between manufacturing complexity and wakes homogenization length imposed the airfoil size.

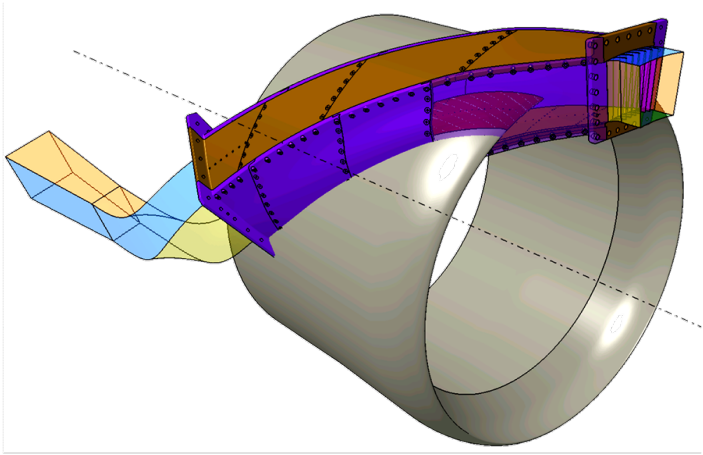

Figure 2.5: *Test section flow duct sketch.*

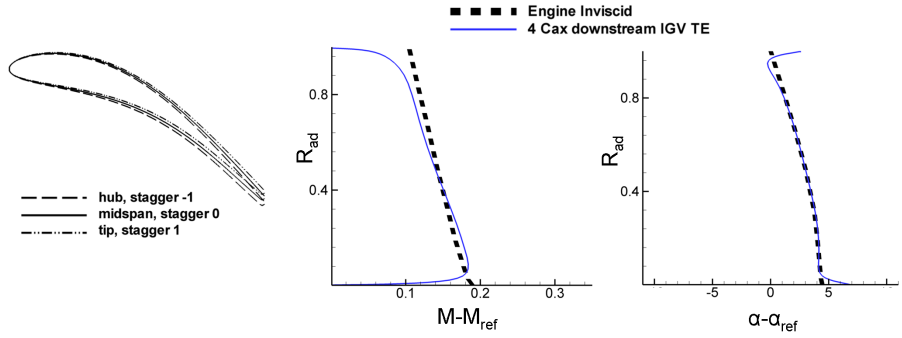

Figure 2.6: *Mach number and flow angle distributions downstream IGVs.*

The final configuration is an array of airfoils of 26 mm axial chord stacked along the leading edge, defining 7 flow passages. The stagger angle of the airfoils varies linearly from hub to tip by 2 degrees. The aspect ratio of the airfoils (h/c_{ax}) is 5.5. Radial variations of Mach number and flow angle downstream of the IGVs are plotted in Fig. 2.6 in non dimensional coordinates.

2.3.2 End-wall design

The definition of the upper and inner walls radius along the axial direction is conditioned by the duplication of the real splitter geometry, the maximum transversal area, and the interest on maximizing the main stream by-pass

flow. The initial end-wall geometry was based on flow streamlines derived from through-flow computations on the real engine. FINE/turbo software (Numeca International ©) was used to perform axisymmetric computations of the flow-field within a domain limited by the hub and casing end-walls including both the main bypass flow channel and the inner flow under the splitter. The distance between the IGVs trailing edge and the axial location of the splitter leading edge was fixed by the convenience of short test section lengths while ensuring the effective dissipation of the inlet wakes in the main bypass-flow. Iterative modifications on the axisymmetric domain including the IGVs were performed in order to find the optimum limiting walls to reproduce the required Mach number and flow angle evolutions. Special interest was focused on reproducing the flow conditions in the region of the heat exchanger.

2.3.3 Lateral walls

In order to reproduce the axial gradients and the azimuthal periodicity, the lateral walls should not induce external forces to the flow. The importance of the lateral walls design is accentuated by the high flow velocities and the large test section length (ratio test section axial length to characteristic transversal dimension larger than 6).

Upstream of the IGVs a 15 deg. annular sector defines the transversal section of the test section inlet. Along the bypass duct three different lateral walls configurations were considered accounting for the engine bypass flow reproduction as well as for the feasibility and manufacturing complexity. To facilitate the understanding, in the following the end-walls are considered as two concentric cylinders (axial radius variation is not considered).

Option a) The intersection lateral walls/concentric cylinders is defined by four cylindrical helices of equal pitch. The geometry of the transversal sections at different axial positions is the same but rotated. The angle helix/generatrix is smaller in the inner than in the outer cylinder. However the flow angle in the engine is lower close to the external wall than to the internal wall. Therefore this option was rejected.

Option b) The intersection of lateral walls/concentric cylinders is defined by four cylindrical helices with different pitches over the internal and external cylinders, but constant angle helices/generatrix. The flow is driven by walls that form a constant angle with the axial direction at different radial and axial positions.

Option c) The lateral walls are defined as flow stream-surfaces extracted from the axisymmetric computation on the domain delimited by the end-walls. The flow angle is respected at all locations and the forces introduced to the flow minimized. It entails the biggest manufacturing complexity.

Numerical flow simulations on the domains defined from options *b* and *c* were performed using FINE/turbo (Numeca International ©) solver. The computational domain includes the IGVs block and the test section, comprising an axial length of 0.9 meters. Computations have been performed considering adiabatic walls and fully turbulent flow. The Spalart-Allmaras turbulence model was considered. Values of y^+ were about 6. The grids used were about 20 million points, with higher mesh density in azimuthal direction to reproduce the wake effects downstream of the IGVs. Convergences were achieved after 1000 iterations, 80 hours CPU time in an Intel Core 2 Quad Q9400 (2.66 GHz) machine.

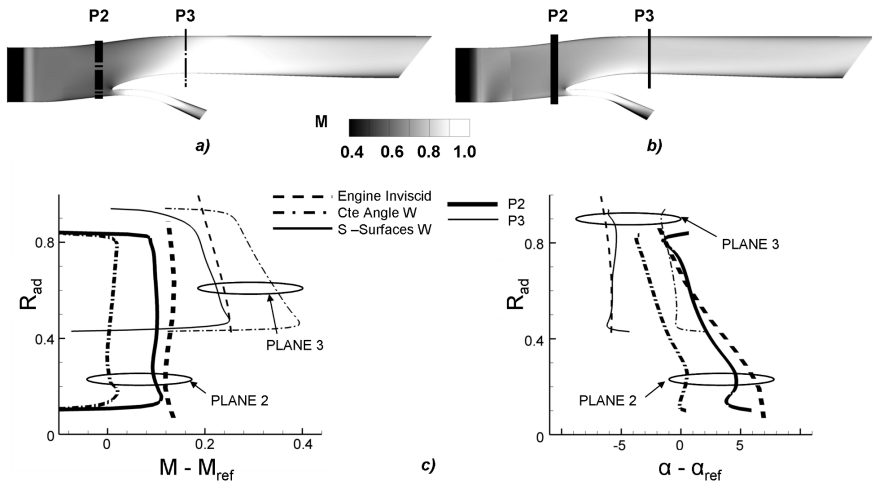

Figure 2.7: *Meridional Mach number contours: a) Constant angle walls, b) Streamsurfaces walls. c) Radial Mach number and flow angle distributions at control planes P2 and P3 from engine Through-flow Computations (dash line), constant angle walls TS configuration (dot-dash line), streamsurfaces walls TS configuration (solid line).*

Meridional Mach number contour plots for both geometries (lateral walls options *b* and *c*) are shown in Fig. 2.7. Non dimensional radial Mach number and angle distributions at design control planes P2 and P3 are plotted for both configurations and the flow engine data. In the case of lateral walls defined as flow streamsurfaces the flow is accelerated up to P3 (right upstream the location of the heat exchanger leading edge) to the same Mach number as in the engine flow, and the flow velocity is slightly lower at P2. In both planes the angle distributions match the engine conditions. For the case of lateral walls defined by constant angle helices (option *b*) the flow is over accelerated in plane P3 by 15% and over decelerated about 17% in plane P2. Angular distributions are also significantly different from the

engine data.

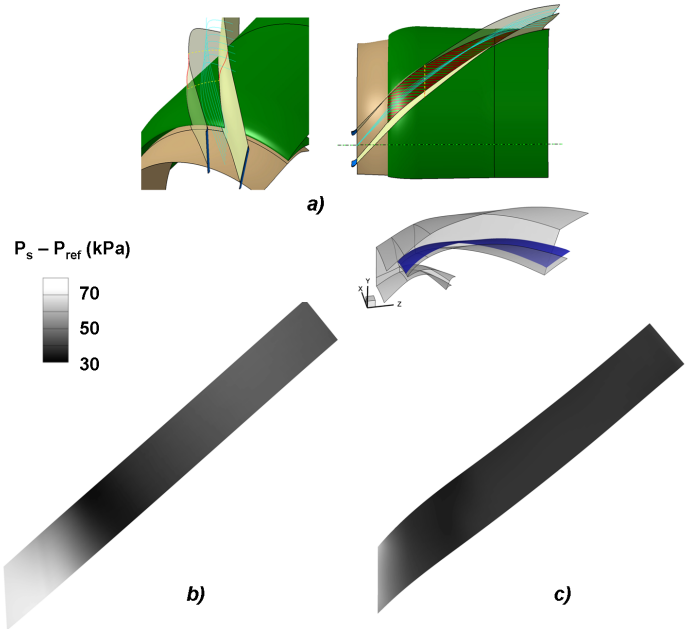

Figure 2.8: *a)Streamsurfaces as lateral walls. Static pressure contours over a streamsurface approximatively 15 mm over the splitter: b) Constant angle walls, c) Streamsurfaces walls.*

Static pressure contours on a surface parallel to the splitter at 15 mm are represented in Fig. 2.8 for configurations *b* and *c*. At a given axial position circumferential gradients are observed in the flow-field established within the constant angle geometry, while axisymmetry is observed for the curved walls.

In agreement with those results lateral walls were defined as flow streamsurfaces to better reproduce the real engine bypass-flow. Transversal sections at constant axial positions along the test section resulted in distorted angular sectors.

2.3.4 Exhaust section.

Given the high bypass flow swirl and flow velocities, the reproduction of the flow distributions for which the test section was optimized depended on the design of the discharge circuit downstream of the test section. Separation on the discharge circuit can influence the upstream flow by introducing blockage or unsteadiness. Two possibilities were considered and numerically modeled: direct evacuation to a dump-tank, and the use of a deswirl duct and diffuser.

The dump-tank was discarded given the high mass flows to be evacuated, the waste of opportunity for pressure recovery, and the installation complexities implied. Furthermore, also when the flow is exhausted to a constant pressure plenum, attention has to be paid to avoid separation of the hub boundary layer due to the adverse pressure gradient in account of the radial pressure gradient of the swirling flow. The design of the deswirl block and diffuser was carried out to minimize any effect on the test section distributions, and to achieve high recovery factors, while respecting ergonomic criteria. High recovery factors are directly related with pressure losses minimization along the exhaust. They imply lower test section static pressure levels and consequently require lower inlet total pressures, and longer test durations. The use of airfoils within the deswirl [42] was not considered due to the increase of losses that it would imply, and blockage effects.

The design of the exhaust circuit was assisted by iterative numerical flow simulations of the complete domain test section plus exhaust circuit. Along the deswirl duct the flow is brought back to axial and slightly decelerated. It is followed by an adaptation block characterized by an annular sector inlet geometry and rectangular transversal section at its outlet while maintaining the transversal area. The axial length of the deswirl plus adaptation block is 0.85 m (similar to that of the test section). Downstream, a double plane divergence diffuser of 0.7 m decelerates the flow prior to its discharge to a circular pipe of 0.5 m diameter which finally directs the low velocity flow to the atmosphere. Guidelines on diffuser optimization assisted the design [46, 56, 57].

2.4 Mechanical design and manufacturing

The mechanical design of the test section and exhaust system is sketched in Fig. 2.9. A modular design provided manufacturing and test section accessibility advantages, at the cost of increased design complexity. The 3D shaped pieces conforming the external radius test section wall are interchangeable with pieces with the same flow surface geometry but allocating the instrumentation carriages supports for intrusive flow measurements at different transversal planes along the test section. The test section modularity was essential for accessibility for heat exchanger model replacement, and application of surface flow visualization techniques.

Transparent walls were designed to permit flow optical access. Different materials and manufacturing possibilities were evaluated that could provide accurate three dimensional surface reproduction, structural resistivity to normal and tangential loads and optical transparency. The adopted solution consisted on 3D pieces manufactured by rapid prototyping from a liquid resin. The thickness of the walls was fixed on 16.5 mm from load analysis on the final modular test section design to ensure the absence of deformation under critical loads. Stereolithography (SLA) technologies were used based

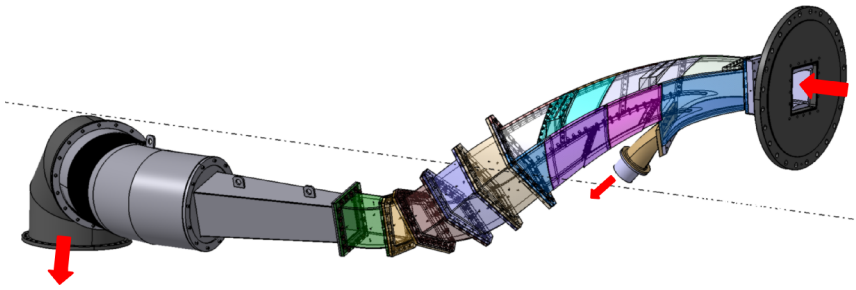

Figure 2.9: *Sketch of wind tunnel mechanical design.*

on the resin WaterShed® XC11122. Water clear characteristics (Fig. 2.10-(a)) were obtained after thermal treatment and polishing processes. Fig 2.10-(b) and 2.10-(c) shows wall sections before and after the application of finishing treatments.

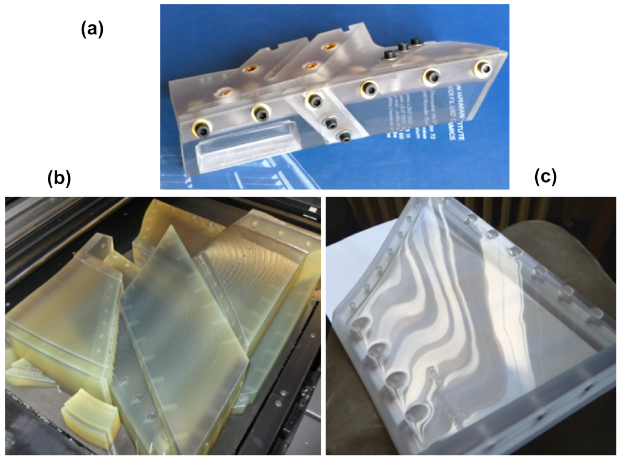

Figure 2.10: *Wall sections (a) Prove of water clear transparency, (b) wall sections without finishing processes, (c) wall section after thermal treatment and polishing*

Two flat (2D) optical accesses of 37.5 mm diameter, were included in additional test section wall pieces in the top and lateral walls to allow infrared and accurate optical measurements without the need of 3D corrections. Germanium and plexiglass window inserts were used.

The test section inlet contraction and set of inlet guide vanes are pictured in Fig. 2.11a. Optical transparency was not required in the deswirl duct, thus a different resin was used for the SLA manufacturing, Fig.2.11b.

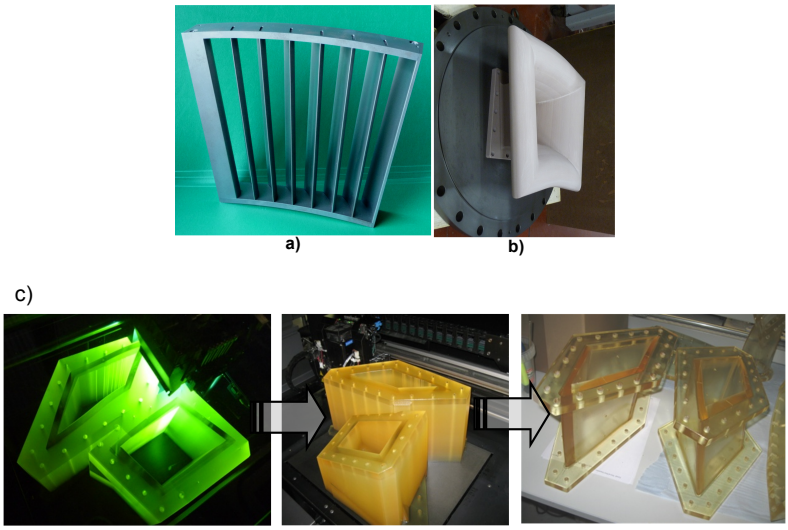

Figure 2.11: *a)Inlet Guide Vanes, b)Inlet contraction, c)Deswirl manufacturing stages.*

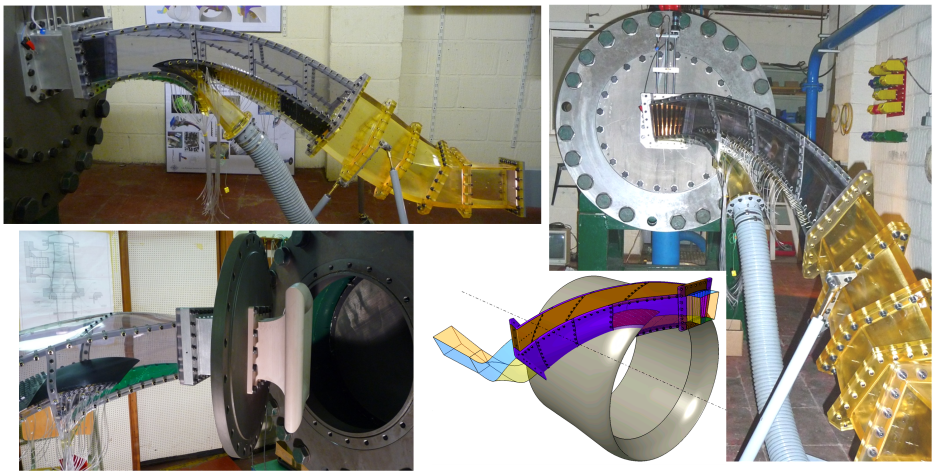

Figure 2.12: *Different views of the turbofan bypass flow transonic facility.*

Different views of the wind tunnel assembly are represented in Fig. 2.12.

2.5 Wind tunnel performance

The operation of the wind tunnel is controlled through the inlet valve regulating the mass flow entering the settling chamber, and consequently the pressure at the settling chamber. The Mach number along the test section depends on the ratio settling chamber to exhaust atmospheric pressure. This dependance is function of the diffuser performance and the pressure losses along the facility, which vary with the flow conditions. Thus the wind tunnel required to be calibrated in order to determine the ratio settling chamber to atmospheric pressure correspondent to the design operational conditions.

Calibration tests were performed in the absence of the finned heat exchanger investigated. The control parameter was defined as the settling chamber pressure and nominal flow conditions were defined such that the Mach number was 0.8 at a reference location: 45 mm in axial direction upstream the heat exchanger. Combined Pitot/thermocouple probes were placed simultaneously at the test section inlet and at the reference location. Total and wall pressures were recorded for different ratios settling chamber to atmospheric pressure. Figure 2.13 depicts the Mach number evolution at both locations for increasing settling chamber pressures.

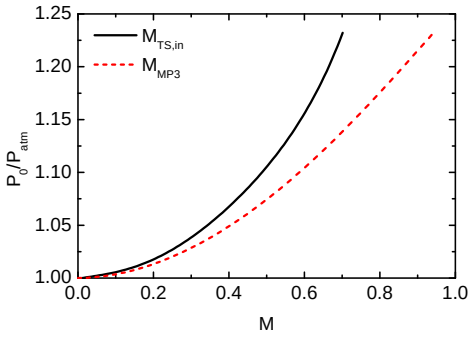

Figure 2.13: *Required control pressure ratio in function of Mach number at TS inlet and at reference location.*

During a nominal test the control valve was operated to keep constant the pressure at the settling chamber, and thus, also the Mach number at a given position. Tests were initiated by a short transient from the initial test section atmospheric pressure until the predefined target pressure was reached. The target pressure was determined by the daily atmospheric pressure and the pressure ratio derived from the calibration tests. Figure 2.14 represents the evolution of pressure ratios, Mach numbers, inlet total temperature and Reynolds number based on the standard fins height (15 mm) during a test. In Fig.2.14a the temporal evolution of the ratio settling chamber to atmospheric pressure is represented together with the ratio inlet

static to atmospheric pressure. The correspondent Mach evolutions at the test section inlet and at the reference position defined for the calibration tests, are shown in Fig.2.14b. At constant pressure and Mach number, the evolution of the Reynolds number (Fig.2.14d) is dictated by the temperature evolution (Fig.2.14c). The maximum duration of a test was limited by the capacity of the pressurized storage tank. For a test initiated with the tank at 40 bars, the maximum test duration was about 7-8 min.

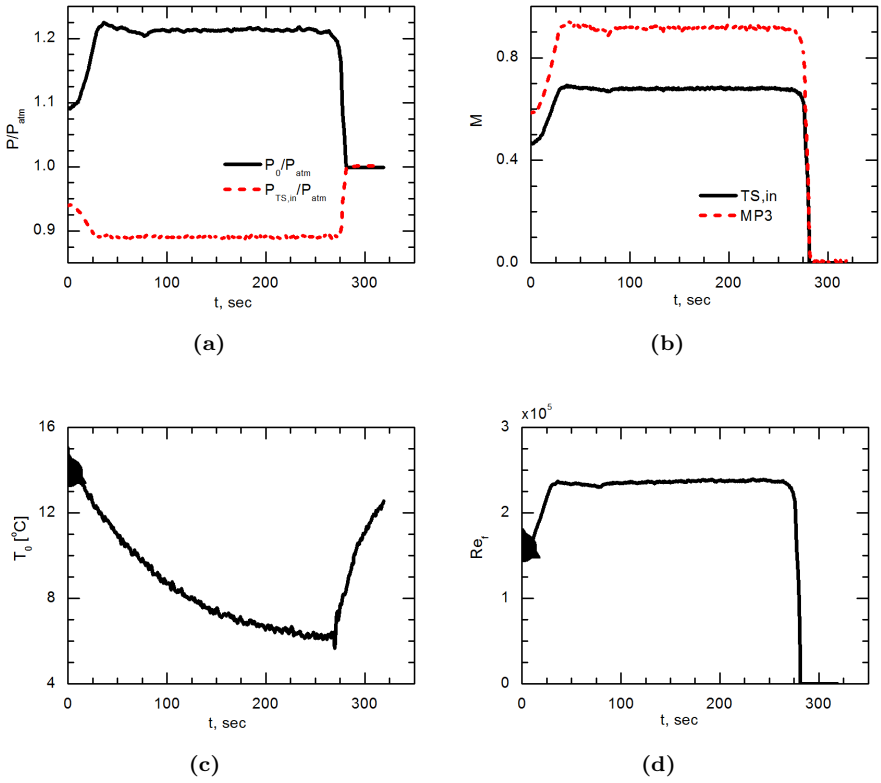

Figure 2.14: *Characteristic pressure ratios, Mach numbers, inlet temperature and Reynolds number evolution during a test.*

Repeatability of nominal test flow conditions was ensured within 1 % in terms of inlet Mach number. The flow was discharged from a tank at ambient temperature conditions equipped with a dryer system. In the absence of temperature control mechanisms the flow temperature and its variation during a test was dictated by the flow expansion in the tank, but also affected by flow dissipative effects along the pressure line guiding the air to the test section, and by its thermal interaction with the surroundings. The

test case shown in Fig.2.14 was chosen as representative of the maximum temperature variations experienced in the facility, as obtained in a cold day during the calibration tests. The test campaigns performed during a warm period showed inlet temperature variations lower than 4 degrees.

Chapter 3

Development of measurement techniques

The characterization of the interaction between the transonic bypass flow and the surface heat exchanger geometries was performed experimentally using several measurement techniques. The transonic and 3D flow environment, together with the complex test section geometry and the operational characteristics of the wind tunnel, makes the measurements of the heat exchanger performances a challenging task. The different measurement techniques had to cope with an intermittent flow, with a relatively short testing time, and involving an initial flow transient until steady flow conditions were achieved. The confined flow behavior was analyzed by means of intrusive aerodynamic probes, thin-wire thermocouples, hot-wires and wall pressure measurements. Instrumentation, measurement procedures and testing, and postprocessing methodologies, were specifically developed within this investigation, with particular attention on multi-hole probes and fine wire thermocouples.

3.1 Multi-hole probes

Multi-hole probes are extensively used to measure flow direction due to their robustness, simplicity and reduced cost when compared with other intrusive techniques as hot-wire anemometers, or non intrusive techniques as laser Doppler anemometry (LDA). Hot-wires are much more susceptible to foreign particle contamination. The impact of dust particles in the sensors can lead to a change in their sensitivity or even breakage. When compared to LDA, pressure probes are much cheaper, easier to manipulate and to implement in a test rig, and provide higher signal to noise ratio. Moreover, multi-hole probes provide not only information on the flow direction, but also static and total pressures and thus, flow velocities. The main constrain related to the use of pressure based directional probes appears if high frequency measurements are required. In the case quasi-steady measurements are intended, as it is the case of the present investigation, multi-hole probes become the best alternative.

Numerous authors have reported works related with the multi-hole technology during the last decades, addressing the effects of probe design, data processing methodologies and calibration techniques. The best probe design, and experimental and processing methodologies, depend on the particular

flow characteristics and test rig, and requires to be carefully addressed.

3.1.1 Design considerations

The design in the present application was driven by objectives common to the complete set of aerodynamic instrumentation, combined with specific considerations for the directional probes. The main requisites for the multi-hole probe head design were: probe miniaturization to reduce flow effects and to increase spacial resolution, wide angle operational range, flow angle sensitivity, and short response times.

The progress on the miniaturization of pressure transducers allows implementing pressure sensors directly at the measurement location in the probe head, thus increasing the frequency response of the probe. However, when fast response is not a requisite, the location of the pressure sensors far from the probe head permits reducing the its size and the fragility of such kind of directional probes. Although short response time was required to increase the measurement points within a test run in this investigation, high frequency responses were not aimed for pressure measurements. Thus the pressure transducers were located outside the test section. Flexible plastic tubes of different diameters were used from the probe head (0.3-0.4 mm ϕ_{in}), through the rake stem (0.6 mm ϕ_{in}), and to the transducers ports (1.1 ϕ_{in}). The time response obtained through this configuration, dependent on the tube arrangement and length, was confirmed to be satisfactory for the testing methodology.

Non-dimensional coefficients are defined in any kind of multi-hole probe to relate the pressures measured by the different sensing holes in order to correlate the probe calibrations to the pressures measured during a test. Different definitions of the coefficients are used by different authors. Whatever the definition, the geometry of the probe head should procure, in the angular range of operation, the highest pressure-coefficient sensitivity to angle variation, and the lowest dependence between pressure coefficients in order to obtain the best accuracy of the measurements.

Bryer and Pankhurst [58] provided a wide overview analyzing different probes for the investigation of three-dimensional flows. The effects of several five-hole probe tip shapes at different velocities were classified by Dominy and Hodson [59]. Conical heads with forward facing tubes are really common due to their easy manufacturing, however they present several drawbacks among which can be highlighted the dependence between the pressure coefficients computed from the pressure measurements. Gaillard [60] analyzed the influence of the cone angle on five-hole conical probes with perpendicular holes, for different Mach numbers. Comparison between conical and hemispherical head shapes was addressed by Mukhopadhya et al. [61], concluding that the angle sensitivity is higher for the hemispherical head. Houtman and Bannink [62] also compared conical and hemispherical head geometries, and recommended the use of the hemispherical heads in

transonic flows due to the smooth variation of the surface pressures with the variation of Mach number. The direction of the holes drilled on the probe head is another design parameter. Holes perpendicular to the head surface are recommended for increasing the angular sensitivity and reducing the sensitivity to Reynolds numbers [59, 63].

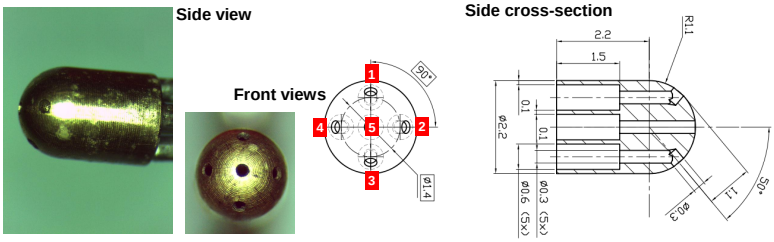

Figure 3.1: *Design of the hemispherical 5 hole probe head and hole number location.*

For the characterization of the 3D transonic bypass-flow, an hemispherical five-hole probe head was selected based on literature results, but also based on the comparison of experimental angular sensitivity analysis performed within this investigation on a conical and an hemispherical probe heads. The geometric characteristics of the designed five-hole probe head are displayed in Fig. 3.1. The holes, drilled perpendicular to the head surface, are separated 90 degrees around the head axis and at 50 degrees from the tip. The pressure line internal diameter changes from 0.3 to 0.4 mm within the head. Thinner tubes allow reducing the head size (2.2 mm diameter) and the probe time response, but increase the risk of blockage due to air impurities. Two heads are combined on a rake at a distance of 18 mm, being 15 mm the distance between the stem axis and the probe tip (common to all the aerodynamic probes involved).

3.1.2 Probe-flow interaction effects

At the high flow velocities reproduced, and given the relatively small flow areas, flow modifications caused by the presence of the aerodynamic probes were a major concern. Numerical flow analysis were performed to analyze the global and local effects introduced by the probes. The study was based on an hypothetical rake of three five-hole probe heads for being the most adverse configuration in terms of area blockage, and the most sensitive probe to flow modifications. The numerical study considered the rake immersed in the region of minimum flow transversal area, Fig. 3.2-right, and under different flow conditions.

Flow simulations were performed in the complete test section domain using the same solver employed for the test section design, FINE/turbo

(Numeca International ©). Computations addressed two configurations: with and without the presence of the probe in the test section. The simplified rake geometry modeled is sketched in Fig.3.2-left. The hemispherical head was replaced by a cylinder, and a rectangular stem was considered instead of the real U shaped stem. The mesh was identical in both test-cases to avoid mesh dependency influencing the results, except within the area occupied by the probe which was mesh filled in the absence of probe. The grid used was composed by 33 million points. Boundary conditions were imposed in terms of inlet total pressure and temperature, and static pressure at the outlet. Three cases with different inlet total pressure boundary condition were imposed for each configuration, i.e., three different flow velocities.

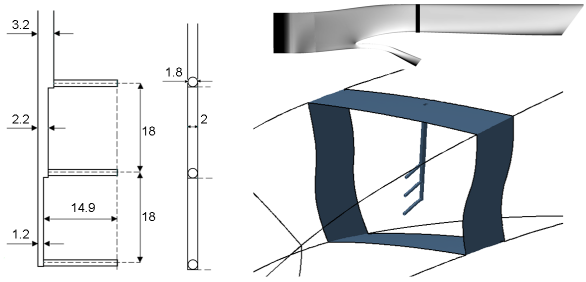

Figure 3.2: *Left: simplified file hole probe rake. Right: probe location in the test section.*

Several authors have treated the experimental evaluation of the blockage by means of static pressure measurements with different acceptance criterium [64–66]. Numerical flow results allow evaluating the global blockage effects due to the flow area reduction, but also the local flow behavior around the immersed object. Both effects are inherent to intrusive instrumentation and depend on the flow conditions. From the numerical characterization, the magnitude of those effects can be evaluated and correction factors can be derived if necessary to increase the fidelity in the measurements.

The probe modeled introducing a 1.2% area blockage at the position considered, reduces the mass flow through the test section by 1.1%. Local flow effects were evaluated by comparison of flow properties right upstream the location of the probe heads with respect to those at the same position in the absence of instrumentation. Figure 3.3 shows the deviation between the total pressure without and with the presence of the probe, relative to the total to static pressure difference without instrumentation. Results are presented for each probe head and local reference Mach number at each flow regime. Pressure values have been extracted in a plane right upstream the probe head through two approaches: considering the central point of the probe head, and computing pressure averaged values on the probe frontal area.

The second approach results in higher non dimensional pressure deviations. At M ~ 0.75, the frontal area averaged non dimensional pressure deviation is about 2 %. In terms of pressure it corresponds to a difference of about 10 mbar between the total pressure with and without instrumentation (2 mbar if only the central point facing the probe tip is considered). The non dimensional deviation between total pressure with and without instrumentation as represented in the plot, is reduced as the flow velocity increases, mainly due to the increase of dynamic pressure. No difference was found between each probe head location for the same flow condition. Thus the lower head probe was not affected by the wall proximity.

Given that the estimated maximum pressure differences computed were of the same order than the maximum total pressure error (section 3.1.6), and the expected lower blockage effects introduced by the two heads five-hole probe rake used on the experimental tests, no correction was considered to be required for the experimental measurements.

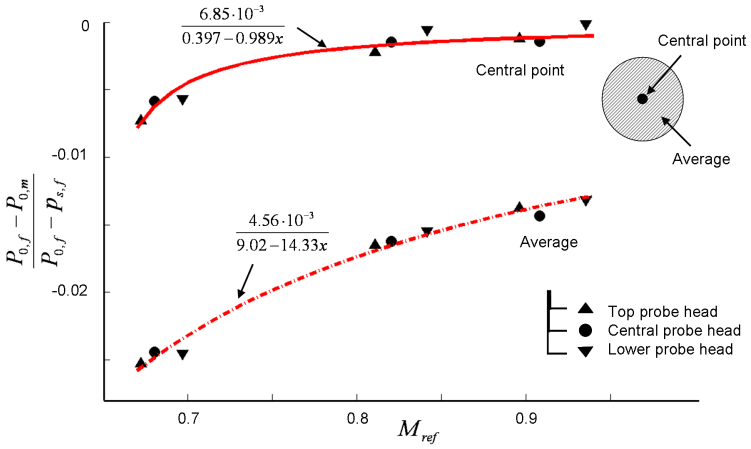

Figure 3.3: *Total pressure deviation caused by the presence of an aerodynamic probe.*

3.1.3 Five-hole probe flow data reduction methodology

A directional probe can be operated with two different strategies: null method and non-null method (or differential pressure method). In the first option an actuator rotates the probe at the measurement location until the pressure readings by two opposite pressure taps are equal, being the rotated angles the flow angles. In the non-null method the probe is held at a fix position during the acquisition and the angle is derived from the pressure readings. The first method requires less effort during the probe calibration and data reduction, but accurate and fast actuators are required to adjust

the probe orientation in a minimum time. The non-null method allows much faster data acquisition since it does not require to be reoriented, and therefore flow variations can be resolved up to the frequency response of the probe itself. However this method requires accurate probe calibrations , and data reduction algorithms to compute the flow variables from the pressure readings. Given the relatively large variability of the flow angles along the test section, and the importance of maximizing the number of measurement points at different positions during a test, the five-hole probe was operated in the non-null method.

The characteristics of the flow at a point in a steady three-dimensional flow are defined by four independent parameters: the two flow angles, the local Mach number and the local total pressure. Thus, in order to calculate the flow characteristics from the pressure readings, at least four pressures have to be measured, while their relationship to the flow parameters is established during a calibration by means of non dimensional coefficients. The probe calibration can be performed in a closed wind tunnel[67] or in a free jet[68], and requires to cover the range of flow directions and at flow regimes characteristic of the flow to be analyzed. During the calibration the flow is kept stationary at each of the angular positions and the pressure levels at each hole are recorded. Attempts have been performed to model the calibration map in order to simplify the calibrations reducing the number of points or overcoming the calibration limitations. Pisasale and Ahmed[69] used the potential flow theory to model the flow around the head. In case of supersonic flows, Milanovic and Kalkhoran[70] made used of a three-dimensional thin layer Navier-Stokes code to calibrate a five-hole probe. However those models are limited by the presence of manufacturing anomalies (tolerances, edge shapes, etc) which can only be accounted for by experimental calibrations. Independently of how the calibration is obtained, pressure readings from the different holes are reduced to a certain number of non-dimensional parameters that are commonly presented in calibration maps. The non-dimensional numbers obtained from the pressure readings during the measurements are then compared to the calibration maps by means of different approaches. Yasa and Paniagua [71] reviewed some of the different data reduction procedures encountered in the literature. Those approaches can be direct interpolation in the calibration maps , graphical methods[72], Taylor series decompositions[73] , polynomial curve fittings [74] or zonal decomposition of the calibration range [75] among others.

The traditional data reduction technique based on four non dimensional parameters presents certain limitations, particularly when the calibration maps are distorted, or when one of the non-dimensional parameters is erroneous due to a wrong lecture on one of the pressure readings. The same limitations appear in the majority of the proposed postprocessing techniques based on non dimensional parameters computed as pressure differences between the different readings. It can be avoided by handling directly the raw pressure levels without computing left-right pressure differences.

The technique employed in the present case was proposed by Yasa and Paniagua[71]. It is based on a calibration database of pressure readings instead of on calibration maps. The database contains the information of the probe pressure readings during the calibration process that are translated to six non dimensional coefficients using the definitions given in Eqs. 3.1,3.2,3.3. The coefficients cp_1 to cp_4 are function of the flow angles and the total and static pressure information are linked to cp_5 and cp_{ave}. The data processing algorithm (Fig.3.4) involves an iterative process covering all the points of the calibration database, that is performed for every set of five pressures provided by the probe. An initial guess for the static pressure is needed that can be considered from a near wall static pressure measurement. From that value and the known Mach number of the calibrations, the six non dimensional coefficients correspondent to a measurement point are computed. In a simplificative way, the method is based on the comparison of the non dimensional parameters from the probe measurements with the values registered in the database. The comparison is evaluated through a regression coefficient, which approaches unity when the probe readings agree with the calibration data set. A polynomial surface fit is then applied to the regression coefficients as a function of yaw and pitch anglesfrom which regression coefficients are defined for a posterior polynomial surface fitting. A distinct peak of the surface fitting reveals the flow angles. The sensitivity of the method can be referred as the steepness of the peak, or the valley if (1-r^2) is represented instead. For the determination of the flow angle, the surface fitting is only applied to the part of the domain revealing higher regression coefficients and using certain weighting factors. This results in a more pronounced peak and therefore, the accuracy of the method is increased. The total and static pressure coefficients are interpolated in the database based on the obtained pitch and yaw angles. The interpolated values are used to compute the actual total and static pressure of the measurement point. The resulting static pressure is then compared to the initial guess. If the static pressure difference is higher than a threshold, the calculation starts a new iteration from the the new static pressure.

$$cp_1 = \frac{p_1 - p_s}{p_5 - p_s} \qquad cp_2 = \frac{p_2 - p_s}{p_5 - p_s} \tag{3.1}$$

$$cp_3 = \frac{p_3 - p_s}{p_5 - p_s} \qquad cp_4 = \frac{p_4 - p_s}{p_5 - p_s} \tag{3.2}$$

$$cp_5 = \frac{p_5 - p_s}{p_0 - p_s} \qquad cp_{\text{ave}} = \frac{\text{mean}(p_{1-4}) - p_s}{p_0 - p_s} \tag{3.3}$$

3.1.4 Angle sensitivity analysis.

The new hemispherical five-hole probe performance was evaluated by comparison with an identical probe with lateral holes misalignment and with

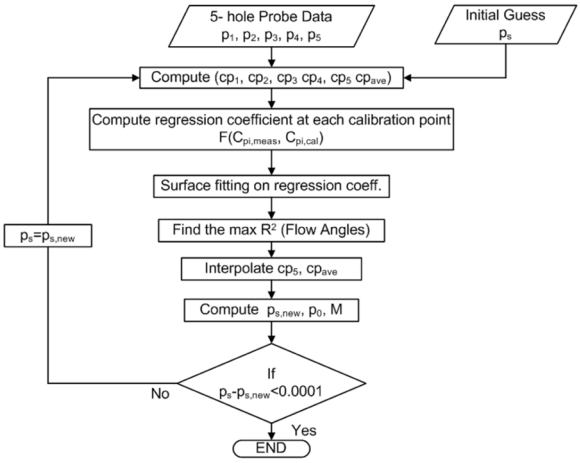

Figure 3.4: *Data processing algorithm.*

a conical probe. The analysis was based on the sensitivity of the individual non-dimensional parameters derived from different calibrations, and the sensitivity on the flow angle determination by means of the employed data reduction methodology. The geometrical characteristics of the conical probe are sketched in Fig.3.5. The cone angle is 60 degrees and the head diameter 3.2 mm. In the hemispherical probe with holes misalignment, the lateral holes are distributed each 90 degrees but slightly rotated from the vertical and horizontal references due to manufacturing irregularities.

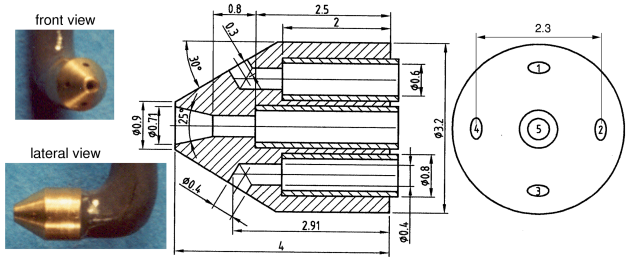

Figure 3.5: *Conical five-hole probe.*

The three five-hole probes were calibrated in a vertical nozzle free jet facility of 50 mm exit diameter. This blowdown wind tunnel is fed by a 40 bar pressurized reservoir (72 m^3). Different grids are mounted in the settling chamber to guarantee the uniformity of the flow and turbulence. Two computerized carriages allowed running an automatic angular calibration in pitch and yaw by pre-programming the engines rotating sequence, velocity and waiting times at each position. The error in angular position of each

step of the calibration was less than 0.1 degrees. Calibrations were performed for the range ±20 degrees and ±30 degrees of pitch and yaw angles respectively, at steps of 2 degrees, and for different Mach numbers between 0.4 and 0.9.

3.1.4.1 Sensitivity of selected non-dimensional coefficients to yaw angle variation

The pressure data obtained during the calibrations was reduced to different sets of the non-dimensional parameters defined by Eqs. 3.1,3.2,3.3. In the current data reduction methodology the flow angles are obtained from the four independent non-dimensional parameters corresponding to each of the lateral holes (cp_1 to cp_4). The sensitivity of those four coefficients to the yaw angle for different fixed pitch positions at different Mach numbers, and for the three five-hole probes under analysis, is compared in Fig.3.6.

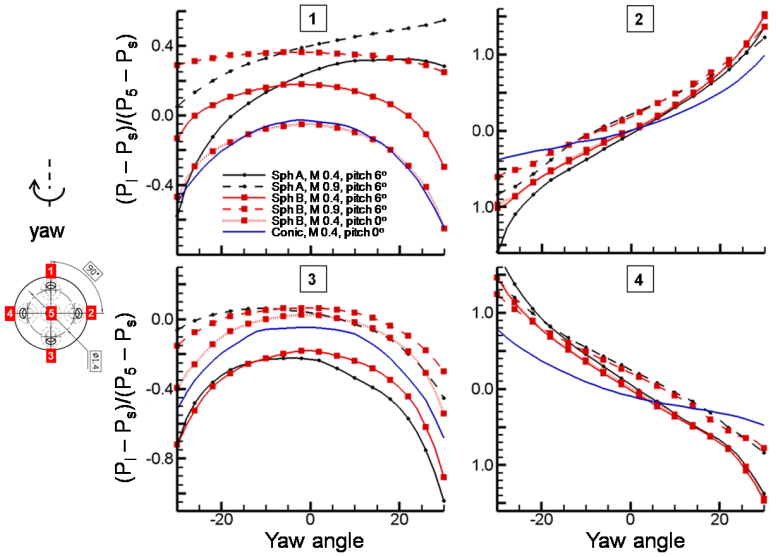

Figure 3.6: *Sensitivity of the non-dimensional pressure coefficients of the four lateral holes to yaw variation.*

Among the lateral holes non-dimensional coefficients, the sensitivity to the yaw angle is mainly provided by the coefficients cp_2 and cp_4. The coefficients correspondent to the upper and inner holes (cp_1 and cp_3), if properly aligned with the vertical and horizontal references, present a low sensitivity to the yaw variation for small absolute yaw angles which increases for increasing yaws. The two hemispherical heads denoted by A and B are compared at minimum (0.4 Mach) and maximum (0.9 Mach) flow speeds, for a fix pitch angle of 6 degrees, to analyze manufacturing irregularities and

Mach number dependence. The hemispherical probe with the lateral holes correctly positioned in the vertical and horizontal axis is denoted by B, and A corresponds to the probe with misalignment in the lateral holes. Since the analysis was done for yaw angle variation, the misalignment affects mainly the distributions of the upper and inner coefficients (cp_1 and cp_3), which do not reflect symmetric distributions with respect to 0 yaw angle. The sensitivity of the left and right pressure coefficients due to the holes misalignment is only slightly affected, since the the variation of cp_2 and cp_4 due to the yaw modification is predominant. The opposite would be observed from the comparison of probes A and B for a fix yaw angle varying the pitch angle. From the comparison of probe B at the maximum and minimum flow speeds, the angular sensitivity is slightly reduced when the flow speed is increased (lower slope of cp_2 and cp_4 with yaw angle). The sensitivity remains unaffected if a different pitch angle is considered for the analysis, the only effect being an offset in the non-dimensional value of cp_1 and cp_3. Comparison of probe B and the conical probe at 0 pitch angle and 0.4 Mach number shows a large yaw angle sensitivity reduction for the conical probe.

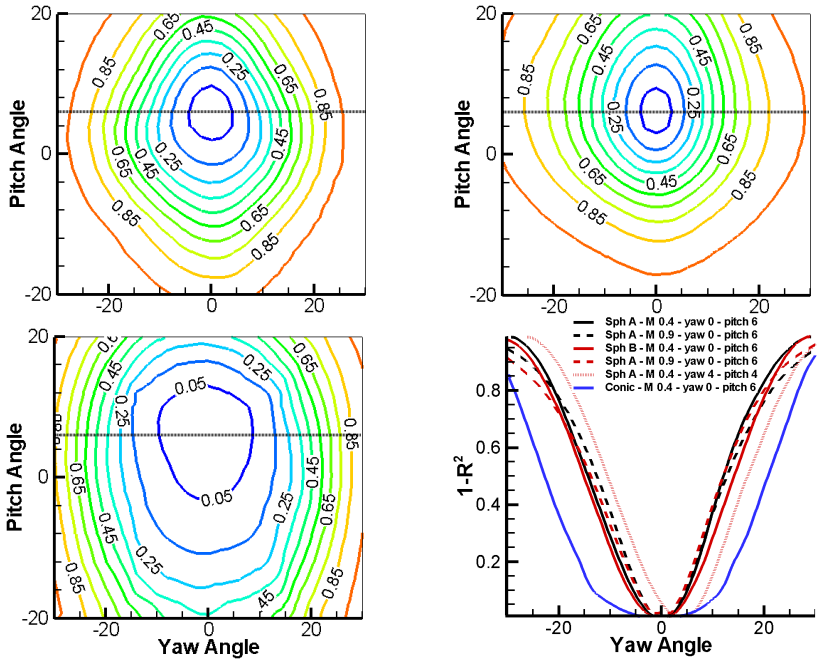

Figure 3.7: *Contours of (1-r^2) for pitch=6 deg., yaw=0 deg., determined with: a)hemispherical head B M=0.4, b)hemispherical head B M=0.9, c)Conical head M=0.4. d)1D (1-r^2) distributions for different probes, flow velocities and angles.*

3.1.4.2 Sensitivity to angles determination through the data reduction method

To analyze the sensitivity of the flow angle determination for the three different five-hole probes, measurements on the calibration jet facility at different flow velocities and known probe angular positions were performed. The probes were set at a certain known pitch and yaw angle at the outlet of the free jet and two Mach numbers were tested, M=0.4 and M=0.9. The non-dimensional coefficients computed from the pressure measurements where compared with the database obtained from the calibrations, and the data reduction methodology applied to determine the flow angle correspondent to the input non-dimensional coefficients. Additionally, the correspondent data points were removed from the calibration database. The sensitivity of the method can be referred as the sharpness of the peak of the polynomial fitting of regression coefficients, or valley of $(1\text{-}r^2)$. Distributions of $(1\text{-}r^2)$ are represented in Fig.3.7 for different flow angles, velocities and probes. In the top of the figure isolines of $(1\text{-}r^2)$ over the complete calibration range are represented for the design hemispherical head tested in the jet with an incident flow at 6 and 0 degrees in pitch and yaw respectively, for the two Mach number tested, 0.4 in the left figure and 0.9 in the right. The left bottom shows isolines of $(1\text{-}r^2)$ obtained for the conical probe at same incidence angle and flow Mach number of 0.4. The 1D plot in the bottom right of the figure shows the distributions of $(1\text{-}r^2)$ along a constant pitch angle line as the indicated in the contours for different cases. Either from the top isolines contours and from the 1D plot, the slight increase in sensitivity as the flow velocity increases for a given probe is observed in agreement with the sensitivity of the individual non-dimensional coefficients observed in Fig. 3.6. The valley of the regression coefficients around the angular position is slightly more sharp for the hemispherical head with holes misaligned (probe A) than for the design probe (probe B), indicating a small increase in sensitivity of the flow angles determination. For the same flow velocity and flow angles the conical probe shows a much wider valley, which in agreement with the evaluation of the individual non-dimensional coefficients, shows its inferior capability for an accurate determination of the flow angle. The accuracy of the determination of the flow angle is not dependent on the particular flow angle within the range of pitch and yaw tested for this analysis. The sensitivity is the same if the flow was at 4 degrees of pitch and yaw, than when immersed at pitch 6 degrees and yaw 0 degrees

3.1.4.3 Error estimations based on the postprocessing methodology

The error on the flow angle determination associated with the postprocessing methodology can be analyzed using the data from the calibrations. In the case in which the Mach number is known, the database including only the calibration at that Mach number is used. For this purpose all the calibration points were treated one by one. For the evaluation of a certain point (pitch

and yaw angle values), the correspondent values of pressure were considered as a test measurement. The information related to this point was removed from the calibration database. The methodology for the determination of the flow angles was then evaluated with the pressures correspondent to that particular point as an input. The result is shown in Fig. 3.8 in which the contour plots represent the difference between the computed yaw and pitch angles and the exact ones. This procedure overestimates the error since the most important information from the database, on the region where the solution is located, is being removed. This would have a similar effect than performing less detailed calibrations. The plot in Fig. 3.8 corresponds to the calibration of the hemispherical head designed for the current investigation at M=0.9. The dots show the real angular positions. The exact flow angle is computed with a maximum error limited to 0.2 degrees for incidence values within the interval $-20 < yaw < 20$ approximately. For higher yaw angles the error in the yaw determination increases up to 0.3-0.4 degrees. It can be justified by two reasons: by the flow/probe incidence, or by the data reduction procedure. The linear behavior of the sensitivity of the lateral holes coefficients to yaw variations was seen to be altered for yaw values higher than ± 20 degrees (Fig.3.6). In the current data processing methodology, the surface fitting is performed taking into consideration the points with higher regression coefficients from the database. In the limits of the calibration map, the information from the surrounding points is not balanced, since it does not exist information for higher angles.

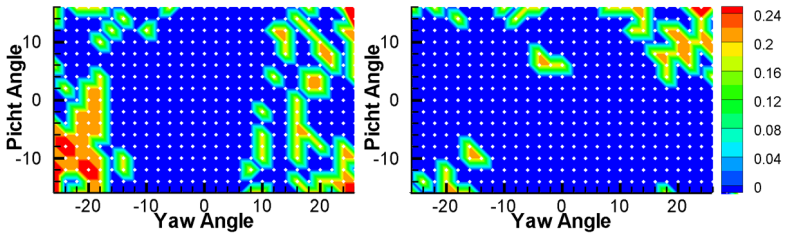

Figure 3.8: *Error evaluation for yaw and pitch angles (in degrees).*

The influence of flow speed on the flow angle is analyzed in Fig. 3.9. The data collected during a calibration at Mach 0.9 was treated as measurement data, and the flow angle was derived using the calibration data at Mach 0.4. The error is evaluated as the difference between computed and real incidence angles. When the yaw angle is lower than 16 degrees the maximum error in pitch and yaw angle is limited to 0.6 and 0.9 degrees, respectively. This error is to be considered if the probe calibration is only performed at one flow velocity.

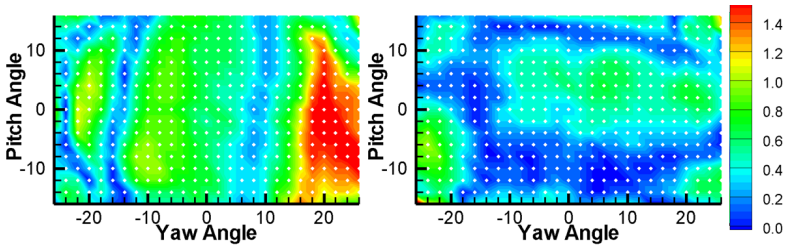

Figure 3.9: *Influence of the velocity on the error on the angle determination.*

3.1.5 Five-hole probe operation in the transonic facility

The geometrical complexity of the current test section imposed certain constrains to the instrumentation positioning, which affected particularly the five-hole probe measurements. Map measurements performed at different planes along the test section required optimizing at each map axial location the direction of insertion of the instrumentation (stem axis) in order to maximize the accessible measurement area. Fixed the direction of insertion, the probe head, perpendicular to the stem, was oriented at each measurement plane to be aligned with the mean flow direction in terms of yaw angle. Thus, at each measurement plane two different angles defined the orientation of the instrumentation.

Since the stem axis was not parallel to the local radial direction as commonly set in annular test-rigs, the probe head was not aligned with the flow. This had important implications in the flow/probe angular range in which the probe was operated. Calibrations were performed in the vertical nozzle free jet facility described in section 3.1.4, within the range ±26 degrees for yaw angle and 0-44 degrees for pitch angle. The probe positioning had also implications on the data processing, since the angles measured in the probe reference system required to be transformed to a coordinate system with flow significance.

The yaw and pitch angles, as derived from the pressure readings through the five-hole probe data reduction methodology, were converted to the local cylindrical coordinate system at each point, thus related to the radial, circumferential and axial flow velocities. The angular transformation was performed in two stages.

First, angles measured with respect to the probe axes were translated to a global test section coordinate system. Secondly the global angles were projected on the local coordinate system at each point. The angular transformations are sketched in Fig.3.10. The global axes are defined by the test section axial direction (same as the engine), and the horizontal and vertical references with respect to the ground. The angles defining the probe orientation at each measurement plane are: φ, rotation around the axial di-

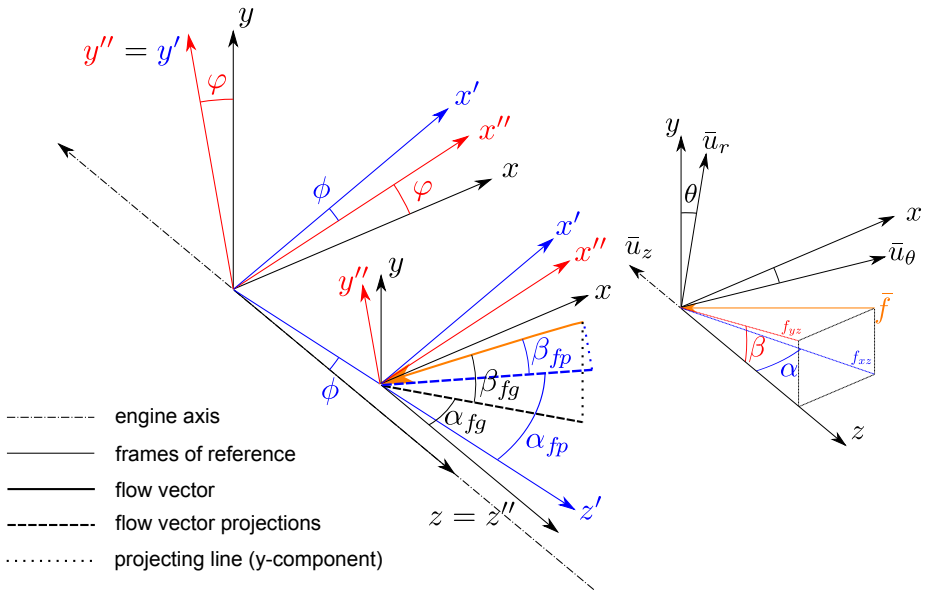

(a) 1^{st} *transformation: probe to global axes.*

(b) 2^{nd} *transformation: global to local axes.*

Figure 3.10: *Angular transformations.*

rection, and ϕ, a second rotation around the direction of immersion. Pitch and yaw flow angles with respect to the probe axes are denoted by β_{fp} and α_{fp} respectively, and by β_{fg} and α_{fg} with respect to the global axes. The convention β-α for the projection corresponds to that of the calibration procedure. The relation between the angles in both coordinate systems is given by Eqs. 3.4-3.5.

The angles expressed in the global test section coordinate system were then referred to the local cylindrical system. This is defined at each point by the local radial and tangential directions, and linked with the global coordinates by the angle θ. Pitch and yaw angles in the local coordinate system denoted as β and α respectively are not dependent on the order of projection but defined as the angles formed by the tangential and axial velocity components (α), and the correspondent to the radial and axial velocity components (β). The trigonometric relations defining the flow angles are expressed in Eqs. 3.6-3.7.

$$\alpha_{fg} = atan\left[\frac{cos\beta_{fp} \cdot cos\varphi \cdot sin(\alpha_{fp} + \phi) - sin\beta_{fp} \cdot sin\varphi}{cos\beta_{fp} \cdot cos(\alpha_{fp} + \phi)}\right] \tag{3.4}$$

$$\beta_{fg} = asin(cos\beta_{fp} \cdot sin\varphi \cdot sin(\alpha_{fp} + \phi) + sin\beta_{fp} \cdot cos\varphi) \tag{3.5}$$

$$\alpha = atan\left[\frac{cos\beta_{fg} \cdot sin\alpha_{fg} \cdot cos\theta - sin\beta_{fg} \cdot sin\theta}{cos\beta_{fg} \cdot cos\alpha_{fg}}\right] \tag{3.6}$$

$$\beta = atan[\frac{cos\beta_{fg} \cdot sin\alpha_{fg} \cdot sin\theta + sin\beta_{fg} \cdot cos\theta}{cos\beta_{fg} \cdot cos\alpha_{fg}}] \tag{3.7}$$

The chosen local reference system is such that pitch values are positive when the radial flow velocity component is negative, while positive yaw angles are linked to tangential velocity components in the direction imposed by the inlet guide vanes.

3.1.6 Uncertainty of the five-hole probe measurements.

The accuracy of the flow magnitudes derived from the pressure readings of the five-hole probe is limited by the combined effect of errors arising from the pressure sensors and probe calibrations, the probe installation, and the data reduction procedure, as well as from the flow and test-rig environment.

Pressure measurements, both from probe calibrations and tests, are subjected to the same random and systematic sources of error since the same measurement chain and flow environment was involved. The bias error on the pressure measurements was restricted through strict experimental practices: control of zero balances on relative pressure transducers and detailed sensors calibration. Calibration errors for the two pressure transducers employed (Validyne variable reluctance transducers and ASM piezoresistive transducers) were 0.025% (20:1) for a mean pressure value of 200 mbar. Signals sampled at 1KHz during 1 sec., the largest error contribution was due to the standard deviation of the voltage signal, 0.4% (20:1). Accounting for all contributions and considering the whole pressure range involved, global (bias and random) pressure uncertainties were lower than 1 mbar.

The cumulative error on each derived flow magnitude can be estimated as the Root of Sum of Squares (RSS method) of the different contributions to the error. For each of the flow magnitudes three main error contributions were considered: error caused by a pressure perturbation in the measurements, error caused by a pressure perturbation during the calibration, and error associated to the data reduction procedure.

A direct source of error implicity included in the estimation of the global error is the bias error associated to the probe positioning. It affects in the same magnitude to the probe installation in the calibration set-up as in the test-rig. The associated uncertainty on yaw and pitch angles was determined by the resolution of the electronic level, 0.1 degrees. This contribution is of the same order as the correspondent to the pressure perturbations, and can be considered as the source of a pressure perturbation in the readings, either during the calibration or during the measurements.

The contributions based on pressure perturbations were computed applying error propagation theories with a perturbation equal to the pressure uncertainty, 1mbar. The different contributions were evaluated based on flow measurements performed in a transversal plane in the region of the test section where the heat exchangers were located. Thus, a full set of five pressures for different locations was considered, and also a calibration database

with information for one flow Mach number exclusively.

For estimating the first contribution, a pressure perturbation was introduced in one of the five probe readings for all the set of data, the data reduction procedure evaluated with the new pressures, and the output compared to that of the original set. This procedure was repeated for each of the five-hole probe readings. The contribution to the error for each derived flow variable corresponded to the biggest deviation within the set of data, independently of the pressure reading perturbed or the point at which the deviation was maximum.

For computing the error due to a pressure perturbation during the calibration, the same set of flow data was considered, but perturbations were introduced in each of the pressure readings involved in the calibration, five of the five-hole probe and total and static pressures. For each perturbation at a sensor reading on the whole calibration data, the new calibration map was used to compute the derived flow parameters from the test flow data, and from them, the deviations with respect to the no perturbed case. For each derived flow variable the maximum deviation independently of the perturbed reading and test data point, was considered as the contribution to the error.

The error associated to the data reduction methodology was computed using only the calibration database for the a certain calibration Mach number. All the calibration points were treated one by one. For the evaluation of a certain point the pressure information correspondent to that point in the database was removed, and it was considered as the input data from a test. The data reduction methodology was then evaluated and the output compared to the real flow magnitudes associated to that point. This procedure repeated for all the points of the calibration, provided maps of deviations for each of the flow variables. Only the region of the map corresponding to the pitch and yaw ranges involved in the reference measurement plane used for the error evaluation was accounted. Within this region, the maximum deviation was considered as the contribution to the error for each variable.

The maximum individual contributions for each of the flow variables, as well as the global maximum error are indicated in Table.3.1. The largest contribution corresponded to the data reduction procedure. However, the method applied provides overestimated deviations, since no data information is missing from the calibration during the postprocessing of the real test measurements. Therefore, the presented uncertainty analysis is an estimation of the maximum errors involved.

3.2 Shielded fine-wire thermocouple probes

In aeroengine component testing [76–78] high fidelity in the total temperature measurements is needed. Thermocouple probes for high accuracy gas temperature measurements require specific designs optimized for the ap-

	p_i' *meas.*	p_i' *cal.*	*method*	*Global Error*
yaw, [deg.]	0.1	0.1	0.85	0.86
pitch, [deg.]	0.1	0.1	0.9	0.91
P_t, [mbar]	1.6	1.4	10	10.2
P_s, [mbar]	0.55	1.1	2.3	2.6
M	0.0013	0.0013	0.003	0.0035

Table 3.1: *Maximum individual error contributions and cumulative error of the five-hole probe flow measurements*

plication of interest, and precise characterization of their uncertainty and response characteristics. In the present investigation numerical simulations were performed to study the steady and unsteady heat balances within a temperature probe and to evaluate both the temperature field during a transient and at equilibrium conditions.

Multiple attempts to provide correction factors for standard thermocouple designs were found in the literature [79–83]. The experimental evaluation of the time response has been a continuous subject of interest in which both internal and external heating techniques have been applied. Internal heating consists on heating electrically either with a continuous or pulsating DC current [84] or with AC current [85]. The time constant was deduced from the thermocouple temperature decay after the removal of the DC/AC overheating current. However the internal heating offers several disadvantages [86] such as Peltier effects and non-uniform temperature distributions over the sensor. In turn, the external heating includes a wide array of possibilities: oscillating temperature jet created by a the wake of a heated wire [87]; laser beam [86]; cold air jets impulses [88]; rotating wheel chopping hot and cold tubes [89]; fast displacement of probes to regions of different temperature [90]; fast displacement of probes to a rocket plume [91]. In addition to dynamic characterizations, overall recovery factors were traditionally experimentally determined as an indicator of the temperature error of a thermocouple. Such global recovery factors accounted for the total effect of radiation, conduction and convection on the probe for a given flow environment. The variability of the heat fluxes balance within the probe with the environment and probe design, required each thermocouple to be carefully designed and calibrated for the required application. However, exact corrections from experimental calibrations were impractical. Furthermore, not only the testing flow conditions but also the thermal interactions between the probe and the test bench required to be duplicated in the calibration set-up. The precision to reproduce and to characterize the calibration environment determined the accuracy of the corrections.

Zeisberger [92] applied one dimensional heat transfer calculations to analyze the influence of the steady temperature errors for different geometrical

parameters of a kiel thermocouple. The current conjugate numerical characterization of shielded thermocouple probes performed the coupled fluid convection and solid conduction. The developed numerical methodology allowed understanding and quantifying the influence of the design parameters, essential to achieve a good design for precise gas temperature measurements, and characterizing the steady and transient response of the thermocouple probe optimized for the present application.

3.2.1 Thermocouple probe design

Total flow temperature measurements were to be performed in transient conditions in the new 3D transonic wind tunnel [77]. Design objectives common to the rest of the instrumentation, as probe miniaturization and short response times to maximize the number of measurement points during a test, applied also to the temperature probe. Given the relatively small spatial temperature variations and the variation of the inlet temperature during a test, the following aspects were particularly important: high-frequency response, error minimization, and precise characterization of the probe response. The compliance of those objectives was necessary to synchronize all readings with the mean flow temperature variations, as well as to accurately analyze the flow temperature effects produced by the heat exchangers. Thin wire thermocouples were more suitable to fit the requirements of this application, than other kind of total temperature probes [93].

The temperature of a thermocouple junction is the result of the energy balance including the convective heat flux between the junction and the surrounding gas, radiation to the walls, and conductive flux to the wire. The measured temperature would be equal to the total flow gas temperature in the absence of radiative heat fluxes, conductive flux to the thermocouple support and dissipation of kinetic energy in the boundary layer.

General design rules reported in the literature, [94, 95], as well as design recommendations for particular applications based on comparative analysis of different probe configurations [79, 80, 96, 97], provide the basis to reduce the temperature error sources on new designs. A shield is recommended in order to decrease the error caused by the transformation of kinetic energy into thermal energy in the boundary layer around the junction (often called velocity error). The shield also provides structural resistance in high velocity flows and reduces radiation effects [98]. However, decreasing the velocity of the flow decreases the convective heat transfer, increasing the conduction error and the response time. Thus, the internal velocity must be kept as high as allowable. The internal velocity is function of the vent hole to inlet ratio. The junction position within the shield is a compromise between entrance flow effects, radiation shielding and convective heat transfer between the thermocouple and the shield. Recommended values are given by Rom and Kronzon [80] and Glawe et al. [79]. The wires within the shield can be

placed parallel or perpendicular to the flow. In the first case, the length of the wires is limited to prevent wire bending. In the second, the length is limited by the shield diameter.

Conduction errors can be estimated from the one dimensional energy balance on a wire element. Integration along the wire considering symmetry boundary condition at the junction ($y = 0$), and isothermal temperature $T_w = T_{sp}$ at the support of the wire ($y = l$), results on a simplified solution for the wire temperature distribution [99]. At the position of the junction, the temperature is the given by Eq. 3.8. The assumptions of constant gas temperature T_0, and constant convection coefficient h required for the simplified integration along the wire, neglect the effect of the real flow temperature differences along it.

$$T_0 - T_j = \frac{T_0 - T_{sp}}{\cosh(l\sqrt{\frac{4h}{k_w d_w}})} = \frac{T_0 - T_{sp}}{\cosh(l/l_c)} \tag{3.8}$$

Design rules derived from this simplified solution recommend to have high values of convective heat transfer coefficient (high velocities), high length to wire diameter ratios l/d_w, low conductivity wire materials k_w, and support temperatures T_{sp} close to gas temperatures. Petit et al. [87] suggest that the ratio l/l_c should not be smaller than 5.

The contribution of the error due to radiation is generally important at high flow temperatures. In the present transonic flow application both the flow and the test section walls remained at $\pm$ 15 $^\circ C$ of the ambient temperature. Considering the most adverse case of unity view factor and equal conductive and radiative areas, radiative error estimations yielded a negligible error contribution, lower than $4 \cdot 10^{-4}\%$, about 1 mK.

In the case of uniform temperature on the junction, constant heat transfer coefficient independent of time, and no heat transfer by conduction between the junction and the adjacent wire, the thermocouple response to a temperature step is a first order system, Eq. 3.9, where τ is the characteristic time constant. The assumption of first order system would also be valid for the assembly wire and junction if their diameters are identical, there are no radial or longitudinal temperature gradients, no conductive heat transfer to the supports, and the heat transfer coefficient is constant in time and along the length of the wire.

$$T_0 = T_j + \tau \frac{\partial T_j}{\partial t}, \quad with \quad \tau_j = \frac{\rho_j C_{p_j} V_j}{h_j S_j}; \quad \tau_w = \frac{\rho_w C_{p_w} d_w^2}{4 k_g N u_w} \tag{3.9}$$

A thermocouple probe was designed in the basis of the pre-existing design rules to fit the particular requirements of this work. The temperature probe consisted of a rake of five shielded thermocouples. The geometric characteristics of the temperature probe heads are sketched in Fig. 3.11. A type

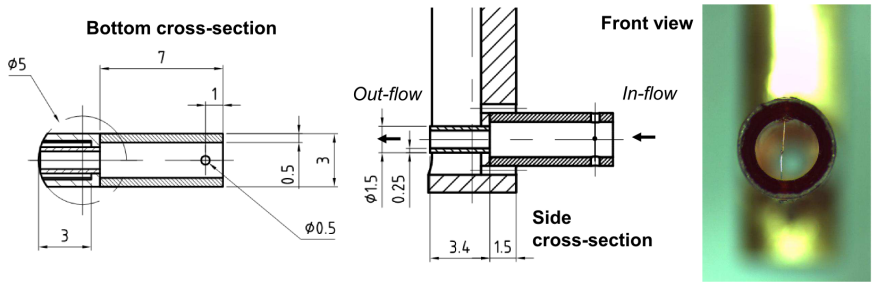

Figure 3.11: *Shielded thermocouple probe.*

T thermocouple (copper-constantan) was placed perpendicular to the flow with a total length equal to the internal shield diameter, 2 mm. This wire configuration was intended to avoid wire bending at high velocities. Ratios l/d_w of 39 were obtained with wires of 25.4 μm diameter. The ratio bead to wire diameter from the OMEGA unsheathed fine gage thermocouples was 2.7. The shield diameter was a compromise between blockage minimization, wire structural resistance and limitation of conductive errors. The shield was made of polycarbonate, chosen for its low conductivity. In agreement with the values recommended in the literature [79], [80], the inlet/outlet area ratio was 4 and the junction was mounted at 1/2 internal shield diameters from the entrance.

3.2.2 Methodology of the aerothermal study

Experimentally, the accuracy of the temperature corrections required a precise control of the gas temperature excitation and test conditions. Instead, in the current research the transfer function of the thermocouple probe was numerically obtained by evaluating the response to a temperature step.

Both the flow field around the shielded thermocouple and the thermal interaction between flow and thermocouple were numerically resolved by means of conjugate heat transfer simulations. At the transonic conditions of interest, the characteristic time for the flow to develop around the thermocouple is two orders of magnitude smaller than the characteristic time of the thermal transient in the thermocouple wires. This allowed solving the aerothermal interaction flow-thermocouple by performing simulations in two steps, which highly reduced the computational cost. First, a steady simulation was solved to establish the flow around the probe considered isothermal. The flow-field solution of this step was imposed as initial condition for the simulation of the following stage. In the second step, the solid boundary conditions were changed and a conjugate heat transfer (CHT) simulation was performed, solving the energy balances within the thermocouple. This second stage was evaluated in steady or transient state depending on whether

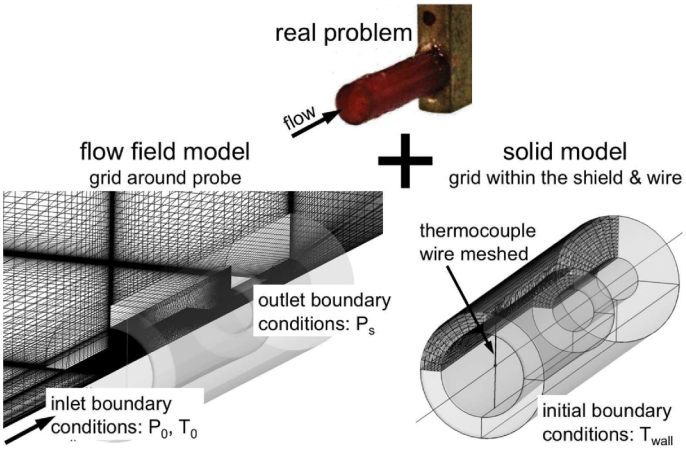

Figure 3.12: *Schematic of the computational grid and boundary conditions. Top: Image of the shielded thermocouple. Left: Gas mesh around the shield. Right: Mesh in the solid domain.*

the interest was focused on the steady temperature errors or on the transient behavior. In the latter case, the result was the response of the thermocouple to a temperature step.

This methodology allowed the detailed analysis of the heat fluxes within the thermocouple probe, and the evaluation of the influence of the flow environment, probe geometry and wire materials.

3.2.3 Numerical tools

The shielded thermocouple head was modeled in a 3D domain constituted by a quarter of a cylinder thanks to the existence of two symmetry planes on the probe geometry, Fig. 3.12. The domain comprised 6 shield diameters in the radial direction and in the axial direction upstream of the probe, and 10 diameters downstream. The three solid parts (shield, wire and junction) were meshed independently and concatenated to the gas domain mesh in the solver. The hybrid 3D mesh is composed by about 1.75 million cells. The grid was refined along the walls of the solid parts and specially around the thermocouple wire and junction.

The Reynolds Averaged Navier Stokes solver employed was CFD++ (v.8.1) [100], and the k-epsilon turbulence model was used. The initial values of k and epsilon were estimated in function of the free stream nominal velocity, with a free-stream turbulence level of 1% and a turbulence length scale based on the tube inner diameter. Values of y^+ in the vicinity of the thermocouple junction are lower than 0.3, and lower than 0.5 along the wire. For the steady simulations on both stages, convergence was achieved after 1000

	Geom 1	*Geom 2*	*Geom 3*
$l, [mm]$	1	1	1
$d_w, [mm]$	0.0254	0.0508	0
$d_j, [mm]$	0.07	0.14	0.07

Table 3.2: *Probe geometric configurations.*

iterations , 5.5 hours CPU time in 8 parallel Intel Core 2 Quad Q9400 (2.66 GHz) machines. For the transient CHT simulations the number of iterations required to achieve convergence varied depending on the wire material. In average 1000 iterations with different time steps were required, involving 51 hours of CPU time running in 8 parallel machines. The integration time step was adjusted as function of the rate of evolution of the junction temperature, starting from 0.1 ms.

Nominal flow conditions for the simulations correspond to inlet boundary conditions T_s = 273 K, P_s = 101325 Pa, V_∞ = 231 m s^{-1}, and P_s = 101325 Pa at the domain outlet. Different Mach and Reynolds numbers were tested for the geometrical configuration corresponding to the design geometry.

Three geometrical configurations were analyzed: *Geom 1, 2 and 3* (Table 3.2). The geometrical parameter varied was the wire diameter. *Geom 1* corresponds to the design case. The wire diameter is doubled in *Geom 2* where the ratio junction to wire diameter has been kept constant. *Geom 3* refers to the test case of a junction with infinitely thin wires. The shield diameter was not chosen as parameter since bigger values would increase the undesired blockage effects and lower values would decrease the wire length and thus, increase the conduction errors.

Heat loss through the wires to the support is function of the wire dimensions and flow conditions (convective heat flux), but also of the wire material conductivity, and support material and temperature. To study conduction effects, four wire materials (Table 3.3) and three types of boundary conditions at the support were considered for the configurations *Geom 1* and *Geom 2*. The selected wire materials are copper, constantan, nicrosil (lowest conductivity among those used in thermocouples), and an ideal material with conductivity equal to 1 $Wm^{-1}K^{-1}$. The different shield-support boundary conditions tested were:

1. Adiabatic shield,
2. Isothermal shield at 300 K,
3. CHT in the shield.

In all cases the shield material was polycarbonate (Table 3.3), and the junction properties the average of the two materials of type T thermocouples.

	Copper	Constantan	Nicrosil	Ideal	Polycarbonate
K, [W m^{-1} K^{-1}]	401	19.5	13	1	0.2
ρ, [kg m^{-3}]	8930	8860	8530	8860	1210
C_p, [J kg^{-1} K^{-1}]	385	390	460	390	1250

Table 3.3: *Material properties of thermocouple wires and probe shield. Evaluated at 23° C.*

3.2.4 Steady temperature effects

3.2.4.1 Global temperature correction

The junction temperature results from the balance between the convective heat fluxes gas-junction and gas-wire, and conductive flux junction-wire and wire-support. If those effects were decoupled, individual error equations could be used to estimate the deviation of the measured temperature from the different error contributions. However, in practical applications the junction temperature must be evaluated by the simultaneous solution of the different heat flux rates [84].

The overall temperature error (1-Z), associated to the overall recovery factor Z, is defined as the difference between the total gas temperature and the measured temperature $(T_0\text{-}T_j)$, relative to the dynamic temperature $(T_0\text{-}T_\infty)$. The overall recovery factor can be decomposed into several contributions as indicated in Eq. 3.10. The first term (a) is the velocity error, related to the adiabatic recovery factor. The second term (b), takes into account the temperature error due to conduction and convection along the wire, for a given support-shield temperature, (T_{sp}). The last term (c) collects the velocity error of the support-shield and the conduction effects between the shield, probe stem, and external probe support. The applied numerical method allowed analyzing separately each contribution.

$$(1-Z) = \frac{T_0 - T_j}{T_0 - T_\infty} = \overbrace{\frac{T_0 - T_{ad}}{T_0 - T_\infty}}^{a} + \overbrace{\frac{T_{ad} - T_j}{T_{ad} - T_{sp}}}^{b} \cdot \overbrace{\frac{T_{ad} - T_{sp}}{T_0 - T_\infty}}^{c} \tag{3.10}$$

The experimental evaluation of the different contributions to the overall recovery factor was not feasible since velocity and conduction effects could not be measured independently. Fig 3.13 compiles global recovery factors for different thermocouple probes, obtained experimentally by Paniagua et al. [83] for different Mach numbers. Tests were conducted for various shielded and bare thermocouples with wires parallel and perpendicular to the flow.

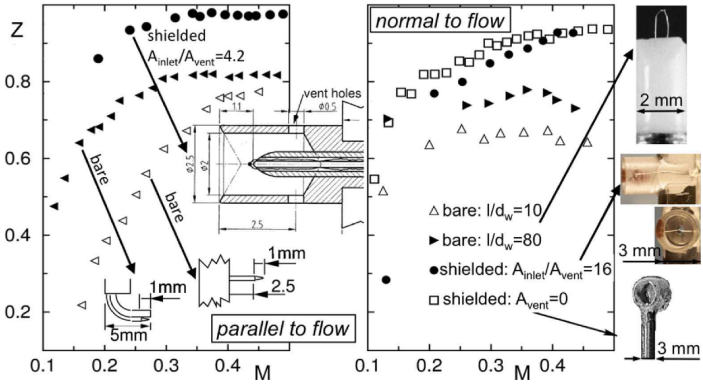

Figure 3.13: *Experimental Overall recovery factors as a function of Mach number for bare and shielded thermocouples*

3.2.4.2 Velocity error

Temperature probes are intended to measure the gas total temperature, i.e. the temperature that the gas would attain if it is brought to rest through an isentropic process. However, in real gases frictional heat is generated within the boundary layer, hence the conversion of kinetic energy into thermal enthalpy is not perfect. The recovery factor, Eq. 3.11, represents the amount of kinetic energy recovered by the gas, where T_{ad} is the temperature of the surface of the junction if it would behave as an adiabatic body, and V is the reference upstream flow velocity. The recovery factor is function of the geometry of the immersed body, the Prandtl number of the fluid and the flow velocity. Experimental values of adiabatic recovery factor determined by different authors [96],[101],[102] were presented by Moffat [95].

$$r_a = \frac{T_{ad} - T_s}{V^2/2C_p} = 1 - \frac{T_0 - T_{ad}}{V^2/2C_p} \tag{3.11}$$

In case of adiabatic shielded thermocouples the reference flow velocity in the recovery factor ($r_a(V)$) is the velocity upstream of the junction within the shield, referred as V_{int}. Therefore, the term (a) in Eq. 3.10 represents an overall adiabatic recovery factor. Note that in the case of bare thermocouples r_a=Z_a.

$$Z_a = \frac{T_{ad} - T_{s,\infty}}{V_\infty^2/2C_p} = 1 - \frac{T_0 - T_{ad}}{V_\infty^2/2C_p} = 1 - (1 - r_a)\frac{V_{int}^2}{V_\infty^2} \tag{3.12}$$

The experimental determination of adiabatic recovery factors was impractical since the junction temperature has to be determined with great accuracy, and ensuring negligible influence of conduction to the supports, so the junction behaves as an adiabatic body. Steady simulations at different flow velocities allowed determining both r_a and Z_a and their sensitivity to flow

Mach and Reynolds numbers. Wire and shield were considered adiabatic solids in the computations and CHT was solved at the junction, at T_{ad}.

Computations were also performed considering all the solid boundaries adiabatic, including the junction. The average temperature on the junction adiabatic surface $T_{ad,m}$ was compared with the junction temperature obtained when CHT was applied. Temperature differences were observed to be lower than 0.004 % $((T_{ad,m} - T_{ad})/T_{ad,m})$.

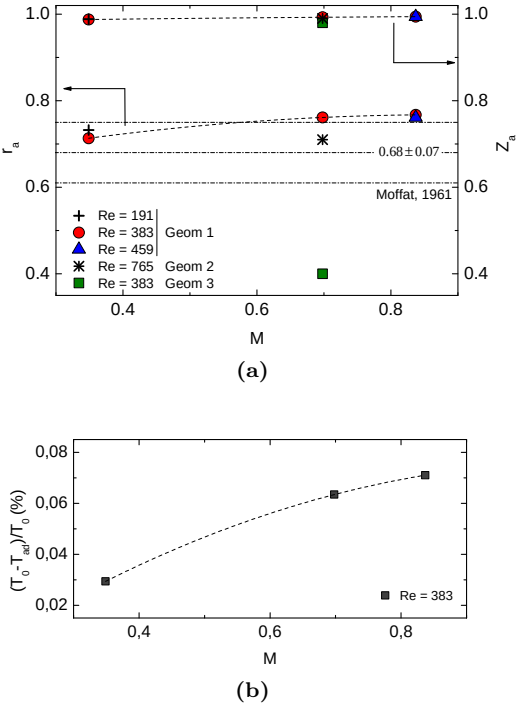

Figure 3.14: *(a) Recovery factors for different probe geometries, Mach and Reynolds numbers. (b) Temperature error due to not isentropic flow deceleration*

Figure 3.14a shows the evolution of the recovery factor (r_a) and the overall recovery factor (Z_a), for different Reynolds and Mach numbers. The results are in good agreement with recovery values compiled by previous researchers [95] and obtained under controlled experiments in order to avoid the influence of other error sources different from the velocity error.

Red dot symbols represent recovery factors computed for a given probe geometry (*Geom 1*, nominal design) and at constant Reynolds number based on the wire diameter of 383, for different flow Mach numbers. The adiabatic recovery factor (r_a) increases slightly with the Mach number, and thus with the velocity within the shield (V_{int} is about 1/6 of V_∞). The overall recovery

factor *(Z_a)* shows the same trend although due to the presence of the term V_∞, the effect of the variations of the adiabatic junction temperature on the recovery factor is attenuated. For the same probe geometry (*Geom 1*) at constant Mach number, a decrease in the Reynolds number to 191 achieved through a decrease in static pressure, results in a slight increase of the recovery factor (cross symbol). This effect is noticeable in the adiabatic recovery factor *(r_a)* and less in the correspondent overall recovery factor *(Z_a)*. In the same way an increase of Reynolds number results in a decrease of the recovery factor (blue triangle symbol).

The variation of the wire diameter at nominal flow conditions is directly translated to a change of the Reynolds number. Results obtained for *Geom 2* with double wire diameter and a flow Reynolds number of 765, provide an adiabatic recovery factor (star symbol) lower than the correspondent for the thinner wire.

Recovery factors were computed likewise for the infinitely thin wire case *(Geom 3)*, providing lower values (green square symbol). The flow behavior around a sphere is not similar to that around a thermocouple junction, neither to the flow parallel to a cylinder [95]. Comparison of the flow fields around the junction for both geometries, showed a stronger flow deceleration forced by the presence of the wire, and hence, a thicker thermal boundary layer. Consequently the transformation of the flow kinetic energy into thermal energy is more efficient.

Results prove the increase of the recovery factors with increasing Mach number and with decreasing Reynolds number. Nevertheless, the temperature error represented in Fig. 3.14b by the ratio $(T_0 - T_{ad})/T_0$ still increases with increasing Mach numbers since the kinetic energy rises at higher rate than the recovery factor.

3.2.4.3 Conduction error

Free of velocity errors, the difference between the real junction temperature and the total temperature is the error due to conduction, namely the product of terms (b) and (c) in Eq.3.10. In a well designed thermocouple the junction temperature should be little sensitive to the support temperature, i.e. the term (b) is close to zero. In that case the overall contribution of conduction would be negligible whatever is the value of term (c).

Term (b) reflects the influence on the junction of the balance conduction-convection along the wire and the conduction with the support. In a first approximation, its contribution can be estimated by the solution of the one dimensional energy equation, Eq.3.8, that predicts an exponential decrease with the increase of the parameter l/l_c (for $y \geq 5$, $\cosh y \simeq 0.5exp^y$). Term (c) indicates the strength of the conduction heat transfer between the thermocouple and the support. The lower temperature of the shield-support with respect to the total gas temperature (T_{ad} in the absence of velocity error),

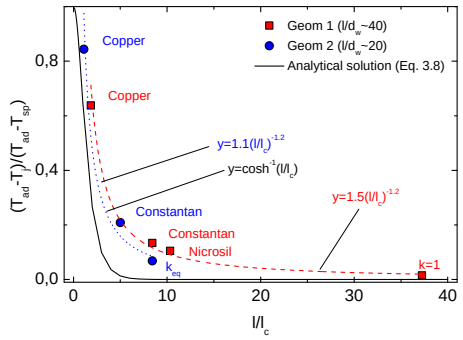

Figure 3.15: *Non-dimensional conduction temperature error in function of the parameter l/l_c. Results from CHT simulations*

$T_{ad} - T_{sp}$, drives the conduction to the wire. In the case the support would be perfectly isolated from external sources, it is function of the recovery factor of the complete shield/support. In real applications it is also function of the depth of immersion of the support in the flow, the support geometry and thermal properties, and the external boundary conditions of the probe.

The values of the parameter l/l_c for each material and for each of the geometries *Geom*1 and *Geom*2 are indicated in Tab. 3.4. In Eq. 3.13, for the computation of l/l_c, air conductivity was evaluated at the gas total temperature [84], and the Nusselt number was derived from a correlation for wires perpendicular to the flow [95]: $Nu = (0.44 \pm 0.06)Re^{0.5}$.

$$\frac{l}{l_c} = l\sqrt{\frac{4h}{k_w d_w}} = \frac{2l}{d_w}\sqrt{\frac{Nuk_g}{k_w}} \tag{3.13}$$

	Constantan	Copper	Nicrosil	Ideal	Equivalent
k, [W m^{-1} K^{-1}]	19.5	401	13	1	6.89
l/l_c (Geom 1)	8.43	1.86	10.33	37.24	
l/l_c (Geom 2)	5.01	1.11	n.a.	n.a.	8.43

Table 3.4: *Conductivities and l/l_c ratios for the different wire materials and probe geometries evaluated.*

Figure 3.15 shows the non-dimensional conduction temperature error corresponding to term(b) in Eq.3.10. All results correspond to complete CHT simulations. The temperature difference ratio is plotted versus the parameter l/l_c, which for a given probe geometry is only function of the wire material. The error decreases as the parameter l/l_c increases indicating that the junction temperature is less influenced by the conduction effects. It has

been also included in Fig. 3.15 the non dimensional conduction error computed for the thicker wire geometry ($Geom2$) and an hypothetical material denominated *"equivalent"*. Its conductivity was chosen such that the associated l/l_c value computed for $Geom2$ is identical to the l/l_c computed for constantan and the thin wire geometry ($Geom1$) *(*$k_{eq} = k_{const}\sqrt{2}/4$*)*. For those two materials two different values of the non dimensional conduction error were obtained for the same value of l/l_c, showing the limitations of the analytical expression conventionally used to estimate the conduction errors (Eq. 3.8). Indeed the present results show two slightly distinct trends for each l/d_w, that are best fitted by power laws with a common exponent coefficient of -1.2 instead of by the predicted hyperbolic cosine trend. The error underestimation introduced by the analytical expression can be explained by the simplifications introduced for its derivation, mainly the assumptions of homogeneous gas temperature and constant heat transfer coefficient along the wire. It can be concluded that the parameter l/l_c is a good estimator of the conduction error, but inappropriate to establish a unique relation with the temperature error.

Figure 3.16a represents the global contribution to the conduction error computed for the reference probe geometry ($Geom1$) for different materials. The figure compares for a given wire material and geometry, thus a given l/l_c, the variability of the temperature error due to the conditions at the shield/support. Fig. 3.16b displays the temperature distribution along the wire in the same conditions for three of the materials and two of the boundary conditions, isothermal support and CHT within wire and support. The junction temperature ($y = 0$) is the same for the ideal wire ($l/l_c = 37$) independently of the conduction at the shield, with an overall conduction error of about 0.04 %. The temperature at each position along the wire is less affected by the longitudinal conduction, hence by the shield temperature, and more by the convective heat flux. Thus the temperature distribution is able to reflect the non homogeneity of the gas temperature around the wire. The junction is only influenced by the wire temperature adjacent to it, and the effect of the shield temperature penetrates only through the last 20% of the wire. In the case of constantan wire, the temperature is affected by conduction to the shield to a higher extent. However, the temperature at the junction converges to almost the same value for the different boundary conditions. Overall conduction errors vary between 0.18 and 0.19 %. In the copper wire case, with a l/l_c about 2, conduction with the support influences the junction temperature in a higher degree. Errors vary between 0.23 and 0.45% depending on the support conditions.

The reference adiabatic temperature considered for the analysis of the conduction errors is that of the junction. However, due to the strong flow deceleration taking place around the wire in the vicinity of the junction, there is a less efficient flow deceleration in this region. Thus, the temperature recovered is lower when compared to the junction. This effect can be observed in Fig. 3.16b for the ideal wire distribution in which the tempera-

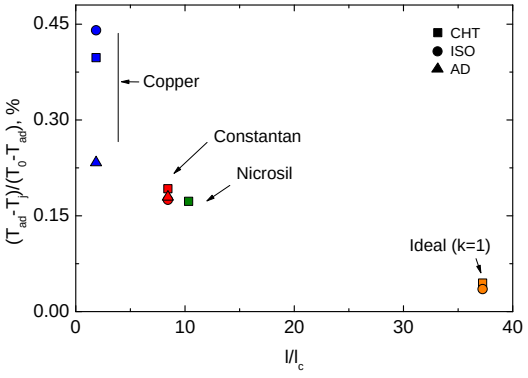

(a)

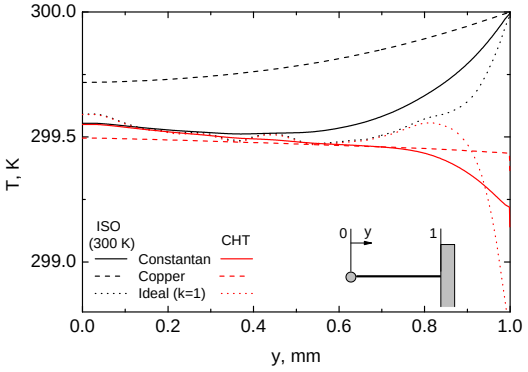

(b)

Figure 3.16: *(a) Overall temperature errors due to conduction in function of l/l_c. (b) Wire temperature distributions*

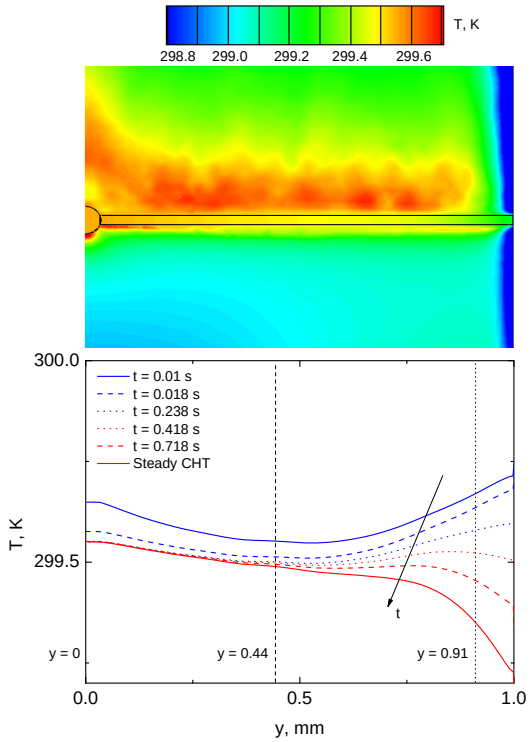

Figure 3.17: *CHT numerical results. Top: 2D temperature contour, steady conditions. Bottom: Evolution of constantan wire temperature distribution.*

tures at 10 to 20 % from the junction are slightly lower than at the junction. It explains also the slight difference between the junction temperatures for constantan and ideal material wires. The higher conductivity of constantan forces the junction to stabilize at the lower temperature of the wire in the vicinity, while for the ideal material the temperature at the junction rises to almost the adiabatic temperature.

3.2.5 Transient temperature effects

The diffusion of the heat fluxes within the probe introduce a temperature lag on the junction temperature with respect to the gas temperature. The properties and geometry of the thermocouple wires affect the junction temperature evolution. The numerical methodology applied in this study allowed analyzing the temperature evolution on the complete probe in response to a temperature step. All the results correspond to the nominal flow conditions, with an initial probe temperature equal to $T_i = 300$ K.

The temporal evolution of the temperature along the constantan wire for

*Geom*1 is displayed in Fig.3.17. The response time of the shield is much higher than that of the junction or wire due to its larger thermal inertia and lower thermal diffusivity. Thus the part of the wire closer to the junction y = 0 reached the final temperature faster than the part of the wire close to the shield/support due to its influence by conduction. Figure 3.18 shows the time temperature history at three wire positions and a point within the shield, for constantan and copper materials. Temperature traces were made non dimensional using the steady level (T_f).

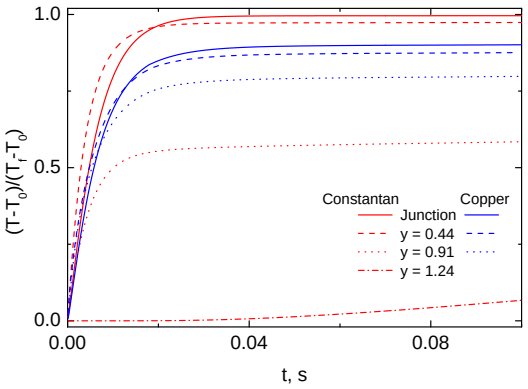

Figure 3.18: *Temperature evolution at four control points on constantan and copper wires.*

All the temperature distributions, except that of the shield, showed a fast initial temperature change, followed by a slower evolution. The fast initial temperature rise is dictated by the inertia of the junction or wire elements. The slow down is accentuated by the influence of the support at a certain position. In the constantan case the junction overpassed the conventional threshold of the 63.2 % of the response in 6.5 ms, and achieved the 90% of the final temperature in 18 ms. The temperature at y = 0.44 mm showed a faster initial rise due to the lower thermal inertia of a wire element when compared with the junction, of bigger volume. However the convergence to the final temperature takes longer than in the junction due to the influence of the evolution of the shield at this point. The same behavior was observed at y = 0.91 mm, although further influenced by the shield temperature evolution.

The comparison of the temperature evolutions in the copper wire case is analogous. The initial response of the copper is slightly slower than with constantan, and the temperature evolutions at the different points nearer to each other. It is explained by the higher conductivity of the copper, that implies higher diffusivity along the wire, and thus smoother temperature gradients between the different positions. Whereas in the constantan case, the effect of the support is almost negligible close to the junction.

Neglecting junction-wire conduction, the response of the thermocouple

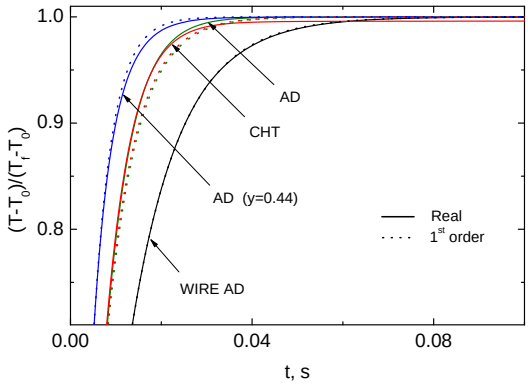

Figure 3.19: *Comparison of junction temporal evolutions with the correspondent first order.*

would be that of a first order system, Eq. 3.9. The system would be defined by the time required to complete 63.2% of its response to a gas temperature step. None of the wire temperature evolutions represented in Fig.3.18 corresponds to a first order response due to the influence of the support.

Non dimensional junction temperature evolutions are represented in Fig. 3.19 for the ideal case of adiabatic wire, and constantan wire with two different support conditions: CHT and adiabatic. For each evolution the time to reach 63.2% of the final temperature was used to evaluate the correspondent first order response. When the wires are considered adiabatic, the junction evolution collapses to the first order response. The presence of the wires modifies the temperature response independent of the condition at the support. When no flux occurs between shield and wires the junction reaches the final temperature without the delay caused by the support but it does not correspond to a first order. This result is in agreement with the works of Yule et al. [103] and Petit et al. [87]. The influence of the wires causes an acceleration of the junction response when compared with the adiabatic wire result. It is instigated by conductive effects from the faster response of a wire element. The evolution at y = 0.44 mm is included in the graph for comparison.

Figure 3.20 displays the non dimensional junction temperature evolutions for different wire materials and the two wire diameters ($Geom1$ and $Geom2$). All cases correspond to complete CHT simulations with the consequent possible influence of the slower response of the support. For the cases in which the conductive effects on the junction are not too noticeable ($l/l_c \geq 5$), the higher the wire conductivity the faster the response of a wire element and therefore the faster the response of the junction. Increasing the wire and junction diameters introduces a delay in the response due to the increase of the thermal inertia, and a decrease of the parameter l/l_c, hence an increase

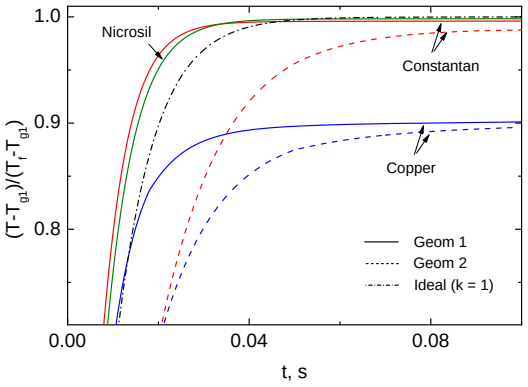

Figure 3.20: *CHT numerical results. Junction temporal evolution.*

of the conductive fluxes.

The characteristic flow Reynolds number affects the rate of temperature change through its influence on the convective heat transfer. In order to analyze the Reynolds dependance, junction temperature evolutions were resolved for the nominal flow conditions, i.e Reynolds number of 383 for *Geom 1*, but also for two other lower values (*Re* 100 and *Re* 158). For temperature responses following a first order behavior the characteristic response time would be inversely proportional to the Nusselt number. In general, it is possible to evaluate the Reynolds number effect on the initial part of the temperature response, where conduction effects are not predominant. Characteristic times were evaluated considering the ratio between the response and its derivative during the first milliseconds.

Experimental evaluation of the transient response of the shielded thermocouple corresponding to *Geom 1*, was evaluated in a small free jet calibration stand sketched in Fig. 3.21. The set-up consisted of a plenum chamber and a smooth contour nozzle, which vented to atmosphere. Air from a pressure line was heated up through an electrical mesh upstream the plenum chamber. The nozzle exit diameter was 12 mm. The shielded thermocouple was located very close to the exit of the nozzle, to minimize any heat loss. A shutter was placed between the nozzle and the probe to subject the thermocouple to a flow step. Inside the settling chamber a thermocouple and a Pitot probe measured total conditions. The total temperature was kept constant at 70 °C. Note that in this set-up, the Reynolds number is almost proportional to the Mach number. In the range of total pressures tested, the Reynolds number based on the wire diameter varied between 75 and 154. Higher Reynolds numbers could not be achieved due to limitations on the maximum total pressure.

Figure 3.21-left shows the initial junction temperature evolutions for two of the different flow conditions tested, and the correspondent of the CHT

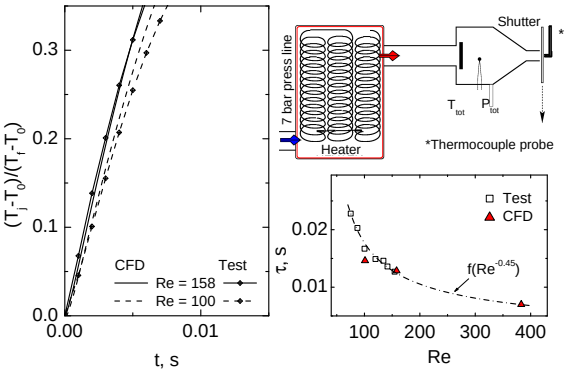

Figure 3.21: *Experimental and numerical comparison of the Reynolds number effect on the shielded thermocouple response time*

simulations for the same Re numbers. The increase of the flow velocity, and thus of the Reynolds number, due to an increase of total pressure at ambient pressure and constant total temperature, increases the convective heat transfer coefficient, accelerating the response. Characteristic times evaluated for the experimental responses decreased with increasing Reynolds numbers as represented in Fig 3.21-right. The trend representing the experimental results was found to be of the type $(a + b * Re^{0.45})^{-1}$. This result is in agreement with the Nusselt correlation proposed by Collis and Williams [104]. The trend obtained at the lower experimental Reynolds numbers fits the numerical value obtained for a Reynolds number about three times higher.

Assuming the response of a thermocouple can be expressed as linear system model of m-order, the transfer function of the thermocouple in the complex frequency domain (z) can be expressed by the ratio of two m-order polynomials, Eq. 3.14. A digital procedure [105] was used to determine the invariant transfer function that reproduces the junction response in each case.

$$H(z) = \frac{b_0 \cdot z^{-d} + b_1 \cdot z^{-1-d} + \ldots + b_m \cdot z^{-m-d}}{1 + a_1 \cdot z^{-1} + a_2 \cdot z^{-2} + \ldots + a_m \cdot z^{-m}} \tag{3.14}$$

A first order response was found for $Geom1$ with adiabatic wires and for $Geom3$, in accordance with the temporal analyses. A second order system fitted the junction response when the support is adiabatic. Likewise, a second order system represented the complete CHT simulation in the case of the ideal wire material, where the conductive effects are negligible. For the case of the nicrosil wire, a third order response was found. The higher the effect of the support, the higher the order of the system was found to represent the transfer function. For both $Geom1$ and $Geom2$ with constantan wires, the response was modeled with a 5^{th} order system. For copper wires

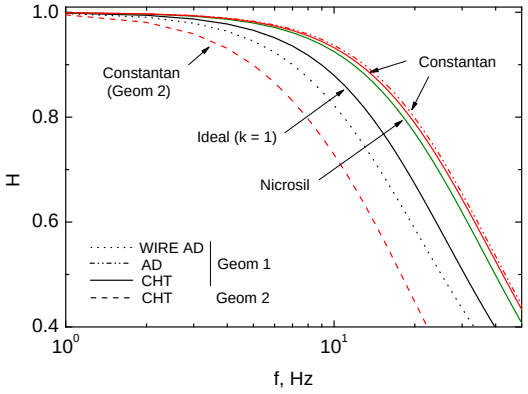

Figure 3.22: *Transfer functions for different wire materials, wire diameters, and support conditions.*

the response could be considered 5^{th} or 6^{th} order. The transfer functions representing the junction responses for several test cases are shown in Fig. 3.22. The faster response corresponded to constantan wires with cutting frequencies slightly higher than 10 Hz.

3.2.6 Uncertainty on temperature measurements

The accuracy of the temperature measurements by means a thermocouple probe depends on the probe design and on the flow and test environment which determine the errors due to conduction, radiation and velocity effects, but it also depends on the errors of the signal acquisition, and in the accuracy of the calibration of the measured signal. Accurate experimental calibrations are costly and difficult since they require a strict control of the flow conditions used as reference for the calibration, and the probe to be exposed to the same sources of error than during the tests, thus to the same test environment. The constrains for the experimental calibration could be reduced in the case it could be ensured that the thermocouple is not affected by conduction or radiation errors during the tests. In this case the calibration environment should also ensure that it is not influencing the measurements by those mechanisms.

The numerical methodology presented in this investigation facilitates the probe characterization. It can be used, as previously proposed, to ensure that a given design is free of conduction errors in order to simplify the experimental calibrations. However, for any design, its output can be directly used to estimate the contribution of the different sources of error associated to the flow and probe characteristics. The error contribution due to the signal calibration can be then obtained in a steady experimental environment, at zero flow velocity, with the solely constrains of not introducing

	$\Delta T/T$ [%]	ΔT [K]
Conduction	0.038	0.11
Velocity	0.063	0.18
SteadyCal.	0.035	0.10

Table 3.5: *Maximum individual error contributions to the bias temperature error*

spurious radiation errors or conduction errors in the case the probe design is sensible to the stem conditions (known from the numerical characterization). This procedure allows characterizing individually the different error contributions from which the cumulative bias error can be estimated as sum of the individual errors.

The results of the numerical procedure applied to the probe design used in the experiments, provided the errors due to conduction and those caused by velocity effects. Conduction errors were evaluated for different heat flux conditions at the support. The largest conduction error for the shielded thermocouple probe accounted to 0.038%. For the test flow conditions, maximum temperature errors due to velocity effects were about 0.063%. Radiation errors were estimated to be lower than 0.004% in the present application.

The uncertainty associated to the calibration of the temperature signal is defined by the procedure followed to perform the static calibration. The shielded probe was calibrated in a calibration oven. Temperature uniformity was warranted by means of a cylindrical capsule open in both extremes, in which the absence of temperature stratification was verified. Reference bare thermocouples previously calibrated in a precise oil bath were placed facing the junction of the shielded thermocouple and at different positions within the jail. A large probe immersion depth was set in order to avoid conduction effects due to the stem. The measurement chain used during the calibration was the same as during the tests. An electronic ice-point reference unit was used to minimize the cold reference junction error, with an stability of ± 0.03 °C. The associated bias temperature error was 0.1 °C (20:1).

The different contributions to the bias temperature uncertainty are summarized in Table 3.5, based on a mean flow temperature of 288 K. The largest contribution is due to the adiabatic recovery factor. The thermocouple measurements were corrected with the adiabatic recovery factors derived from the probe characterization, reducing the maximum systematic errors to 0.2K. In the case the velocity effects were not corrected, the maximum temperature error would be 0.4K. Random temperature errors were estimated lower than 0.1K when accounting for the contributions of the signal acquisition and the standard deviation on the oven calibrations. The global temperature uncertainty on the temperature measurements (bias and ran-

dom) is estimated on 0.3K.

The maximum rate of inlet temperature variation during the tests was 0.02 K/s. The transient numerical and experimental probe characterizations provided information on the response time of the temperature measurements. Given the fast response of the thermocouple temperature in comparison with the rate of flow temperature change, corrections on the thermocouple temporal response by means of the thermocouple transfer function were nor applied. However, the information on the response time was used to optimize the automatic probe moving system in such a way that the thermocouple reaches the steady temperature equilibrium at each fix measurement point, before being displaced to the next position. This allowed maximizing the number of measurement points during a test while ensuring the absence of transient errors on the measurements due to the probe response or inlet temperature variation.

3.3 Probe selection

The design of the different probes for flow characterization, demanded to meet different kind of requirements derived from the geometrical test section constrains, flow characteristics, and operation of the wind tunnel, in addition to the requests on the measurements. Map measurements at different positions along the test section were aimed, such that a complete measurement contour was obtained for a given probe within a single test run, with sufficient resolution, and covering the largest area possible within the plane (of about 0.01 m^2). The geometry of the two-dimensional contours of the measurement planes (distorted trapezoids) were different for each the axial position. Information on the measurement range of the flow variables to be measured was estimated from the numerical simulations performed during the test section optimization. Maximum testing times were estimated from the one dimensional wind tunnel models that assisted the design. With those constrains and objectives the design of the instrumentation was driven by the main criteria: probe miniaturization, robustness, high spacial resolution, short response time, wide flow angle range operability, and accuracy.

To maximize both area coverage and resolution, the number of measurement points within a test was increased by the use of rakes and relatively fast probes (short response times). Instrumentation miniaturization (head and stem) was essential to reduce blockage effects, specially critical in the present case combining transonic flows and limited flow area. Size reduction was limited by minimum functional probe head considerations, and probe robustness (stem diameter). All probes were designed to introduce similar frontal blockage. Probe head miniaturization was also aimed for increasing spatial resolution. The distance between the probe head tip and the stem axis was imposed to ensure the absence of flow modifications due to the presence of the stem. It was conserved for all probes. The minimum distance

between heads was fixed to avoid flow influence between consecutive heads. The maximum number of heads was fixed by geometrical considerations of the measurement planes (maximum and minimum immersion lengths within the different planes), and rake robustness (thinner support in the region of the heads, and increased diameter far from the heads). However the number of heads on a rake was also limited in the case of the five-hole probe by the stem diameter, which must fit the pressure lines of all the probe heads.

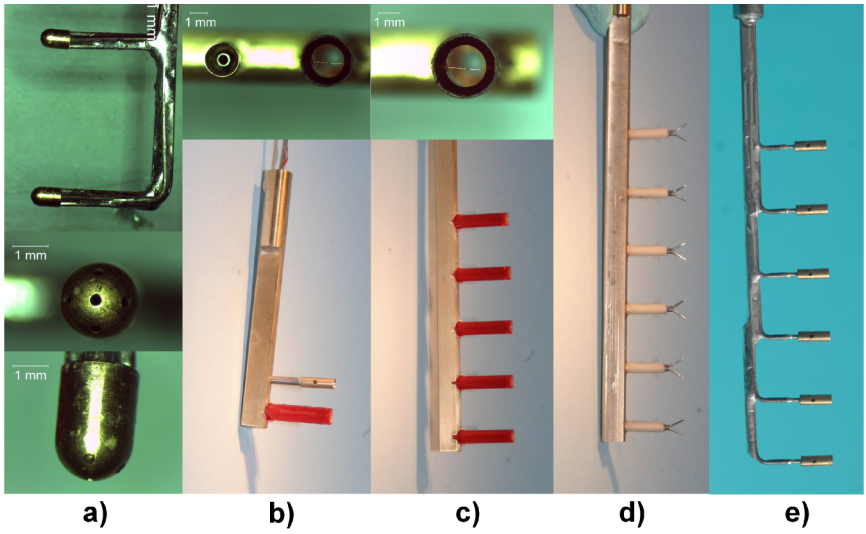

Figure 3.23: *a) hemispherical five-hole probe rake, b) reference probe, c) shielded thermocouple rake, d) hot-wire rake, e) shielded Pitot probe rake.*

The different intrusive probes designed are pictured in Fig. 3.23. Rakes of five-hole probes, shrouded Pitot probes, shielded T-thermocouples, and hot-wires, as well as reference probes combining shrouded Pitot and thermocouple probe heads were used. The maximum frontal width of the rakes was 2-3 mm in the region where the heads are located. A stem of 6 mm diameter was used in all the probes far from the probe heads to increase stiffness. The distance between the stem axis and the heads tip was 15 mm. The distance between heads was 12 mm in all probes except for the five-hole probe, were heads were separated 18 mm to ensure no influence on the pressure measurements by consecutive heads.

Six shrouded Pitot of 2 mm external diameter were mounted in the total pressure probe rake. Four vent holes are included in the shield providing a ratio A_{in}/A_{out} of 1. The use of a shield reduces the sensitivity to flow angles increasing the angular operational range. The insensitivity of the total pressure to pitch and yaw angles was demonstrated for flow angles up to 34 degrees at Mach 0.06. Two hemispherical heads of 2.2 mm diameter compose the five-hole probe rake due to space limitations within the

stem to include more pressure lines without compromising the risk of pipe blocking. Hemispherical heads were selected for their better performances at transonic speeds and wider angular span. Five shielded thin wire T-thermocouples were included in the temperature probe rake. The external diameter of the polycarbonate shield was fixed to 3 mm as a compromise to maximize l/d_w (reducing conductive error) while keeping the wire structural resistance. The use of the shield increases the angular insensitivity, the sensor recovery factor, and serves as support for the thermocouple wires placed perpendicular to the flow direction. Turbulence intensity measurements were performed by a rake of six platinum coated tungsten hot-wires, of wire length and diameter 5 mm and 9 μm respectively. The design of the probe heads on the reference probe corresponded to that of the Pitot and thermocouple probes.

3.4 Conclusions

Detailed analysis have been presented regarding five-hole probe and thermocouple probe designs. The main conclusions are summarized in the following:

3.4.1 Five-hole probes

Among the existent measurement techniques to measure flow direction, and when high-frequency measurements are not demanded, multi-hole probes are the best alternative for their comparatively reduced cost, simplicity, and accuracy provided.

For flow direction measurements in a transonic environment, and when a wide angular range is required, hemispherical probes have shown a superior performance with respect to conical five-hole probes regarding sensitivity to angle variations. Previous works already suggested the advantages of hemispherical heads for the transonic range, although a clear agreement was not found in the literature. Comparison of sensitivity of non-dimensional coefficients computed from the five pressure readings to angle variations for both type of probes was performed during this work based on calibration data for a 60 and 40 deg. span on yaw and pitch angle respectively. The influence of manufacturing irregularities in the five-hole probe due to holes misalignment was also addressed.

The influence of blockage effects was studied through numerical computations, providing overestimated total pressure errors induced by the presence of the probe lower than 2%.

The methodology used for the calculation of the five flow variables derived from the pressure readings on a five-hole probe, plays an important role on the accuracy of the results. Multiple studies have addressed this topic in the literature. The methodology employed in this investigation overcomes the limitations of the traditional data reduction procedure based on four non di-

mensional parameters, i.e., not able to deal with distorted calibration maps due to manufacturing imperfections, failure when one of the five readings is erroneous. This data reduction method is based on a database of calibrations instead of on individual calibration maps. The procedure was adapted for this application and its capabilities and sensitivity to angles and Mach variations analyzed. The evaluation of error caused by the data-reduction procedure estimated with calibration data yielded errors lower than 0.4 degrees on the two derived angles, within the angular range evaluated: ± 20 degrees and ± 30 degrees for pitch and yaw respectively. Maximum angle errors in the case the five-hole calibration is only performed for one flow velocity, Mach 0.4, and measurements are performed at Mach 0.9 were lower than 0.7 degrees within the previous range of pitch and yaw angles.

The flow variables derived from five-hole probe measurements are subjected to several errors from the calibration of the pressure transducers (affecting probe calibration and tests), to errors during probe calibration, errors on the probe installation and errors derived from the flow and test-rig environment. An estimation of the maximum errors affecting the derived flow magnitudes, evaluated based on flow measurement performed in the most sensitive region of the test section, yielded maximum errors lower than 0.9 degrees for pitch and yaw, 10 mbar (about 2%) for total pressures, 2.6 mbar (about 1.3%) for static pressures, and about 0.45% in the case of Mach numbers.

3.4.2 Fine shielded thermocouples

Accurate temperature measurements require specific designs and precise uncertainty characterizations. However, thermocouple probes are subjected to error sources difficult to experimentally evaluate due to the difficulty to determine the error in a certain environment, and also due to the difficulty to reproduce the real test environment on a calibration. A numerical procedure was proposed that outperforms previous experimental approaches to analyze the thermocouple response and provides an insight on the mechanisms of the different sources of error. The current conjugate numerical characterization applied to shielded thermocouple probes performs the coupled fluid convection and solid conduction, and allows studying the steady and unsteady heat balances within the probe.

General design rules reported in the literature based on simplified energy equations, and design recommendations based on comparative analysis of different probe configurations, provide the basis to new designs. When accuracy on the temperature measurements is required, those simplificative analysis are no sufficient to ensure the validity of the design. The new methodology was applied to the fine wire shielded thermocouple designed within this investigation, as well as to similar designs with different values of wire diameter and material. Also different boundary conditions at the wires support were analyzed. Results provided information on the probe

characteristics, and allowed the understanding of the heat transfer processes within the probe and the influence of the design parameters on the different sources of error.

The commonly described experimental "recovery factor" can be dissected in two steady error sources: flow velocity effects and conductive errors, that can be analyzed separately with the proposed method. Radiation effects were shown to be negligible in the flow environment addressed.

Adiabatic recovery factors, representative of the velocity error, were computed for different Mach and Reynolds numbers and showed a good agreement with experimental results for bare thermocouples obtained by previous researches under strict experimental control. Adiabatic recovery factors increase with increasing Mach numbers and decreasing Reynolds numbers, and are improved by the use of shields. Besides the increase on recovery factor, the temperature error increases for increasing Mach numbers due to the higher rate of increase of the kinetic energy.

The influence of conductive errors on the junction temperature is mainly dictated by the parameter l/l_c, which collects the effects of the wire conductivity, length and diameter, and of the flow convective heat transfer. Also the geometry and material of the support plays an important role which influence of the temperature error depends likewise on the parameter l/l_c. It has been proved that conductive temperature errors decrease with increasing l/l_c, and that for values of l/l_c lower than 5, the junction temperature error is dominated by the support characteristics.

The temporal temperature evolution within the probe was analyzed through time resolved conjugate heat transfer simulations. Its sensitivity to varying wires conductivity and diameter, as well as the influence of different conditions at the interface wire/support, was evaluated. When no heat transfer exist between the wire and the support, the temporal response is driven by the thermal inertia of the thermocouple. It has been observed that the presence of the wires accelerates the response with respect to that of an hypothetical junction with no heat flux wire/junction. The influence of the heat flux between the support and the wires on the junction temperature is controlled by the conductive effects, and thus, by the parameter l/l_c. The dependance of the response time with Reynolds number observed from the numerical test cases was in agreement with experimental results performed in a free jet, and with the Nusselt correlation proposed by Collis and Williams [104]. Transfer functions of the junction response were obtained for the different numerical cases demonstrating that the order of the lineal differential equation modeling the response was shown to increase with the influence of the conductive effects from the support on the junction. The response could be that of a second or third order differential linear system for l/l_c values higher than 10.

The information from the numerical characterization of the probe design employed for the test measurements, allowed to complete the estimation of the temperature uncertainties with a simplified experimental calibration,

avoiding the complexity of conventional experimental characterizations. Additionally, the correction of measurements with the overall adiabatic recovery factors numerically computed, allowed reducing the temperature error. The methodology described for the error analysis provided global systematic temperature errors of 0.2K, and random errors derived from the experimental calibration and signal acquisition of 0.1 K.

The numerical procedure developed can be used as a design tool when accurate temperature measurements are required. The procedure has been demonstrated with parametric studies directly coupled with the computer-aided-design of the probe. Therefore the geometrical/material optimization can be readily implemented by coupling the grid-solver-postprocessor with differential evolution methods, such as the one proposed by Storn and Price [106]. thermocouple probe needs to be designed, and the conclusions presented on the influence of different design parameters provide direct general design guidelines.

Chapter 4

Experimental and data reduction procedures

This chapter presents the experimental approaches followed to investigate the bypass flow heat exchanger performances. Testing procedures and data processing methodologies for the thermal and for the aerodynamic characterization are described.

The splitter geometry, reproduced at real scale, bifurcates the mass flow into the main bypass flow and the inner flow simulating the entrance of the engine core flow. This allows replicating the inlet bypass effects and the growth of the boundary layer. Figure 4.1 sketches the test section. The air under the splitter is evacuated to the atmosphere through a variable area restriction, to control the pressure distribution at the splitter and the location of the stagnation point.

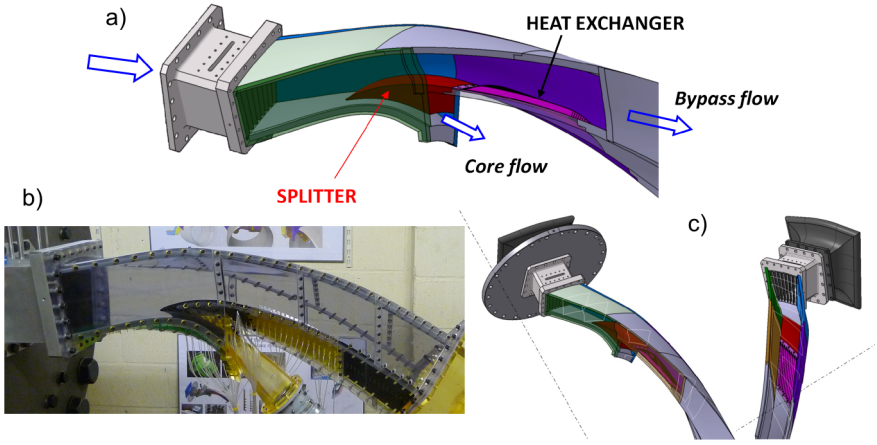

Figure 4.1: *Test section. Lateral view: a)sketch, b)picture. c)Sketch top views.*

The investigated surface heat exchangers are integrated on the splitter downstream of its leading edge. The axial variation of the radius of the splitter surface is small in this region. Three heat exchangers were tested, all composed by arrays of fins manufactured in aluminium alloy 6061-T6.

The location of the leading and trailing edges of the fins was common for the different geometries. In function of the geometry investigated, tests can be divided in four tests configurations:

- *Clean*: This configuration corresponded to the baseline bypass duct. No heat exchanger was integrated on the splitter.
- *Continuous fins I*: The heat exchanger investigated was composed by longitudinal fins characterized by triangular transversal sections with rounded edges. In longitudinal direction, the leading edge of the fins is defined by a smooth beveled contour, while the trailing edge is rectangular. The orientation was fixed by a middle fin chord plane at 40.5 degrees with respect to the local meridional plane. The intersection of this plane with the splitter surface defined the fin central line. The transversal fin profile evolves along this line, while defined at each point by the local radial direction.
- *Continuous fins II*: The heat exchanger investigated was composed by longitudinal fins characterized by rectangular transversal sections with rounded edges. In the longitudinal direction, both leading and trailing edges are rectangular. The lateral surface is defined by a plane oriented at 42 deg. with respect to the local meridional plane at each longitudinal position.
- *Interrupted fins*: In this configuration the heat exchanger is composed by small rectangular fins evenly spaced in the longitudinal direction. Both fins transversal and longitudinal sections are defined by sharp rectangular edges. The orientation was fixed by a middle fin chord plane at 42 degrees with respect to the local meridional plane. As in the *continuous fins I* configuration, the intersection of this plane with the splitter surface defined the fin central line. The transversal fin profile follows the local radial direction at each point along the fin central line.

The geometrical characteristics of the heat exchangers investigated are sketched in Fig.4.2. Fins' dimensions correspond to a transversal cut perpendicular to the fin central line.

The wind tunnel was operated at nominal conditions for all tests, corresponding to cruise engine conditions at zero altitude (aero-design point).

4.1 Thermal investigation approach

The evaluation of the cooling capacity of finned heat exchangers requires the coupling of the convective and conductive heat transfer processes within the array of fins. To this goal, the convective thermal characteristics of the fins at engine flow conditions need to be known, which was the target of the present thermal investigation.

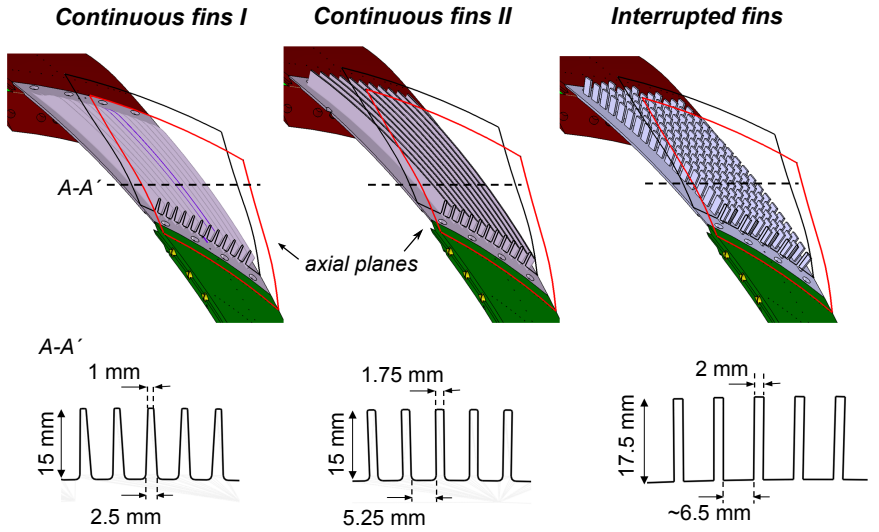

Figure 4.2: *Sketch of the different heat exchanger configurations and geometrical characteristics.*

4.1.1 Methodology for the convective heat transfer study

Experimental and numerical methods were coupled to determine the convective heat transfer characteristics. The applied methodology was based on the use of the adiabatic heat transfer coefficient h_{ad} and the associated adiabatic temperature T_{ad}, as invariant descriptors of the forced convection in high speed flows, as proposed by Moffat [107], Eq. 4.1. The benefit of using h_{ad} and T_{ad} to describe the convective process lies on their invariability with respect to changes in the thermal boundary conditions. The couple adiabatic heat transfer coefficient and adiabatic temperature are only function of the fluid dynamics dictated by the geometry and the fluid properties. Thus, measurements made in the facility under the transonic engine flow, can be used for different thermal inputs. Additionally, T_{ad} provides an estimation of the local total temperature of the flow at the edge of the boundary layer.

$$h_{ad} = \frac{Q}{T_{ad} - T_{wall}} \tag{4.1}$$

The experimental approach used to determine h_{ad} and T_{ad} consisted in measuring the heat flux correspondent to different wall temperatures, and from the relationship between the heat flux and wall temperature, extrapolating to zero heat flux to obtain the adiabatic temperature. The slope of the linear fit between the heat flux and the wall temperature corresponds to the adiabatic heat transfer coefficient. This approach has been used by Smith et al.[108] in steady conditions, and in short duration facilities at the von Karman Institute by Pinilla et al.[109] and at Oxford University by

Thorpe et al.[110]. In short duration facilities multiple tests for different initial wall temperatures are required since the wall temperature variation is rather small during a single test.

Experiments have been designed in the transonic facility to provide a high temperature difference flow-fins with the use of electrical heaters attached to the inner surface of the heat exchanger. The power of the heaters and thus, the maximum surface temperature achieved was restricted by the temperature limits of the test section wall material. The fins wall temperature distribution was recorded by means of infrared thermography (IR). The temporal evolution of the convective heat flux correspondent to each recorded fin pixel and its temperature evolution, was numerically computed accounting for the 3D heat transfer conduction within the heat exchanger. The test sequence was initiated by preheating the fins up to the maximum temperature. Once the thermal steady state was reached, the inlet valve was operated to reach the nominal steady flow conditions in the test section. The initial flow transient was minimized during the thermal tests to about 2 sec. As soon as the flow was established the electrical heaters were switched off and the temperature of the fins, while being cooled down by the flow, recorded with the IR camera. During the 30-40 sec. of the experiment in steady flow conditions, the flow temperature variation was lower than 0.8K, while the surface temperature varied by about 15 K. The temporal evolution of the wall temperature during a test is represented in Fig.4.3-a, for a certain fin pixel close to the leading edge, to depict the methodology. The time t_1 corresponds to the instant at which the heaters were switched off after the initial flow transient. At this time the fin temperature was T_1 as recorded by the IR camera, and the correspondent convective heat flux flow-fin Q_1. At time t_2 the fin temperature decreased to T_2 since it was cooled down by the flow, and the heat flux at this instant was also lower, Q_2. Fig. 4.3-b represents the correspondent values of heat flux and surface temperature obtained during a complete blow down for a certain position on the fin surface. For each fin pixel measured by the IR camera, a linear fit between the heat flux flow-fin and correspondent fin temperature was performed. The extrapolation of the fitting to zero heat flux provided at each fin position the adiabatic wall temperature (abscise for zero ordinate value), and adiabatic heat transfer coefficient (fitting slope). In the present application the variation of the wall temperature monitored during a test was large enough to compute for a single test, sufficient pairs heat flux/wall temperature as to perform a linear fit with high regression coefficient, without the need a multiple tests as required in short duration facilities.

Given the periodicity representative of the aerothermal effects on the engine bypass flow heat exchangers, the analysis was restricted in the test model to the central fin, assumed to be insensitive to the presence of the lateral walls. Due to the 3D shaped test section and test model, and the relatively large length of the fins (length/height=17.7) complete optical access to the central fin on the array was not possible. The IR field of view

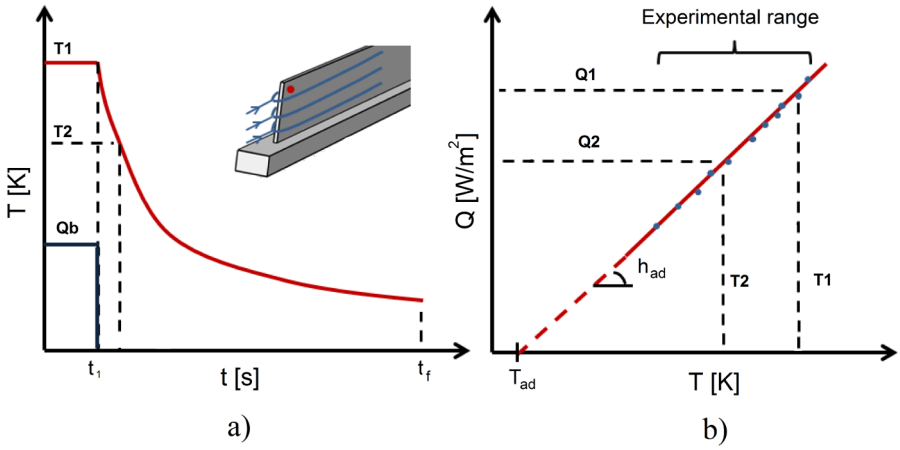

Figure 4.3: *a) Temperature evolution at a certain location on the fin, b) Linear fitting of the Heat flux (Q)-Wall Temperature (T_w) curve, for the computation of the adiabatic heat transfer invariants (h_{ad}, T_{ad}).*

was limited to the 40% of the total fin length from its leading edge. The IR camera orientation allowed temperature measurements also in the fin's base. Image post-processing techniques, as well as careful IR calibration were required. Infrared thermography was employed since it provides non-intrusive spatially resolved surface temperature distributions. IR sensors allow high levels of accuracy and resolution provided an accurate calibration is performed. For the computation of the heat flux temporal evolution at each fin pixel, the typical mono or bi-dimensional assumptions used in short duration facilities [111] can not be applied in the present case due to the complex 3D heat conduction processes within the heat exchanger and the large test duration. An innovative processing technique based on a transient three dimensional Inverse Heat Conduction Method (IHCM) [112] was used.

4.1.2 Experimental set-up and infrared thermography

Tests for convective heat transfer characterization required adapting the test section in order to provide an optical access suitable for the IR measurements, and to accommodate a heated model minimizing the conductive heat losses. In addition to the fin surface temperature measurements, the temperature evolution within the base of the fins was recorded at different positions by means of embedded thermocouples. Flow total pressure and temperature temporal evolutions at the test section inlet and outlet were also measured.

The lateral wall piece facing the heat exchanger included an adaptor to mount a germanium window of 80 mm diameter and 10 mm thickness to

provide optical access. A picture representing the test section optical access and the IR camera location is shown in Fig.4.4

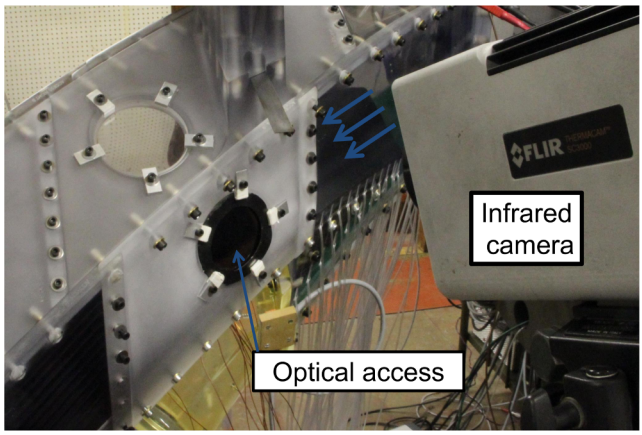

Figure 4.4: *Test section optical access and IR camera positioning.*

In order to minimize the heat transfer losses through the inner surface of the heat exchanger to the wind tunnel and environment, a special support was designed. An air cavity was allocated between the heat exchanger base and a 3D support adapted to the inner test section geometry. The support was manufactured by rapid prototyping of a resin that provided high temperature operational limits, and very low conductivities. This arrangement provides sufficient space to accommodate the adhesive surface heaters attached to the base of the fins, and the cabling of the embedded thermocouples. Direct contact between the heat exchanger and holding frame or lateral walls was eluded by the use of an insulating material (PTFE, teflon). Numerical simulations were performed for the design of the heaters to estimate the required heat power to reach the maximum model temperature imposed by the maximum operational temperature of the wind tunnel walls (50^oC).

The wet surfaces of the heat exchanger were painted in black to increase the fin emissivity and to reduce the reflectivity. The fins were instrumented with adhesive surface thermocouples distributed on the IR visible part of the surface cooler, to assist the calibration of the infrared camera. Flexible electrical heaters (Minco HK5286R3) were attached to the inner surface of the aluminium heat exchanger model. Nine T-thermocouples were embedded on the base of the fins at different axial and circumferential positions. All the thermal sensors involved were calibrated simultaneously, after their implementation on the surface cooler, in a calibration oven. Three type K-

thermocouples (previously calibrated in an oil bath) were distributed along the heat exchanger length close to its surface during the oven calibrations to increase the accuracy of the calibrations.

All thermocouple sensors used (type T) were connected to an electronic ice point reference unit to minimize the cold reference junction error. The Isotech TRU (Thermocouple Reference Unit) 937 (model 100) supplied a 0^oC reference temperature with an stability of $\pm$ 0.03^oC. The thermocouple signal was amplified and filtered in a signal conditioning box with a gain of about 2500 and a low pass filter at 10 kHz. Pressure lines from the aerodynamic probes were connected to Validyne DP15 sensors. Pressure and temperature signals were analogically filtered at 125 Hz and sampled at 500Hz by a high speed acquisition system in continuous mode during the blown-down test. In the same acquisition system also the power imposed on the heaters was recorded in order to determine the exact moment at which the heaters were turned off. The images recorded with the infrared camera (FLIR SC3000) were sampled at 50 Hz with a full resolution of 320 by 240 pixels. Synchronization between the camera and the pressure and temperature readings was obtained by triggering the camera with the main acquisition system. The acquisition was started before the starting of the blow-down.

Infrared camera calibration was performed in-situ in order to overcome the limited knowledge on the parameters determining the incident radiation onto the infrared camera [113]. To avoid large temperature gradients the calibration was performed in no flow conditions by imposing different levels of power on the surface heaters. The wall temperature of the different surfaces observed (lateral fin surface and base) was extrapolated from the local thermocouple readings to the surrounding image pixels. A correction matrix was first obtained at ambient temperature to correct for the variation of the angles of view and out of focus points. The correction factor was extrapolated from ambient temperature to the temperature range of the experiments.

4.1.3 Inverse Heat Conduction Method

The complexity of the 3D heat transfer effects within the finned heat exchangers, together with the unsteadiness of heat transfer process analyzed, implied the necessity of using inverse heat flux methods to determine the convective heat flux on the wet surfaces from the surface temperature measurements.

Inverse heat conduction problems are mathematically ill-possed and their stability is strongly affected by unavoidable noise in the measurements. Colaço [114] presented an overview of techniques dealing with inverse heat conduction methods. The mathematical methods presented in the literature to solve inverse problems involve the reformulation of the ill-posed equations using regulatization [115, 116] and optimization techniques [117]. Finite dif-

ferential methods are commonly involved in the inverse problems to solve the heat transfer equations. The IHCM used for this application developed by Sousa et al.[112] is based in an iterative regularization, proposed by Alifanov [116], that uses a conjugate gradient method (CGM) with the adjoint problem as a minimization technique. The 3D heat transfer equation was solved with a commercial code, COMSOL multiphysics®, working as a subroutine of the inverse algorithm. This link allows to model complex geometries and to work with different boundary and initial conditions.

The thermal analysis was focused on the central fin of the *continuous fins II* configuration, assuming periodicity and avoiding the influence of the lateral test section walls. The commercial finite element solver COMSOL was used to solve the three dimensional heat conduction problem on the solid domain. In order to simplify the numerical domain, the slight curvature of the model caused by its implementation on the splitter cylindrical surface was neglected. An sketch of the geometrical simplification from the 3D heat exchanger geometry to the straight fin considered for the numerical thermal analysis is sketched in Fig.4.5.

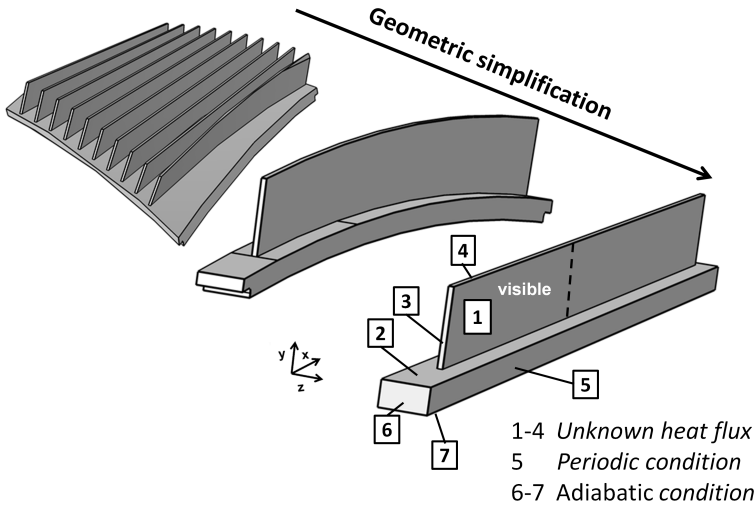

Figure 4.5: *Heat exchanger fin model for numerical heat conduction solver and boundary conditions.*

The boundary conditions imposed on the fin model were: periodic boundary conditions in the lateral base surfaces, adiabatic walls in the upstream and downstream base surfaces as well as in all the inner base surface, and unknown heat flux in the wet surfaces (the fins' surfaces and top base surface), Fig.4.5. Since the field of view for the IR temperature measurements

was limited to the frontal 40% of the fin, the numerical domain was divided in a visible and non visible part, as represented by the dotted line in the same figure.

The raw images obtained with the IR camera were post-processed to provide the input temperature information as required by the numerical method used to compute the convective heat transfer characteristics. A raw image as provided by the IR camera is shown in Fig.4.6a. A perspective transformation was first performed. The spatial resolution was reduced to increase the computational time leading to a matrix of 70 by 7 pixels on the visible part of the lateral fin surface, the total lateral area corresponding to 111 by 7 pixels. The subdivisions on the observed surfaces in which temperature information was averaged in each time step are sketched in Fig. 4.6b.

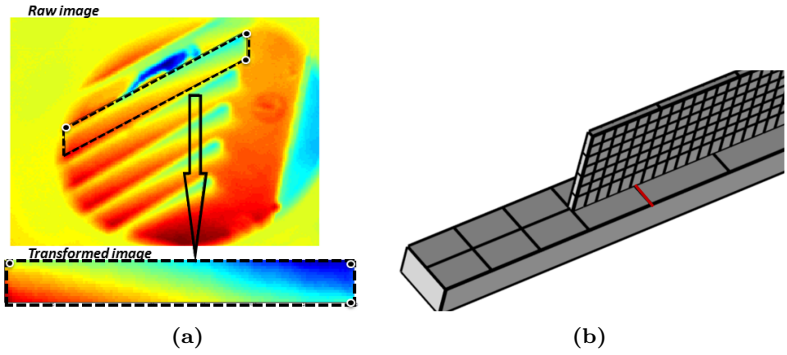

Figure 4.6: *a)Image perspective transformation, b)Area subdivision on lateral and bottom surfaces for numerical calculations.*

The evolution of the heat flux distribution on the wet surfaces was computed by the inverse heat conduction method, from the input temperature distributions measured by IR thermography on the same surfaces. The IHCM is based on an iterative regularization in which an optimization technique (CGM) is used to minimize the objective function defined by Eq.4.2. The objective function quantifies the squared difference between the measured temperature Y(x,y,t) and the estimated one T(x,y,t), at each time step between t_i and t_f defined by the time window of the transient process analyzed.

$$R[Q(x,y,t)] = \int_{t=t_i}^{t=t_f} \sum_x \sum_y [T(x,y,t) - Y(x,y,t)]^2 dt \qquad (4.2)$$

The computational methodology is sketched in Fig.4.7. The computation is started by a random initial guess for the heat flux $Q_0(x,y,t)$ on the boundaries defined by unknown heat flux boundary conditions (no initial information of the unknown heat flux is required). The 3D finite element

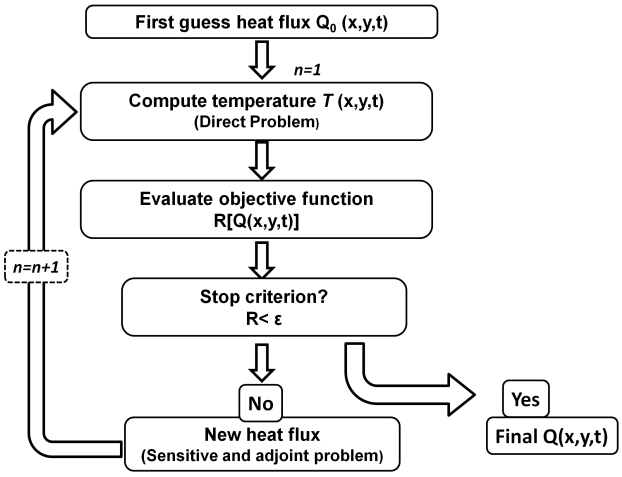

Figure 4.7: *Methodology for heat flux computation based on IHCM.*

solver is used to solve the direct problem using this initial boundary condition, providing the first estimation of the temporal temperature distribution T(x,y,t). The objective function is evaluated and if the convergence threshold is not satisfied, a new heat flux is computed. This process is iterated until the stopping criterion is satisfied. The threshold (ε) for the convergence of the objective function was determined based on the standard deviation σ of the IR measurements, Eq.4.3, where M is the total number of spatial measured points. Computations are performed in the complete numerical domain, although the evaluation of the objective function is restricted to the visible part.

$$R[Q(x,y,t)] < \varepsilon, \qquad \text{with} \qquad \varepsilon = M\sigma^2 t_f \tag{4.3}$$

Numerical validation of the inverse heat conduction method applied to the present application allowed estimating the accuracy of the data processing technique [118]. The validation test case involved step gradients of heat transfer coefficients in order to test the capabilities of the method to numerically unfavorable conditions. Maximum temperature errors were lower than 4K and 2K for the fin and base surface respectively. Maximum errors on the heat transfer coefficients were lower than 10% in most of the domain.

4.2 Procedure for the aerodynamic characterization

The flow characterization was addressed by measurements at several representative positions. Intrusive instrumentation was used to measure time-

averaged flow properties and different data reduction methodologies were implemented to evaluate local and global flow effects, as well as balances of losses between different sections.

To this goal map measurements of total pressure and temperature, static pressure, Mach number, flow direction and turbulence intensity were performed at different measurements planes along the test section, for the different test configurations. To minimize the blockage, for each test only one aerodynamic probe was inserted at a certain measurement plane for a given test configuration. During the test the probe was translated within the plane to map the investigated property. Additionally wall pressure measurements at the inner walls (splitter surface and inlet shroud) were performed along the test section mid-line and circumferentially at the axial location of the measurement planes. Mid-line wall pressures were likewise measured at the entrance of the inner core flow, together with total pressure and temperature upstream the area restriction, and at the entrance of the deswirl duct. The operation of the engines for the instrumentation positioning and the different acquisition systems used was synchronized within a control software developed for the aerodynamic testing.

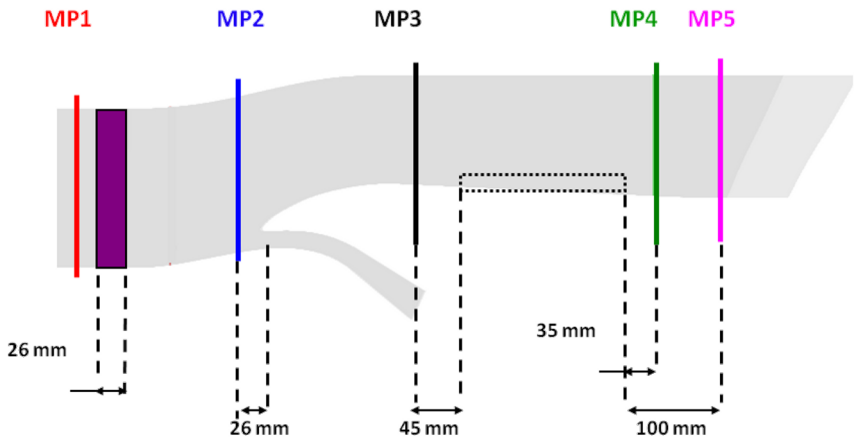

Figure 4.8: *Measurement planes location, meridional view.*

Fig.4.8 displays the five measurement planes, perpendicular to the engine axis, and their axial distances to representative test section locations (IGVs TE, splitter LE, ACOC LE and TE). *Plane 1* (MP1) rendered the reference pressure and temperature levels at the entrance of the test section, upstream the inlet guide vanes. The engine flow downstream of the inlet fan and upstream the bifurcation bypass/core flow was characterized by measurements at *plane 2*. *Planes 2* and *3* provided information about the flow development at the bypass entrance. The heat exchanger location was bounded by measurement *planes 3* and *4*. *Plane 3* rendered the inlet flow conditions

for flow balances upstream/downstream of the heat exchangers. The development of the flow structures caused by the heat exchangers was analyzed from the flow evolution from *plane 4* to *plane 5*.

4.2.1 Instrumentation and measurement chain

Measurements were performed by means of intrusive instrumentation specifically designed for this application, consisting on: rakes of shrouded Pitot probes, five-hole probes, thin wire shielded T-thermocouples, hot-wire probes, and reference probes combining a shrouded Pitot probe and a shielded T-thermocouple. The design criteria and characteristics of the probes are described in section 3.3.

Three types of differential pressure transducers were used for the pressure based measurements. Three Scanivalve ZOC33 miniature pressure scanning modules (64 channels each) were used for the wall pressure measurements. Pressure lines from aerodynamic probes were connected to Validyne DP15 variable reluctance transducers and piezoresistive transducers (ASM 5812-0050) of different range, allowing duplicated readings. Given the variability of the pressure levels registered by the five-hole probe signal duplication on sensors of different range allowed maximizing the resolution on the measurements without missing information by punctual saturation in one of the transducers. Plastic pipes of 1.1 mm internal diameter were used for all pressure lines. Five-hole probes were calibrated in a free jet facility within the angular range ±26 deg. for yaw and 0-44 deg. for pitch, each 2 deg. Calibrations were performed for Mach numbers from 0.55 to 0.8, each 0.05 ΔM. The sensitivity of the Pitot probe rake to pitch and yaw angles was analyzed in the same facility for the same angular range. The measured total pressure showed to be insensitive to the flow-probe yaw angle within the calibration range, and also to pitch angles up to 40 degrees. Maximum total pressure error at 44 pitch degrees was 2%.

The measurement line for the type T-thermocouples was identical to the one described in the thermal set-up. The thermocouples were calibrated in an oven after probe manufacturing. To ensure temperature uniformity during the calibration the rake was covered by a cylindrical capsule opened in the bases and type K thermocouples (previously calibrated in an oil bath) were inserted facing each rake junction. Special attention was paid to minimize calibration errors, as well as conduction errors by deep immersion and isolation of the rake on the oven.

Two different control modules were used for the hot-wire probe rake: the Dantec StreamLine Pro Anemometer System operated in CTA (Constant Temperature Anemometry) mode was used for the three lower heads, and VKI control circuits based on constant OHR (Over Heat Ratio) for the remaining heads. Cut-off frequencies were 30 kHz for the Dantec system and about 13 kHz for the VKI control units. Hot-wire calibrations were performed in a calibration nozzle jet of 12 mm diameter connected to an

air heater. Calibrations were performed varying both the total pressure and temperature in the nozzle settling chamber, for the range of flow velocities encountered during the tests. This allowed wire temperature corrections during the postprocessing of the hot-wire signals. Angular sensitivity was also accounted during the calibrations.

4.2.2 Instrumentation positioning and traverse mechanisms

Aerodynamic probes were inserted at the measurement planes through a slot in the upper test section wall and fixed to a carriage actuated by a two axes traversing mechanism. A flexible steel sheet was used to close the gap formed as the probe moved in circumferential direction within the slot.

Two angles defined the probe orientation at each measurement plane. The angle of insertion (φ) defined by a rotation around the engine axis (opposite direction), and the orientation of the probe head defined by a rotation around the stem axis (ϕ). The angular zero reference is the vertical direction for φ, and the axial direction for ϕ. The values of the angles defining the probe orientation at each measurement planes are given in Table. 4.1.

	Plane 2	*Plane 3*	*Plane 4*	*Plane 5*
φ, [deg.]	46	29	27	26
ϕ, [deg.]	-6.49	-4.17	6.83	9.98

Table 4.1: *Angles defining the probe orientation at the measurement planes.*

Probes were moved along two axis defined by the probe direction of immersion (y') and its perpendicular (x'). Coordinates within the plane are referred to those axis and correspond to the location of the probe head central point. The origin in (x') was defined at the center of the measurement plane circumferential span, and positive values were considered towards the inlet test section meridional plane. Removable pins limiting the movement of the stem within the slot served to set the probe at the x' reference position. In the (y') direction the zero reference is linked to the last head central point, common for all probes independently of the distinct head geometries. The reference position was fixed as the position for which the minimum distance between all probes and the splitter is 1 mm. Positive values of y' are considered towards the splitter. Johansson gauges with a precision of 0.005 mm were used to set the probes at the reference position by adjusting the minimum distance probe/splitter, different for each probe and plane.

The probe is operated by two *Maxon A-max motors*, controlled by a Maxon Motor Control Box with electronics EPOS 24/5. The motion system was preprogrammed to pass through a set positions defined in the plane local coordinate system. The engines were stopped at each predefined position while measurements were acquired, and then moved to the next point.

The precision on position of the engines was 1/64 mm. Both engines were operated simultaneously. The complex shape of the measurement sections impeded the imposition of maximum and minimum engine positions for safety considerations.

Measurement points within a plane were limited by the maximum test duration. In order to maximize the measurement area but also to increase the spatial resolution specially in the central region close to the splitter, grids with three different levels of refinement were designed. They are referred as *coarse*, *fine* and *ultrafine* grids. Due to the different number of heads composing the rakes, the distinct distance between heads for the five-hole, and the different geometry of the planes, measurement grids were designed for each rake and plane. For each type of grid and plane the distance between the evenly spaced points in the *x'-y'* coordinates is indicated in Table 4.2. The distance between points in the *x'* direction is the same independently of the rake. However in the *y'* direction the distance between points is different for the five-hole probe rake (between brackets) than for the rest. The maximum measurement span in x' was 90 mm. The closest measurement point to the lateral walls was limited to 12 mm, and to 20 mm to the upper wall. The closest measurement to the splitter wall, 1 mm, was provided by the Pitot probe.

		Plane 2	*Plane 3*	*Plane 4*	*Plane 5*
coarse	x'	8	9	8	7
	y'	12 (18)	12 (18)	12 (18)	12
fine	x'	4	4	2	2
	y'	6 (10)	4 (4)	4 (4)	4
ultrafine	x'			1	
	y'			2	

Table 4.2: *Distance between measurement points for the different measurement planes and type of measurement grids, [*mm*]. Values between brackets correspond to the five-hole probe rake.*

4.2.3 Test sequence and data acquisition

Tests were performed for the different test configurations, at the four measurement planes, with the different probe rakes, and with measurement grids of different level of refinement. A reference probe was fixed at *plane 1* during all the tests, providing the inlet reference flow conditions: total pressure and temperature temporal evolutions. Given the dependance of the absolute pressure levels and the inlet flow temperature on the daily ambient conditions (atmospheric pressure and temperature), the reference conditions at the test section inlet were essential to accurately correlate the measure-

ments from different tests. To minimize blockage, only one probe rake was immersed in the flow during each test. Wall pressure measurements along the test section were recorded for every test.

Different data acquisition systems were used, only one of them in continuous mode recording the reference inlet conditions, the outlet temperature at the inner core flow, the settling chamber pressure and the readings from the thermocouple rake. This high speed acquisition system (DAQ1) allowed analogical signal filtering. Signals were sampled at 1kHz and low pass filtered at 250 Hz to avoid aliasing. It was controlled from an independent computer. Another acquisition system (DAQ2) was dedicated to the probe rake readings, and to the duplication of the reference conditions. It performed discrete acquisitions during the steady state of the probe at a given position, 1 sec. The sampling frequency depended on the type of measurements: 1kHz for pressure and temperature measurements, and 90kHz for hot-wire measurements. The data was transferred after each discrete acquisition to the main computer from which the experiment was controlled. All the pressure based measurements (wall pressures as well as duplicated aerodynamic probe readings) were connected to three Scanivalve ZOC33 miniature pressure scanning modules that were controlled by three Scanivalve Digital Service Modules DSM34000. Those modules incorporate an embedded PC that sampled the pressure signals at 240 Hz during the probe steady position, performed an average of each of the 180 pressures acquired, and transferred the averaged values the main computer. Synchronization was ensured by a control software developed in LabVIEW platform that communicates with the different acquisition systems and the engines software.

Prior to the test, the engines reference is linked to the correspondent zero reference for the particular plane and probe. Both the DAQ1 and the control program are started before the inlet valve opening. When launched, the control program reads the preselected file containing the coordinates of the measurement points on the grid for the particular test, and communicates to the engines software to move to the first target position. Both engines are displaced simultaneously and provide a feedback signal to the main program when stopped. The main program stays armed waiting for a manual trigger signal. The inlet valve is then operated to reach the target pressure in the settling chamber. Once the flow is stabilized the main control program is triggered, and communicates with the engine software to move to the next point in the displacement input file. Once the feedback from the engines is received, and after a predefined delay time larger than the probes response time, the main program triggers the acquisition of the scanner modules and DAQ2 and sends a trigger signal recorded by DAQ1. The control program waits the data transfer to the main computer from the scanner and DAQ2 after the acquisition, and communicates with the engines to move to the next point. This process is repeated until the last point of the displacement file is reached. This last point was preprogrammed as a safety point far

from the test section walls. During the discrete acquisitions the control program stores the information from the scanners and from the DAQ2 in two different files were the information from the consecutive measurement locations is accumulated.

4.2.4 Data processing

Specific post-processing tools were developed for each type of probe to analyze the the large amount of experimental data collected during each test. Conventional post-processing (filtering, calibration, averaging) was performed to provide for each test a set of measurement positions and their correspondent averaged flow data.

To compensate for the variation of the exhaust atmospheric pressure, all pressure measurements (probe and static pressures at the walls) required to be referred to the test section inlet total pressure measured at *plane* 1 (P_{ref}). Temperature measurements from different tests are compared in terms of temperature ratios. Measurements derived from the thermocouple rake are referred to the free flow temperature during each test in order to compensate for the temporal variation of the inlet flow temperature.

Routines involving coordinate system transformations were also required to associate each local measurement plane coordinate system to the global engine cylindrical coordinates. System transformations were particularly important for flow direction measurements. Flow angles are provided by the five-hole probe data reduction procedure with respect to the probe reference system, and translated to a local cylindrical system defined at each point within a measurement plane and related to the local radial, circumferential and axial flow velocities. The required transformations are described in section 3.1.5.

Flow balances between measurement planes were estimated by one-to-one comparison of cell area averaged flow properties. The methodology used to provide for each measurement plane cell area averaged values consisted in several steps: mesh generation on each measurement plane, data interpolation combining results from different measurement grids, assignation of interpolated data to cells, and area averaging within each cell. The mathematical procedure followed to divide each measurement plane contour in 2^{2n} cells is based on n iterative subdivisions of non overlapping trapezoidal domains, by means of operations with diagonal and symmetric matrices. The input data for the automatic grid generation were: the number of iterative subdivisions n, and the coordinates of 2^n+1 equally spaced points on each of the four curves defining the the measurement plane contour. The procedure starts by building a symmetric matrix with the four vertex of the contour on its diagonal, and the middle points of each boundary. The intersection of lines defined by opposite midline points is a vertex for four new cells. Each cell is defined by a new symmetric matrix built from coordinates within the external contour, and new coordinates computed from bisection operations.

The same procedure is applied to the each new cell, and repeated n times. This procedure allowed to create $2^n \star 2^n$ cells of similar area besides the irregularity of the 2D contour.

Chapter 5

Bypass flow and surface heat exchangers aerothermal analysis

This chapter presents the analysis of the bypass flow developing along the test section and its aerodynamic and thermal interaction with the investigated surface heat exchangers. The experimental results are organized in two blocks. The first block addresses the overall aerodynamic effects caused by the heat exchangers, as well as the analysis of the flow along the test section in the absence of fins. The second block is dedicated to the heat exchangers performances, considering both the thermal and the aerodynamic behavior. The results are used in the final part of the chapter to estimate the impact of heat exchangers on current turbofans.

The maximum errors associated to the flow measurements, based on the range of flow conditions along the wind tunnel, were about 0.4% (lower than 1 mbar) for direct pressure measurements, 10 and 2.6 mbar for total and static pressures respectively (about 4% and 1.3%) derived from the five-hole probes, 0.0035 in the case of absolute Mach numbers (0.45%), and 0.9 degrees for flow angles (section 3.1.6). Global uncertainties on flow temperatures were lower than 0.3 K (3.2.6), and maximum errors on the turbulence intensity calculations were estimated about 4%.

Flow contours presented through this section are indicated in local $x^{'}$-$y^{'}$ coordinates, defined by the traverse mechanisms at each measurement plane (section 4.2.2). Radial distributions were computed by circumferential averages within a 1 degree annular sector at the center of the contours.

5.1 Performance of the bypass channel flow

5.1.1 Inlet conditions and overall heat exchangers aerodynamic effects

The inlet flow upstream the IGVs (*plane 1*) was assumed to be axial and uniform because of the large size and axi-symmetry of the settling chamber and the downstream contraction. Pitot rake measurements covering 80% of the inlet radial span, confirmed total pressure uniformity to be similar to the inlet total pressure variability during a typical test, i.e. 1.2 % of the measured differential pressure (2.4 mbar). Spatial temperature variations

were of the same order than the uncertainty on the temperature measurements. Profile measurements of inlet turbulence intensity provided mean inlet values of 1.96 %, with a variation along the span below 7%. On the other hand the variability in the inlet turbulence intensity for all the tests was similar to the variation during a typical test, lower than 7%. Angle radial profiles derived from the five-hole probe rake provided null values of pitch and yaw angles, corroborating the inlet axial flow direction.

The repeatability of flow conditions for a certain test configuration was ensured within 1% in terms of inlet Mach number.

5.1.1.1 Heat exchangers effect on inlet mass flow and Mach number

Nominal operational flow conditions were defined from the calibration tests performed in the *clean* test configuration. The calibration of the wind tunnel fixed the required inlet total pressure in function of the exhaust atmospheric pressure independently of the test configuration. The inclusion of an object within a transonic channel alters the mass flow and flow velocity and hence, the induced pressure recovery. This is characteristic of any channel flow, both within the engine bypass duct or in the ground facility. The magnitude of the flow modifications depends on the blockage effects, which are larger in the current test section. An effective flow area reduction of about 2.6 % caused by the presence of the heat exchangers in the test section corresponds to about 0.8 % area reduction within a turbofan of BPR 6.

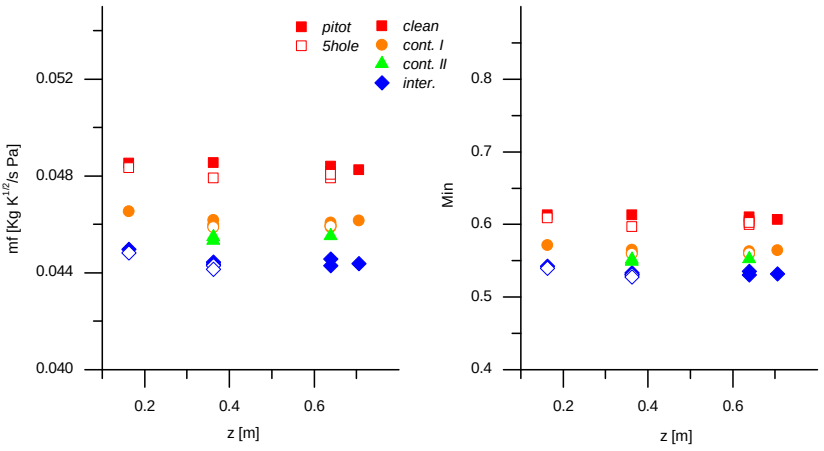

Figure 5.1: *Corrected mass flow (left) and Mach number (right) at the test section inlet for the different fins configurations and probe locations.*

The overall aerodynamic effect of the different test configurations on the transonic channel is shown in Fig.5.1. The test section inlet mass flows and

inlet Mach numbers are represented in function of the axial position of the measurement planes. Values were computed from the total and static pressures, and local geometric characteristics, measured at *plane 1*. In order to study the existence of global flow modifications caused by the instrumentation, two type of probe rakes were immersed at the different planes. Each data point corresponds to one independent test, with either the Pitot (filled symbols) or the five-hole (no-filled symbols) probe rake. The different symbols correspond to the test configuration. Inlet mass flows are corrected with the actual total pressure and temperature to compensate for day to day variations.

For a given test configuration, independently of the probe rake and plane, the corrected inlet mass flow was constant within 1% and the inlet Mach number within 1.5 %. In this context, the global flow modifications caused by the instrumentation were neglected. The presence of the different heat exchanger models in the test section reduced both the inlet mass flow and Mach number. Deficits with respect to the *clean* configuration are summarized in Table 5.1, together with the correspondent geometrical area reduction. The minimum flow effective area along the test section exists in the region where the models were located. Thus, area deficits were computed by comparison between the minimum geometrical area of a plane perpendicular to the mean flow direction in the *clean* configuration, with the area of a plane at the same position in the presence of the fins. The highest flow modification were caused by the *interrupted fins* configuration although the largest area reduction corresponded to the *continuous fins I* configuration, which involved the weakest flow modifications. Each heat exchanger model investigated had different geometrical characteristics, and induced a different local flow structure, making the geometrical local area reduction a poor parameter to correlate the global flow effects.

Dimensional values of inlet mass flows are about 3.4, 3.21, 3.20 and 3.12 $kg \cdot s^{-1}$, for *clean*, *continuous fins I*, *continuous fins II* and *interrupted fins* configurations respectively.

	$\Delta \dot{m_{in}}\%$	$\Delta M_{in}\%$	$\Delta A_{\perp}\%$
Continuous fins I.	4.5	7.1	2.75
Continuous fins II.	5.7	8.9	2.45
Interrupted fins.	7.7	11.8	2.57

Table 5.1: *Reductions of inlet mass flow and Mach number, and flow area, caused by the heat exchangers with respect to the 'clean' bypass flow.*

5.1.1.2 Mean flow velocity evolutions and mass flow bypass-core redistribution

The evolution of the mean flow Mach number at the different measurement plane axial positions for different test configurations (different markers) is represented in Fig.5.2. Mach values were computed from the Pitot total pressure measurements at the center of the planes and wall pressures at the same axial position. From *plane 1* (inlet) to *plane 2* the flow was similarly accelerated for all configurations regardless of the different inlet Mach number. In the absence of fins the flow reached its maximum velocity at *plane 3* and remained at slightly lower Mach numbers in *planes 4* and *5*. However in the presence of fins the flow reaches its maximum velocity at *plane 4* before being slightly decelerated at *plane 5*.

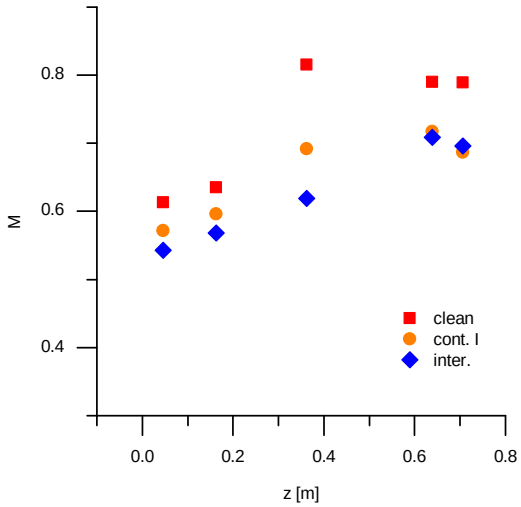

Figure 5.2: *Mean Mach number evolution along the test section for the different test configurations.*

Pitot and wall pressures, as well as total flow temperature measurements, both in the main bypass flow and within the inner exhaust were used for mass flow calculations, together with the geometrical characteristics of the two ducts. About a 98% of the inlet mass flow was estimated to be directed to the main bypass flow channel in the *clean* configuration. This value was reduced to 95% and 94% for *continuous fins I* and *continuous fins II* respectively, and to about 92% for the *interrupted fins* configuration.

Relative dynamic pressure distributions were similar in all cases upstream the heat exchangers except in the inner part of *plane 2* facing the inner exhaust. Contour levels of dynamic pressure derived from the five-hole probe in this limited region for *clean*, *continuous fins I* and *interrupted fins* config-

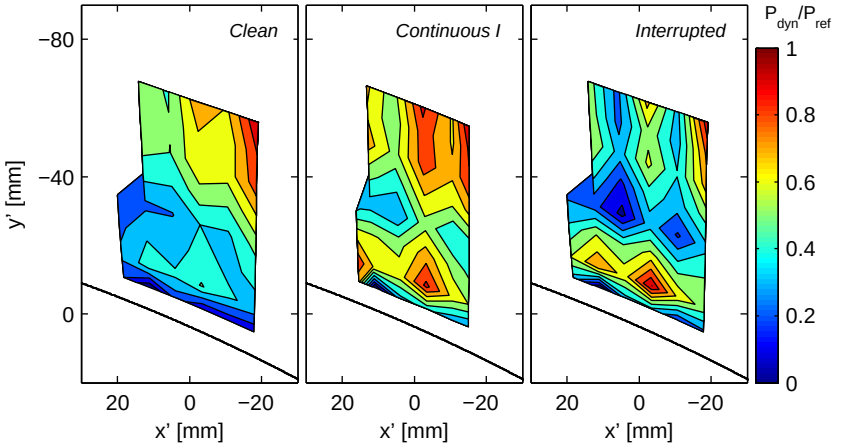

Figure 5.3: *Contours of non dimensional dynamic pressure at measurement* plane *2 in the region upstream the core flow bifurcation.*

urations are shown in Fig.5.3 non dimensionalized with the full span of the dynamic pressure variation in each case. As the total mass flow through the test section decreased, the relative dynamic pressure distribution increased in the inner region. The geometrical characteristics of the inner duct and exhaust pressure being invariable, the mass flow through the inner duct was approximatively constant independently of the global mass flow.

5.1.2 Test section flow structure

Highly swirling flows as the flow downstream of the inlet fan, are characterized by the existence of strong radial pressure gradients dictated by the design radial equilibrium law. Along the bypass flow duct, the variation of radius of the inner wall added further complexity to the swirling flow, causing the longitudinal modification of the radial flow gradients. The current research required the precise duplication of the bypass flow gradients given the importance of secondary flows on the thermal characteristics and flow-surface interactions. Comparison of flow measurements on the *clean* configuration and the 3D CFD computations validated the replication of the turbofan bypass flow within the test section.

The IGVs dictated the inlet time averaged angle distributions with mean swirl angles equal to 44 degrees, and with a variation along the radial span of 4 degrees. Their evolution along the duct was preserved thanks to the geometrically optimized test section. However, the low velocity flow within the lateral boundary layers was deviated towards the suction surface affecting the splitter boundary layer. The influence on the splitter boundary layer increased along the test section as the thicknesses of both the lateral and the

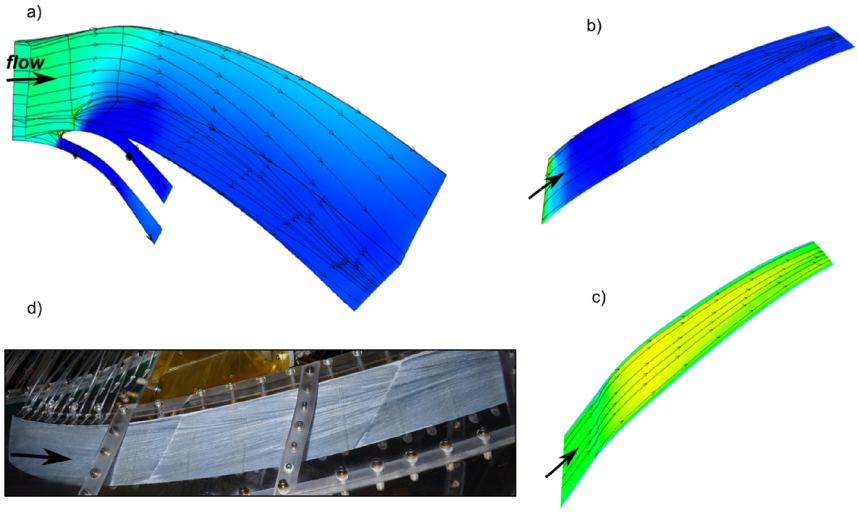

Figure 5.4: *Wall streamlines from numerical computations: a) test section lateral walls, b) splitter surface, c) surface parallel to splitter at 10 mm. d)Streamlines from oil flow visualizations over the splitter for 'clean' test configuration.*

splitter boundary layers increased. Thanks to the flow acceleration over the splitter, limiting the growth of its boundary layer, lateral wall effects up to *plane 3* were only weakly observed. Up to this position at least the 80% of the test section circumferential span was free of lateral effects. Downstream of *plane 3* the influence of lateral wall effects was different for each test configuration due to two dissimilar channel flows developing in the presence of fins. Oil flow visualizations over the splitter demonstrated that for the most restrictive case (no heat exchangers), the central 40-50% of the circumferential span remained unaffected by the lateral secondary flows. This was also confirmed by map measurements downstream of the location of the heat exchangers.

Flow streamlines along the bypass channel walls from the numerical analysis, as well as from oil flow visualizations over the splitter, are represented in Fig.5.4 to illustrate the influence of the secondary flows. Oil flow visualizations also ensured the absence of separation along the splitter surface, a serious concern in transonic flows in curved channels [119].

5.1.3 Clean bypass flow development

5.1.3.1 Velocity magnitude along the test section.

The distribution of isentropic Mach number along the test section center line is represented in Fig. 5.5, along the axial coordinate. Isentropic Mach numbers were computed from the averaged local static to inlet total pressure ratio. Downstream of the IGVs the flow is slightly accelerated up to the splitter leading edge, from M_{is} 0.6 to 0.63. Below the splitter, the flow is diffused prior to the inner exhaust duct. Above the splitter, the flow is accelerated from its leading edge as the surface radius increases, reaching a plateau of M_{is}=0.85 upstream the location of the heat exchangers. Downstream of this position and after a slight expansion, the M_{is} remains almost constant. From the location of the fins leading edge up to the exhaust M_{is} varies merely from 0.8 to 0.79. The uncertainty on the pressure measurements is translated to M_{is} uncertainties of about 0.2 %. Error bars represent the standard deviation of the measurements during a test for each individual sensor. Maximum std values of 1% M_{is} are in agreement with the Mach number variability during a test computed at the test section inlet.

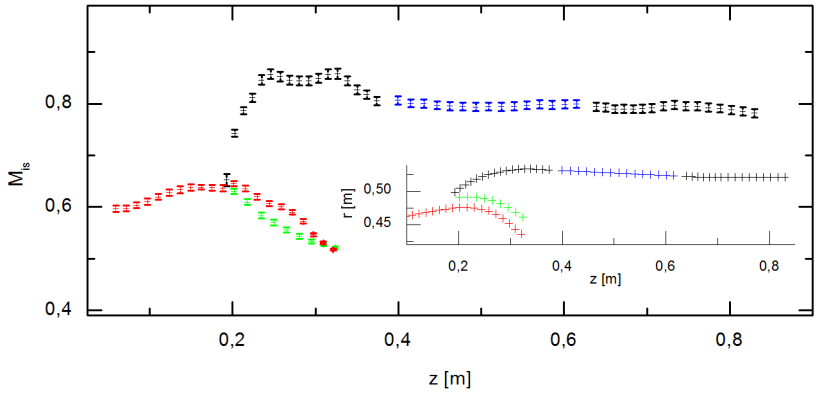

Figure 5.5: *M_{is} along the test section mid-line.*

Contours of absolute Mach number at measurement *planes 2* to *4* derived from five-hole probe measurements are represented in Fig. 5.6. Additionally, the correspondent radial distributions of Mach number are shown in Fig.5.7.

In *plane 2*, the flow velocity is rather homogeneous, with a mean Mach number equal to 0.63±3%. Lower velocities correspond to the inner part of the contour, facing the core flow under the splitter. The flow is accelerated in the main bypass channel presenting the highest Mach numbers at *plane 3*. Disregarding the flow in the vicinity to the splitter, negative radial gradients are observed in *planes 3* and *4*, with maximum Mach variations of about 4%. The main difference between those two planes was due to the influence

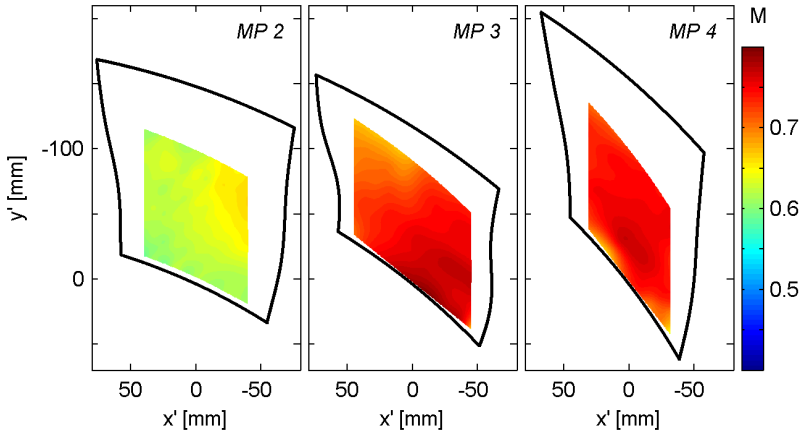

Figure 5.6: *Contours of absolute Mach number at measurement planes 2 to 4, 'clean' configuration.*

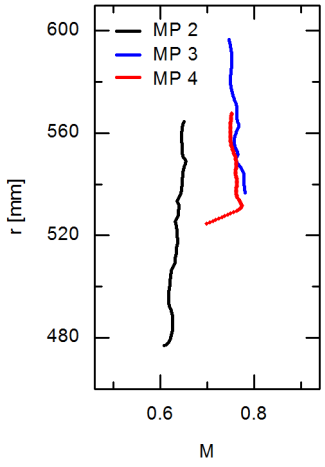

Figure 5.7: *Radial distributions of Mach number at measurement planes 2 to 4, 'clean' configuration.*

of the splitter geometry on the boundary layer development. While at *plane 3* no flow deceleration was detected close to the wall, a 9% Mach number reduction was measured in the inner 8 mm in radial direction in *plane 4*.

5.1.3.2 Flow direction along the test section.

Flow angles were related to local radial, circumferential and axial velocity components at each measurement point. The orthogonal reference system considered is such that pitch values are positive when the radial velocity component is negative.

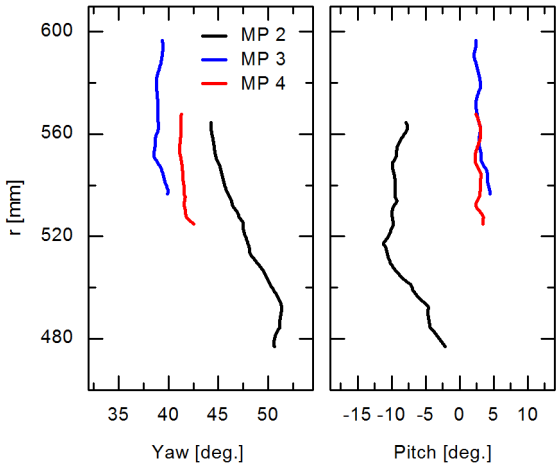

Figure 5.8: *Radial distributions of yaw and pitch flow angles at measurement planes 2 to 4,'clean' configuration.*

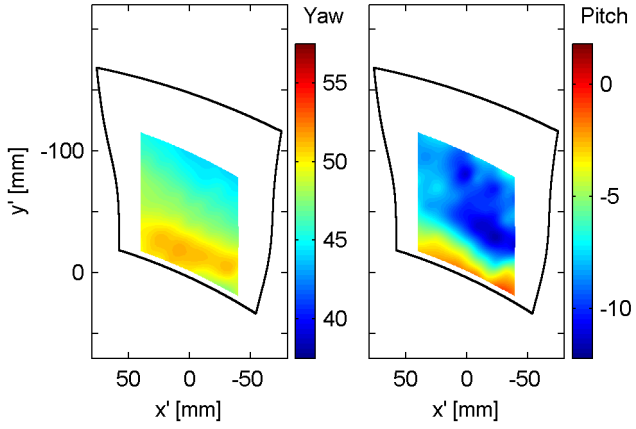

Figure 5.9: *Yaw and pitch angle map distributions at 'plane 2'.*

Radial distributions of yaw and pitch angles at measurement *planes 2* to *4* are represented in Fig.5.8. The flow swirl is inversely related to the flow

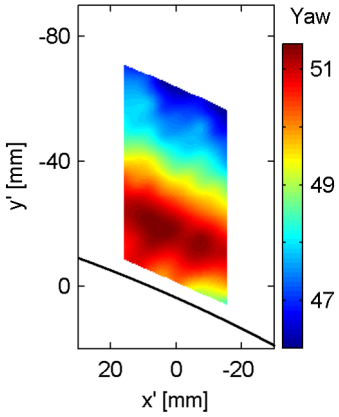

Figure 5.10: *Contour of Yaw angle at 'plane 2' in a limited region upstream the inner core bifurcation.*

velocity. Highest and lowest yaw angles were observed in the planes where the flow velocity was lowest (*plane 2*) and highest (*plane 3*) respectively. The evolution of the pitch angle is dominated by the splitter geometry.

Contours of yaw and pitch angles at *plane 2* are represented in Fig.5.9. The orientation of the flow in the inner region is affected by the presence of the splitter and the inner duct. Those effects do not prevent the reproduction of the engine flow orientation in the part of the flow facing the main stream: negative yaw gradients with mean angles about 45 degrees and 4 degrees maximum variation, and slightly positive pitch gradients with -11 degrees mean value. Small yaw angle variations in circumferential direction due to the wakes of the inlet profiles were observed in *plane 2*, as depicted in the zoomed region in Fig.5.10.

Contours at *planes 3* and *4* of yaw (a) and pitch (b) angles are represented in Fig. 5.11. Mean yaw angles for both planes were 39 and 41.3 degrees, while mean pitch angles were about 3 degrees in both planes. Although angle variations were small, limited to 1.5 degrees, some tendencies were identified in the radial distributions. At *plane 3*, both yaw and pitch angles presented a 1.4 decrease in radial direction up to about 18 mm from the wall. A decrease of pitch angle indicates the radial velocity component closer to zero far from the splitter. At *plane 4*, a 1 degree decrease in radial direction in the yaw angle was observed over the splitter (8-9 mm) associated with the velocity increase across the boundary layer. Homogeneity in circumferential direction was ensured for both angles within 0.5 degrees for the 80% and 40% of the circumferential span in *planes 3* and *4* respectively.

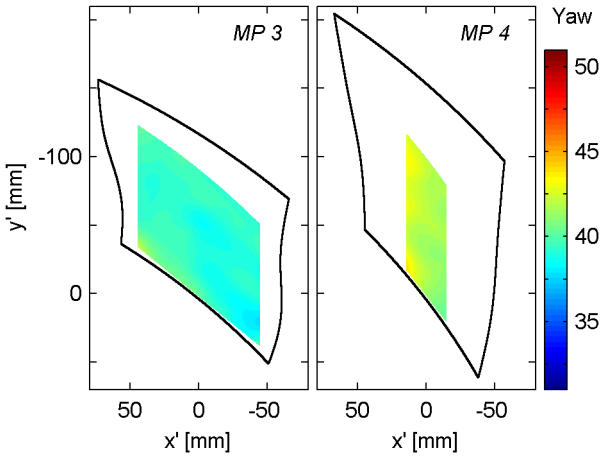

(a)

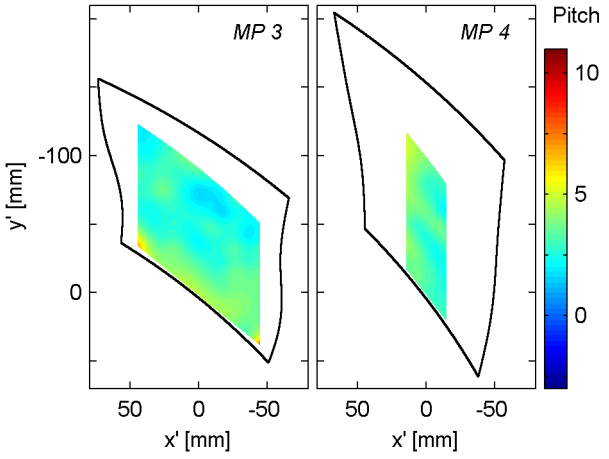

(b)

Figure 5.11: *Contours of yaw (a) and pitch (b) angles at planes 3 and 4.*

5.1.3.3 Temperature and turbulence intensity along the test section.

Total temperature contours in *planes 2* to *4* exhibited a rather uniform distribution, with a maximum variation of about 0.3% (0.9 K)

Turbulence intensity contours measured at *planes 3* and *4* are represented in Fig.5.12. Mean values far from the test section walls are 1.2% at *plane 3*, and slightly decrease to about 1% in the central region at *plane 4*. Ignoring the regions close to the lateral walls, the turbulence intensity level was only seen to increase close to the splitter *at plane 4* to values of about 4-5%. In

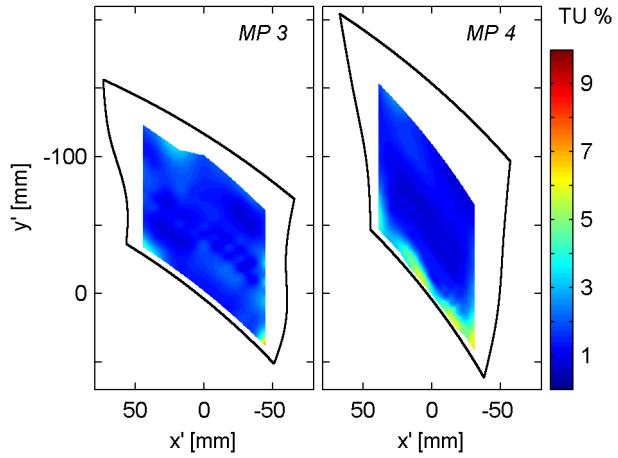

Figure 5.12: *Contours of Turbulence Intensity at planes 3 and 4.*

agreement with the five-hole probe measurements, no boundary layer effects were observed close to the splitter at *plane 3*.

5.2 Aerothermal heat exchangers performances

Results on the thermal and aerodynamic behavior of the type of heat exchangers under investigation are presented in this section. The thermal investigation was focused in the test configuration *continuous fins II*. Results are presented in terms of convective heat transfer characteristics. The aerodynamic analysis is divided in three blocks. First, comparison of flow development along the test section for the different test configurations is addressed. The analysis is restricted in the second block to the wakes of the heat exchangers. Finally, total pressure balances with respect to the inlet and between measurement planes bounding the heat exchangers are analyzed. Results are mainly focused in the two test configurations causing the minimum and maximum flow perturbations: *continuous fins I* and *interrupted fins*. Nevertheless the flow effects induced by the configuration *continuous fins II* are also discussed.

5.2.1 Heat exchanger thermal characterization

The target of the thermal experiments was the measurement of the temporal evolution of the surface temperature distributions of the central fin of the array. To maximize the heat flux flow/heat exchanger, the heat exchanger was initially heated up to 318 K. The surface temperature evolution was the input to the IHCM described in section 4.1.3. Fig.5.13 illustrates the

evolution of the temperatures on the lateral surface of the central fin for three different instants during the cooling down. The inverse solver was fed with the initial conditions (first guess of $Q_0(x, y, t)$) and temperature evolutions ($Y(x, y, t)$) of the visible part of the fin and base surfaces. The transient three dimensional inverse computations were performed for a time step of 0.05 sec. on a domain containing 9450 tetrahedral elements. The iterative process was stopped after n_f =29 iterations. The quality of the minimization process is represented in Fig.5.14 in terms of the comparison, for two different locations, between the measured temperature (Y) and the estimated one (T) computed from the estimated heat flux, output of the IHCM ($Q(x, y, t)$).

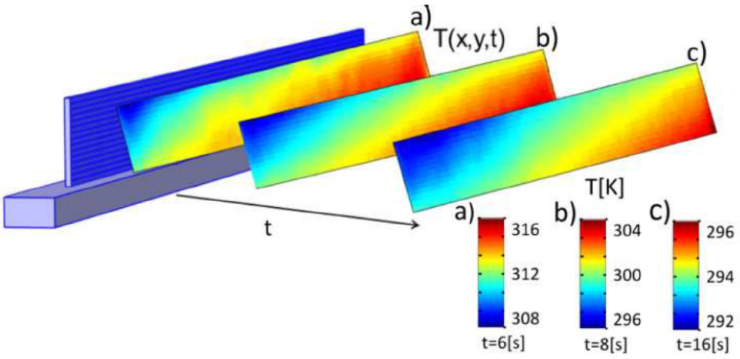

Figure 5.13: *Measured surface temperature evolutions during the test (Y(x,y,t)).*

The adiabatic heat transfer coefficient and adiabatic temperature distributions were obtained through the convective heat transfer approach described in section 4.1.1. The results obtained in the lateral visible part of the fin are represented in Fig.5.15. The adiabatic heat transfer coefficient decreases along the fin in the stream wise direction, and increases along the fin height. Maximum values are observed at the leading edge of the fin. The adiabatic wall temperature also decreases in the longitudinal direction, depicting a maximum variation of 4 K, while it remains almost constant along the fin height.

The evolutions of the adiabatic heat transfer coefficient along the fin length at three different constant heights (2, 6, and 14 mm from the bottom) are represented in Fig.5.16. At each fin height the heat transfer evolution could be compared to that of a flat plate neglecting the influence of the vertical gradients. Correlations from the literature agree on a Nusselt number dependance with the Reynolds number of the form $Nu_x \sim Re_x^{4/5}$ for forced convection on turbulent boundary layers over a flat plate, which in terms of the local convection coefficient turns into the relation $h \sim x^{-1/5}$.

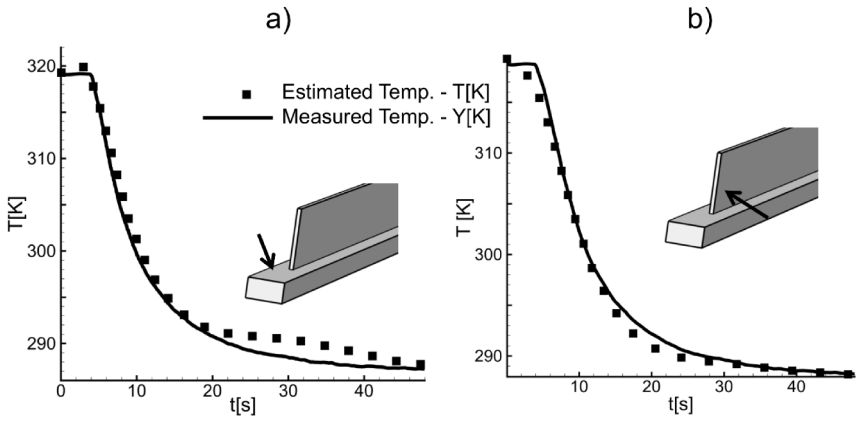

Figure 5.14: *Comparison between measured (Y) and estimated (T) surface temperature evolutions at two locations within the base surface (a), and at the lateral surface (b).*

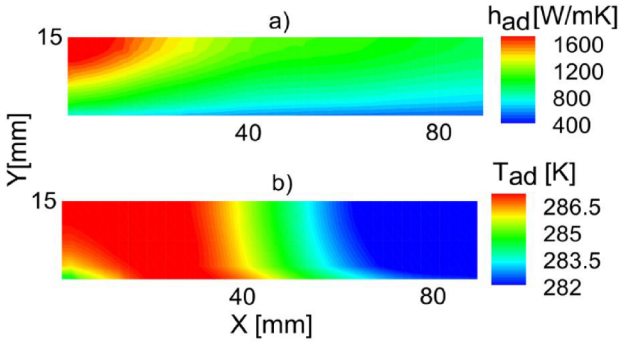

Figure 5.15: *Distributions of adiabatic heat transfer coefficient $h_{ad}(x, y)$ (a), and adiabatic wall temperature $T_{ad}(x, y)$ (b) on the visible part of the fin lateral surface.*

Based on this dependence, the computed adiabatic heat transfer evolutions were interpolated with an exponential fitting ($h_{ad} = a \cdot x^b$). The fittings extrapolated to the full length of the fin are represented together with the experimental data in Fig.5.16. The exponent of the fittings increases with the fin height from -0.13 to -0.19. The adiabatic heat transfer coefficient distribution on the lateral fin surface is dictated by the 3D flow structure. The flow developing along the inter-fins channel and merging with the lateral boundary layers is responsible of the vertical h_{ad} gradients and their variation along the fin. The lower convective coefficients at the leading edge

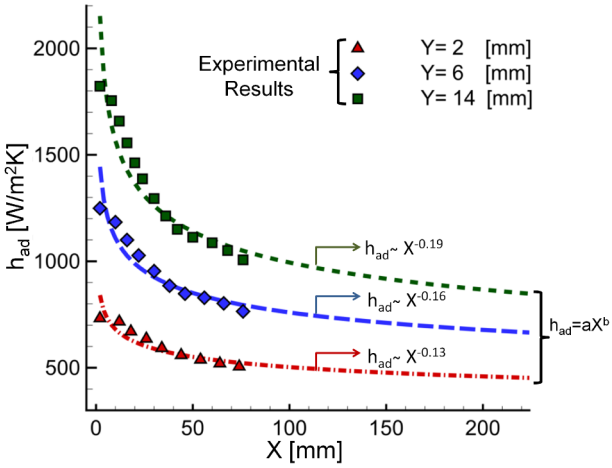

Figure 5.16: *Longitudinal adiabatic heat transfer coefficient evolution at three fin heights, computed data and exponential fitting.*

close to the base can be explained by the effects of the turbulent boundary layer developing over the splitter. The higher flow velocities towards the fin tip promote the increase of the heat transfer coefficient. Secondary flows developing from the entrance of the fins play a dominant role on the pattern of the convective heat transfer distribution.

5.2.2 Flow development along the test section in the presence of heat exchangers

Comparative analyses of the local flow modifications caused by the heat exchangers are presented for the test configurations: *continuous fins I* and *interrupted fins*. The analysis focused on the flow modifications caused by the heat exchangers, only the central region of the 2D contours was considered.

5.2.2.1 Flow evolution over the splitter

Isentropic Mach number distributions computed from the test averaged local static to inlet total pressure ratios are represented in Fig.5.17 in axial coordinates. The uncertainty band computed based on the repeatability for each individual sensor increases with the flow velocity. Besides the differences on M_{is} levels, the parallelism between distributions upstream the location of the arrays of fins proves that their presence does not alter the upstream static pressure distributions. The M_{is} is increased downstream of the fins with respect to its upstream value. The relative increase is larger for the *interrupted fins* than for the *continuous fins I*, resulting in similar

downstream M_{is} level in both configurations. This is in agreement with the mean absolute Mach number evolutions compared in section 5.1.1.2. Distributions downstream of the *clean* and *continuous fins I* configurations follow a similar trend different to that of the *interrupted fins*, as consequence of the strong mixing effects detected in the fins' wakes of the latest.

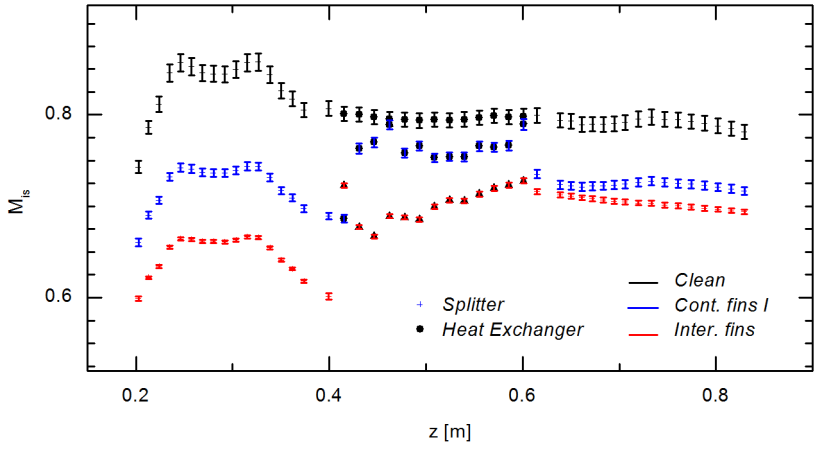

Figure 5.17: *Isentropic Mach number along the test section mid-line.*

The flow within the central passage of the fins presents a different pattern for both configurations, although a strong initial acceleration and a diffusion at the exit is common to both cases. The inter-fins flow structure can not be drawn solely from the static pressure distributions, but some flow characteristics can be pointed out in combination with surface flow visualizations. The flow entering the fins region with a certain angle of incidence with respect to the fins (different for each configuration) is characterized by high velocities, positive longitudinal pressure gradients and turbulent boundary layers. In the *continuous fins I*, the static pressure is not modified close downstream of the leading edges within the beveled fins. After an initial flow acceleration up to about the 27% of the fins length, and a slight pressure recovery, two regions of constant pressure are observed that could reveal flow separation: between 51 and 66% of the fin's length, and at a higher M_{is} level between the 74 and the 89%. In the exit region the flow is again accelerated towards its maximum M_{is} prior to its expansion at the outlet with a pressure recovery of 6.5%. The flow within the *interrupted fins* presents a stronger flow acceleration at the entrance, followed by an also stronger pressure recovery. A region of constant static pressure is observed between the 27 and the 43% of the heat exchanger total length, followed by a continuous M_{is} increase up to the exit. The exit pressure recovery is 4.6 times lower than in the previous case, which is in agreement with a high turbulence mixing region as observed both in the downstream

flow measurements and in the splitter oil visualizations.

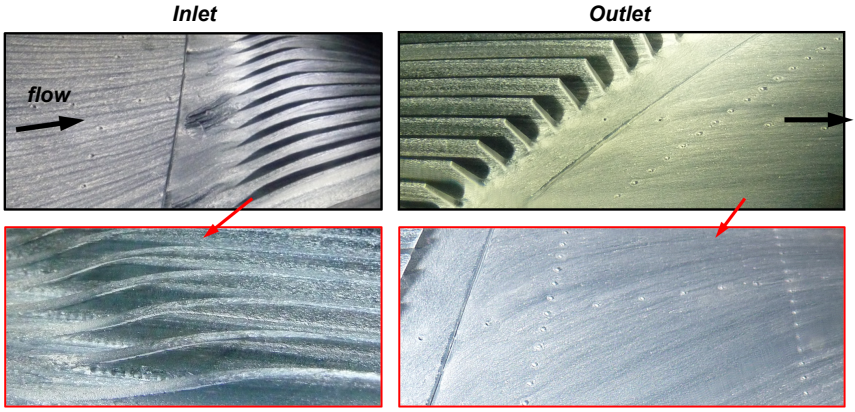

Figure 5.18: *Oil flow visualizations, 'continuous fins I' configuration. Left: streamlines upstream fins leading edges (up), lateral view in the leading edge region (down). Right: streamlines in fins trailing edge region (up), downstream flow evolution over splitter (down).*

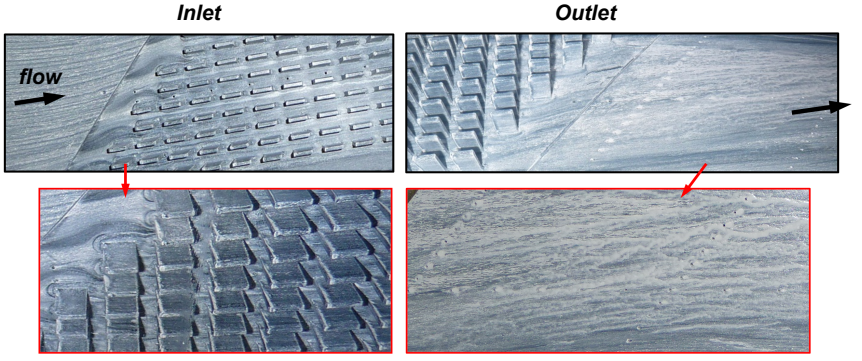

Figure 5.19: *Oil flow visualizations, 'interrupted fins' configuration. Left: streamlines upstream fins leading edges (up), flow redistribution at heat exchanger entrance and fins' lateral view (down). Right: streamlines in fins trailing edge region (up), downstream flow evolution over splitter (down).*

Figure 5.18 shows the streamlines at the inlet and outlet regions of both arrays. The flow is smoothly directed at the inlet within the *continuous fins I* configuration. Along the lateral surface of the fins the streamtrances evolve parallel to the splitter. Individual recirculation spots are identified at the trailing edges of the fins which do not appear to merge between consecutive fins. Figure 5.19 shows images of flow oil visualizations at the entrance and

exit regions of the interrupted array of fins. Due to the position of the leading edges in the array of interrupted fins, streamlines are grouped at the entrance around each two parallel fins. The flow stagnates at the flat leading edge of each fin and a small region of separated flow is observed at the trailing edge of each fin over the splitter surface. Flow separation and reattachment is observed at the lateral surfaces of the fins. At the exit of the array regions of recirculation are observed at the trailing edges. Oil traces downstream along the splitter depict a highly turbulent flow character not observed downstream of the *continuous fins*.

5.2.2.2 Flow modifications upstream of the heat exchangers

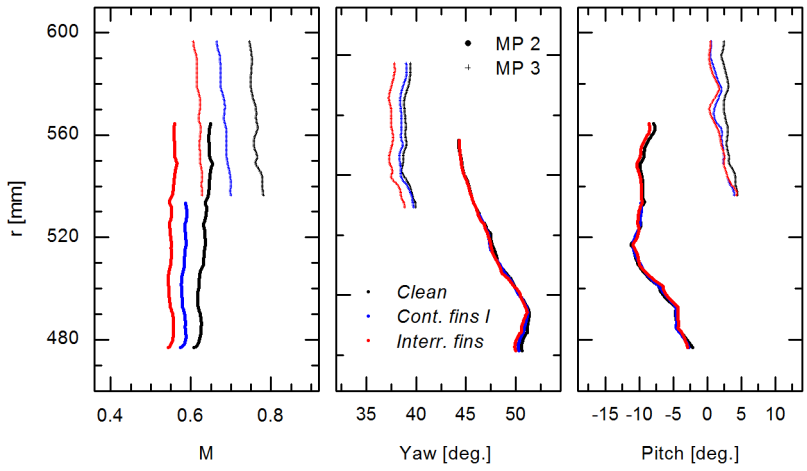

Figure 5.20: *Radial distributions of Mach number, yaw and pitch angles at planes 2 and 3.*

Radial distributions of Mach number and flow angles at *planes 2* and *3* are represented in Fig.5.20. Distributions of total pressure, temperature and turbulence intensity were seen to be identical in the presence or absence of heat exchangers.

Mean Mach numbers at *plane 2* are 0.64, 0.59 and 0.55 for *clean*, *continuous fins I* and *interrupted fins* configurations respectively. A small difference is observed on the magnitude of the radial Mach number gradients in the part of the flow facing the main stream over the splitter. It is in agreement with the mass flow redistribution main channel/inner duct caused by the presence of the arrays discussed in section 5.1.1.2. Due to the proximity of *plane 2* to the IGV, angle distributions at *plane 2* are identical for the different configurations besides the velocity change.

At *plane 3*, Mach numbers present parallel radial distributions with mean

values: 0.76, 0.69 and 0.62 for *clean*, *continuous fins I* and *interrupted fins* configurations respectively. Differences between the yaw angle radial distributions at *plane 3* can not be directly associated to upstream heat exchanger effects, given the differences on flow velocities. However, pitch radial distributions in the presence of fins present a higher negative gradient with respect to the *clean* configuration, indicating a flow deviation towards the over fins region. From a common pitch value of 4.3 degrees in the vicinity of the splitter, pitch angles are 1.5 degree lower far from the splitter in the presence of fins.

5.2.2.3 Flow modifications downstream of the heat exchangers

Comparisons of radial distributions of Mach number, flow angles and turbulence intensity at *plane 4* are represented in Fig.5.21. Only the inner 40% of the radial span has been represented in light of the flow homogeneity for higher radial positions.

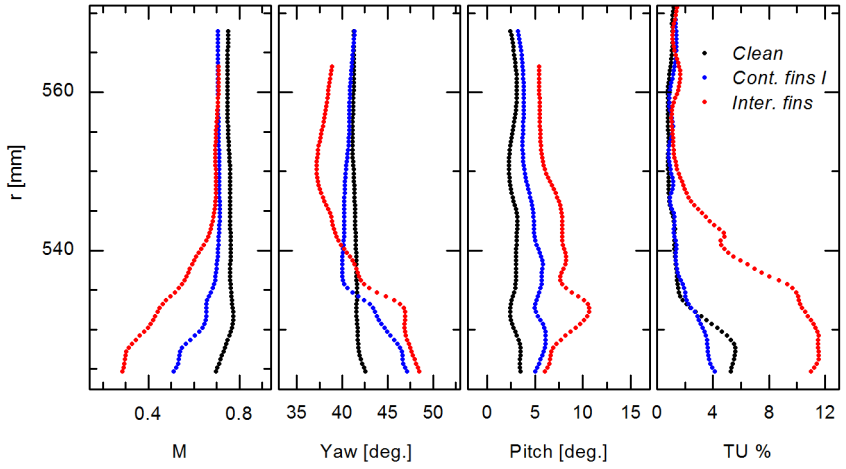

Figure 5.21: *Radial distributions of Mach number, yaw and pitch angles, and turbulence intensity at plane 4.*

Mean flow Mach numbers over the fins are only about 6% lower than in the absence of fins. Close to the splitter Mach numbers are reduced within the boundary layer in the absence of fins, and in a higher extent within the heat exchangers wakes. Mach number deficits close to the splitter with respect to the mean value over the fins are about 8%, 28% and 59% for *clean*, *continuous fins I* and *interrupted fins* configurations respectively. The radial position from the splitter at which the 99% of the unperturbed Mach number is attained is 15 mm for the *continuous fins I* configuration, and at 23 mm in the case of the *interrupted fins*, with fins heights of 15 and

17.5 mm respectively. Additionally, Mach number contours at *plane 4* are represented in Fig.5.22. Periodic variations in circumferential direction are observed in the *continuous fins I* configuration, with a spatial periodicity corresponding to the fins' pitch. On the contrary, the wakes of the individual rows of staggered rectangular fins can not be identified.

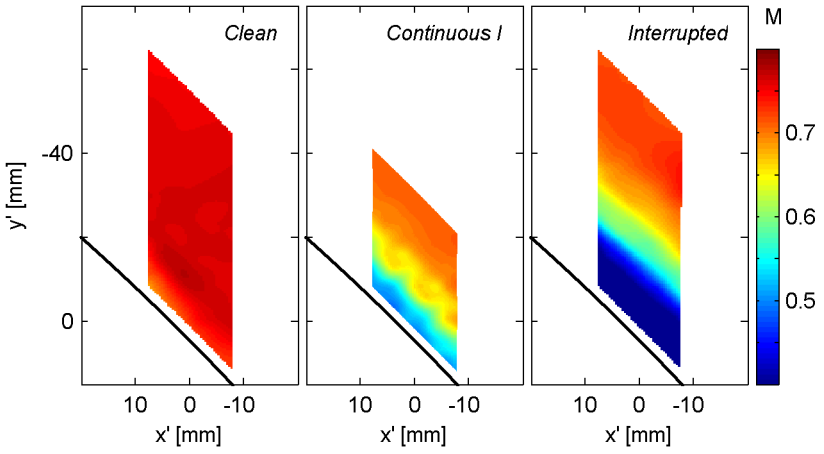

Figure 5.22: *Mach number contours at plane 4.*

The effects of the fins on the flow direction are depicted in the radial distributions in Fig.5.21, as well as in the contours plotted in Fig.5.23 (yaw angle) and Fig.5.24 (pitch angle). In the absence of fins, maximum angle variations of 1 degree are observed within the radial span, with mean values of 41.3 and 2.9 degrees for yaw and pitch angles. For the three configurations maximum yaw angles are observed in the vicinity to the splitter, with higher values downstream of the fins. Yaw angles decrease in radial direction through the wakes of the fins to values slightly lower than the mean yaw angle in the flow over the fins, to which they evolve for higher radial positions. Pitch values are higher in the presence of the fins and reach their maximum values in the region of the wakes, indicating that the flow is deviated towards the splitter.

In the *continuous fins I* configuration the yaw angle, 4.5 degrees higher close to the splitter than in the *clean* configuration, experiences a 7 degrees decrease in radial direction up to 15 mm, followed by a slight increase (1 degree) while accommodating to a constant yaw value similar to the clean bypass flow. Pitch values are 3.5 degrees higher than in the absence of fins within the wakes, and decrease to similar values than in clean flow for higher radius. The wakes of the individual fins are distinguished in the 2D contours both in the yaw and pitch angle distributions.

Variations are higher in the *interrupted fins* configuration. In the vicinity to the splitter the yaw angle is 1.5 degrees higher than in the *continuous*

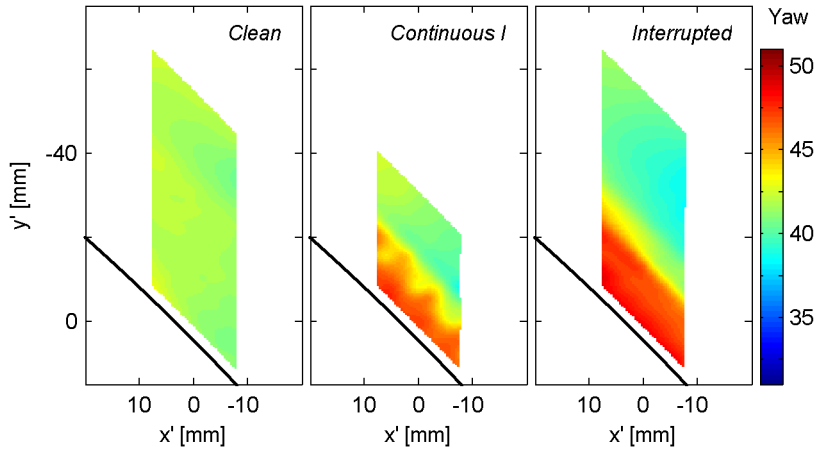

Figure 5.23: *Yaw angle contours at plane 4.*

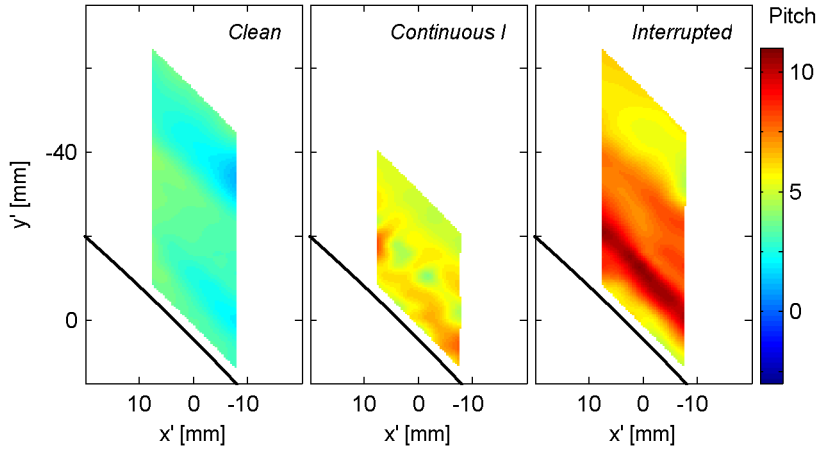

Figure 5.24: *Pitch angle contours at plane 4.*

fins I configuration, in agreement with the difference between both fins' orientation, and pitch angles are 2.5 degrees larger. Up to 10 mm from the splitter, the yaw gradient is small (1.5 degrees) while pitch angles present a 4.5 increase. From 10 to about 27 mm from the splitter yaw and pitch values present the largest decrease, 9.5 and 5 degrees decrease respectively, and for higher positions the influence of the wakes slowly vanishes and the flow angles tend to their constant value far from the walls. The 2D contours downstream of the interrupted fins (Figs.5.23,5.24) reflect homogeneous distributions in circumferential direction.

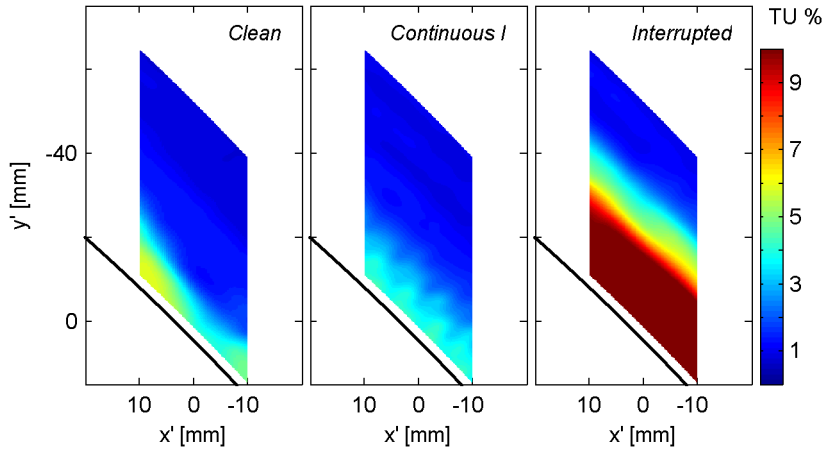

Figure 5.25: *Turbulence intensity contours at plane 4.*

The heat exchanger effects on the flow turbulence intensity are depicted in terms of averaged radial distributions in Fig.5.21, and in terms of 2D contours in Fig.5.25. The turbulence intensity downstream of the *continuous fins I* configuration, differs from the *clean* configuration exclusively in the region close to the splitter, up to about 10 mm. In this region, maximum turbulence intensity values are 5.5%, and variations are observed across the fins in circumferential direction. It is not the case in the *interrupted fins* configuration presenting values close to the splitter are as high as 11-11.5%. The gradient in radial direction is lower in the first 10 mm, and between 10 and 28 mm from the splitter the turbulence intensity decreases from 10 % to the free flow value, 1.1%. Those two regions of different radial gradients were also observed on the flow angles distributions. As for the velocity and flow angles, the turbulence intensity is homogeneous in circumferential direction.

Ratios of total temperature at *plane 4* are represented in Fig.5.26. Total temperature ratios are uniform within 0.15% (about 0.3 K) in the *clean* configuration as well as far from the splitter in the presence of heat exchangers. However, total temperature variations are observed within the fins' wakes. Periodic variations are observed in circumferential direction in the *continuous fins I* configuration up to about 11 mm in radial direction from the splitter. Five valleys are identified within the circumferential span covering partially five fins and corresponding passages. Downstream of the *interrupted fins* configuration both the temperature ratio decrease and the flow area affected are higher than in the *continuous fins I* configuration, while distributions are homogeneous in circumferential direction. In agreement with the rest of flow magnitudes analyzed, lowest temperature ratios are observed up to about 10 mm in radial direction which corresponds to total temperatures 1.6 K lower than the free flow reference temperature. From

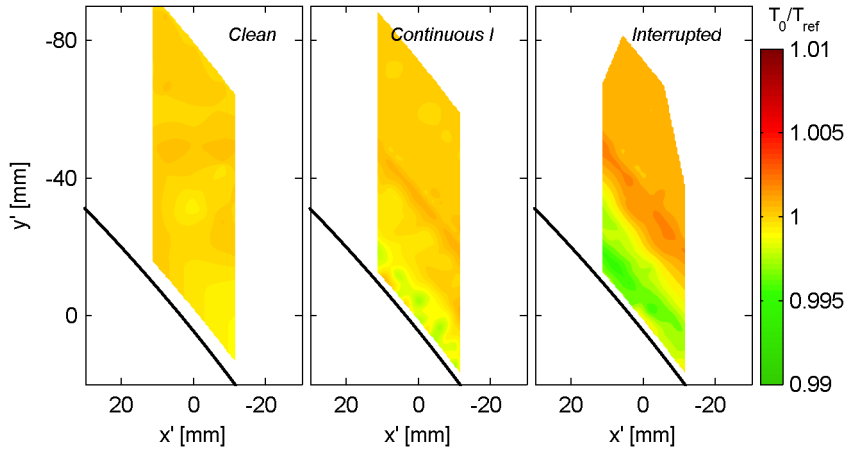

Figure 5.26: *Temperature ratio contours at plane 4.*

10 to about 27 mm in radial direction the temperature increases to values slightly over the reference (0.2 K higher), to later decrease again to the free flow temperature.

5.2.3 Heat exchangers wake analysis

Measurements at *planes 4* and *5* capture the transversal pattern of the time averaged flow characteristics downstream of the finned arrays. The magnitude and depth in radial direction of the flow perturbations caused by the heat exchangers was addressed in the analysis of the radial distributions at *plane 4*. The magnitude of the variations in circumferential direction, as well as the wakes dissipation in the direction of the flow, are analyzed in this section from high spatial resolution measurements (1-2 mm in the local x' direction).

5.2.3.1 Continuous fins

Flow orientation, continuous fins I

Circumferential yaw and pitch angle distributions are represented in Fig.5.27 at the radial position at which the maximum amplitude variations were observed. Three fin wakes were covered resulting in three pitch and yaw angle periodic variations. Yaw variations presented a maximum amplitude of about 2.9 degrees at 8-9 mm radial height. The amplitude diminished for higher radial positions as the radial gradient decreased. Pitch angles presented a maximum peak to peak variation of 2 degrees at a slightly higher radial position, 11 mm. The maximum amplitude of the Mach number

circumferential variation was about 0.045. Both total and static pressure circumferential variations were also observed, the relative fluctuation of the static pressure being lower than the correspondent to the total pressure (1.3 % and 4.6% respectively). Given the scarce resolution of the five-hole probe measurements in circumferential direction (points evenly spaced 2 mm in the local x' direction), the presented peak to peak variations could be underestimated.

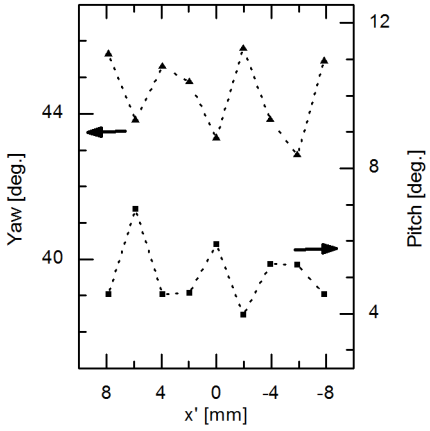

Figure 5.27: *Circumferential distributions of yaw and pitch angle at 8 and 11 mm radial height respectively at plane 4, 'continuous fins I' configuration..*

Flow velocity, continuous fins I

Contours of Mach number derived from Pitot and wall pressure measurements at *planes 4* and *5* are represented in Fig. 5.28a. Correspondent circumferential distributions at selected radial positions are depicted in Fig.5.28b. The sketch (left) shows the location of the measurement points correspondent to the circumferential distributions, as well as the projection in the axial direction of the fins trailing edges onto *plane 4*. Peak to peak variations at *plane 4* are low over the splitter surface (0.018, about 3.8 %). The amplitude of the fluctuations increases in radial direction reaching a maximum of 0.05 (8.4 %) at 9 mm radial height. Comparison at this position of the total pressure variations from Pitot and five-hole probe measurements yielded the same result. The wake width is about 9.5 mm at *plane 4* at the position of the maximum fluctuation. Projected in a plane perpendicular to the mean flow direction it is equivalent to the fins pitch, about 3.9 times the mean fin thickness. The amplitude of the circumferential variations, decreases rapidly for higher radial positions.

The flow pattern downstream of the fins is diffused as the flow evolves

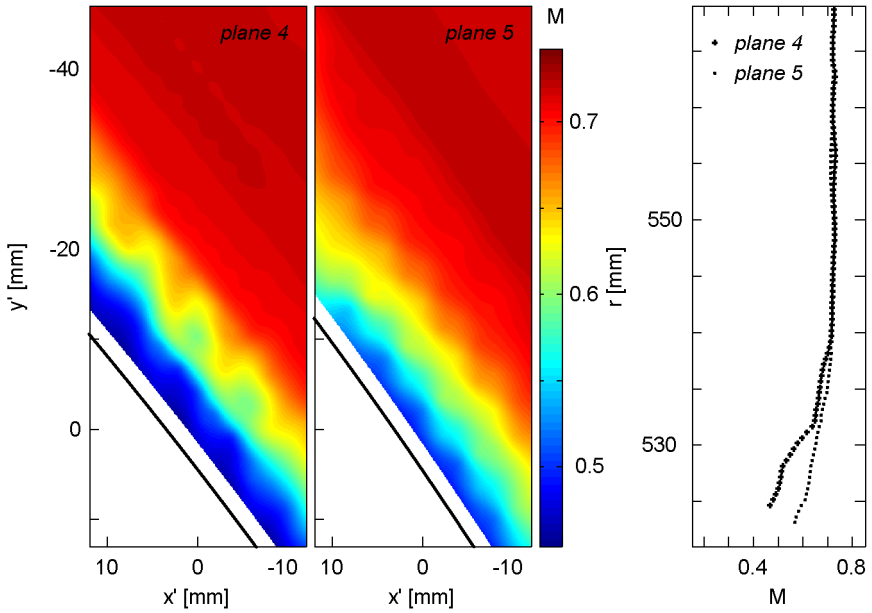

(a) *Mach number contours at planes 4 and 5, 'continuous fins I' configuration.*

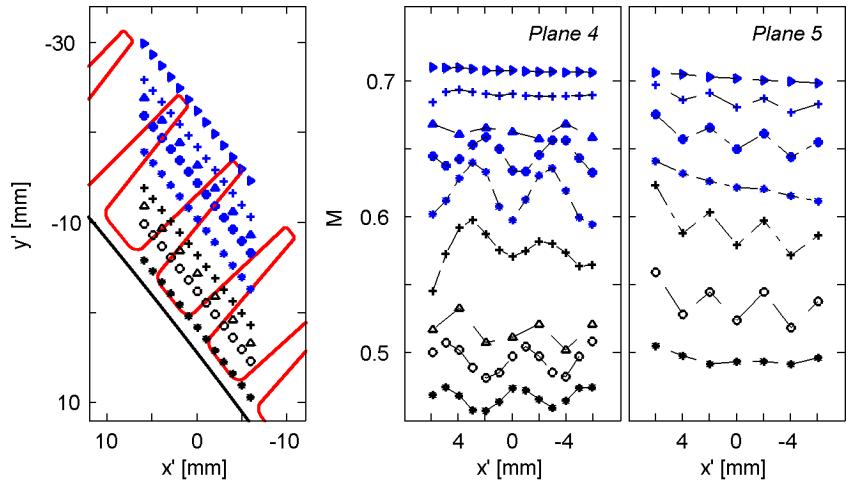

(b) *Circumferential Mach number distributions at planes 4 and 5, 'continuous fins I' configuration.*

Figure 5.28: *Mach number distributions downstream of 'continuous fins I' configuration.*

from *plane 4* to *5*. Nevertheless, peak to peak values of about 0.03 (5.7 %) are still identified at *plane 5*. Maximum variations are observed at lower radial positions and radial gradients are decreased as depicted in the radial distributions in Fig.5.28a (right).

Flow turbulence intensity, continuous fins I

Contours of turbulence intensity at *planes 4* and *5* are represented in Fig.5.29a together with the correspondent radial distributions along 40 mm over the splitter. Circumferential distributions at different radial positions evenly spaced each 4 mm in y' direction are represented in Fig.5.29b.

The turbulence intensity remains the same at both planes and also the radial evolution. However, while at *plane 4* fluctuations are observed with maximum peak to peak values of 1.1 units around a mean value of 3.1% (37% variation), circumferential variations are not perceptible any more at *plane 5*. Peak to peak variations at *plane 4* decrease in radial direction, being negligible at radial positions higher than 11 mm. Absolute variations are similar in the first 10 mm, although maximum values are measured at about 7-8 mm radial height.

Comparison continuous fins I/II

Flow effects caused by the two different arrays of continuous fins tested were similar in magnitude in comparison with the perturbations introduced by the array of interrupted fins. Differences were observed within the first 12 mm in radial direction from the splitter, the radial span reached by the perturbations been similar in both cases. Mach number and turbulence intensity contours at *plane 4* are represented in Fig.5.30. In the *continuous fins II* configuration, circumferential wake profiles are not appreciated as in the *continuous fins I* configuration. The mixing effects at the exit of the fins are stronger, as it is also evidenced by the contours of turbulence intensity. Nevertheless the main differences do not concern the flow magnitudes but the pattern of the wakes.

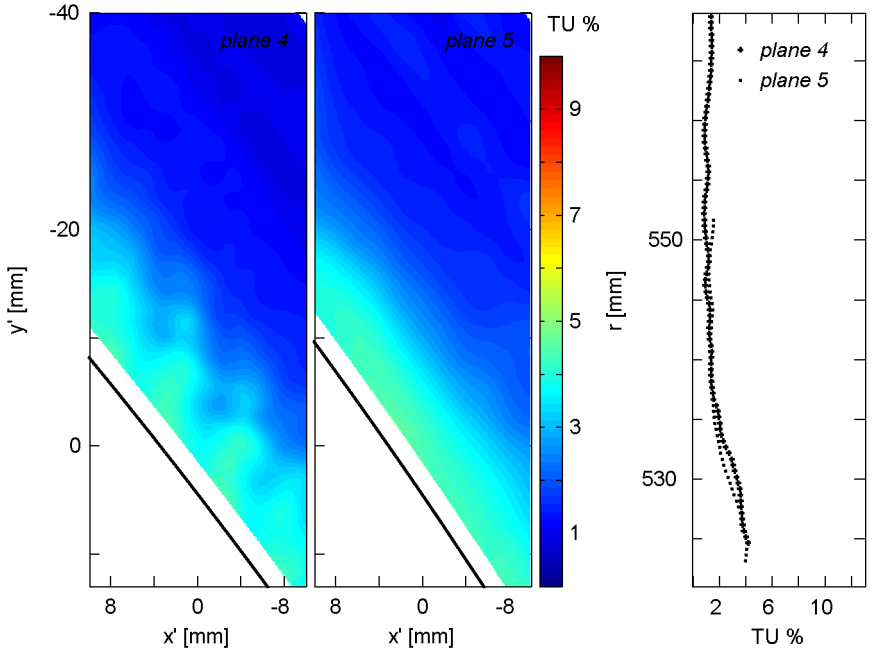

(a) *Turbulence intensity contours at planes 4 and 5, 'continuous fins I' configuration.*

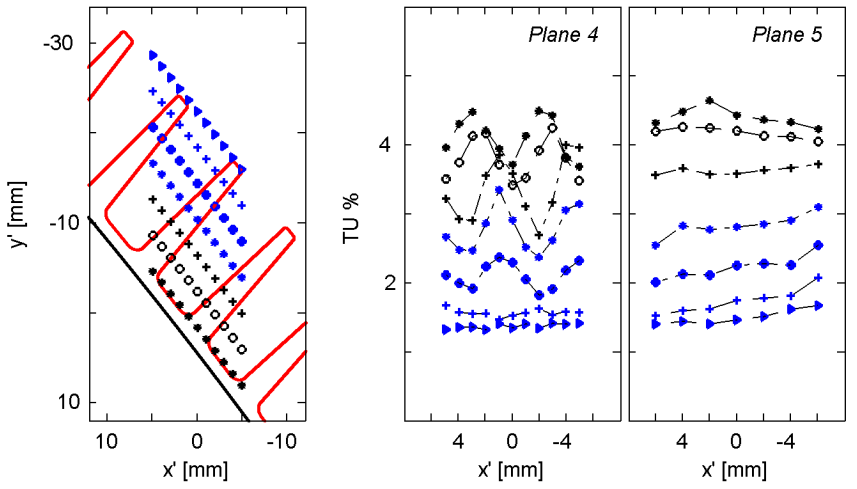

(b) *Circumferential distributions of turbulence intensity at planes 4 and 5, 'continuous fins I' configuration.*

Figure 5.29: *Turbulence intensity distributions downstream of 'continuous fins I' configuration.*

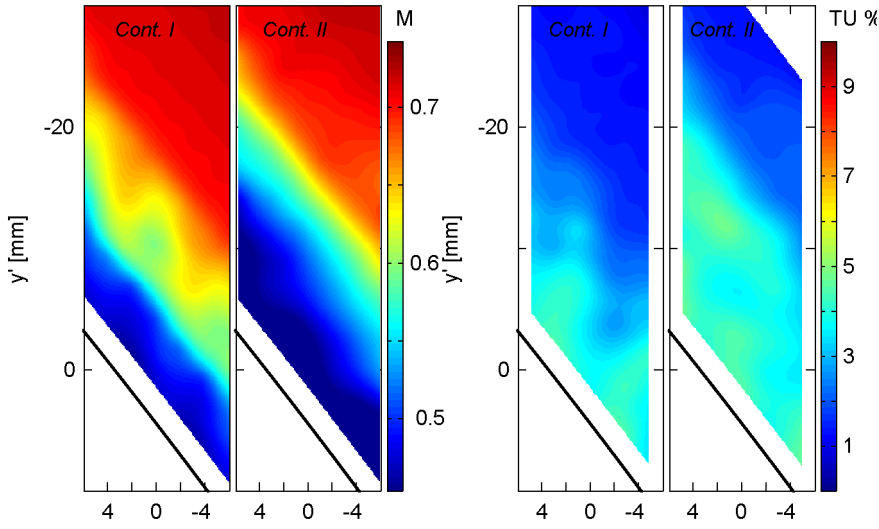

Figure 5.30: *Comparison of Mach number and turbulence intensity contours downstream of configurations 'continuous fins I' and 'continuous fins II', plane 4.*

5.2.3.2 Interrupted fins

Flow orientation and velocity

The flow direction and velocity were seen to be almost constant in circumferential direction. Distributions of yaw and pitch angles at the radial positions at which the maximum variations were observed for the *continuous fins I* (8 and 9 mm respectively), provided values of 46.8 and 10.3 degrees, uniform within ± 0.27 and ± 0.18 degrees respectively.

Contours of Mach number at *planes 4* and *5* derived from Pitot and wall pressure measurements are represented in Fig.5.31a. Circumferential distributions at several radial positions are shown in Fig.5.31b. The associated measurement locations of the circumferential distributions represented, and the transversal cut of the fins by a plane parallel to the measurement plane, are indicated in the same figure.

The abrupt flow deceleration at *plane 4* close to the splitter is recovered as the flow evolves from *plane 4* to *plane 5*. Averaged radial distributions at both planes converge to the same values from about 18 mm radial height from the splitter. For lower positions, the radial gradient is lower at *plane 5*. At the closest circumferential traverse to the splitter, a small peak can be identified which could be associated to a fin wake. It is not present for higher positions where the flow mixing effects are higher.

Flow turbulence intensity

Contours of turbulence intensity, averaged radial distributions, and circumferential distributions at *planes 4* and *5* are represented in Fig.5.32.

While the maximum values of TU were similar at both planes downstream of the array of continuous fins, in the case of the interrupted fins the maximum turbulence intensity is reduced at *plane 5*. As for the Mach number distribution, the averaged radial distributions of TU converge to the same value from about 18 mm radial height. The highest turbulence intensity at *plane 4* is not observed at the closest circumferential traverse to the splitter, as already observed in the comparison of the radial distributions for the different configurations, but to a traverse at about 6 mm radial height from the splitter. A periodic pattern in circumferential direction can be identified close to the splitter, corresponding to the velocity peak observed from the Pitot measurements.

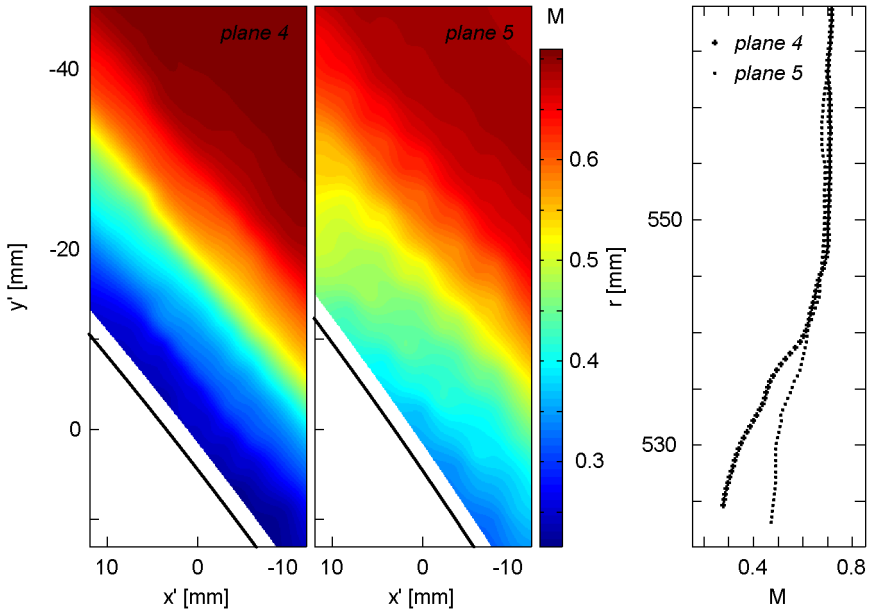

(a) *Mach number contours at planes 4 and 5, 'interrupted fins' configuration.*

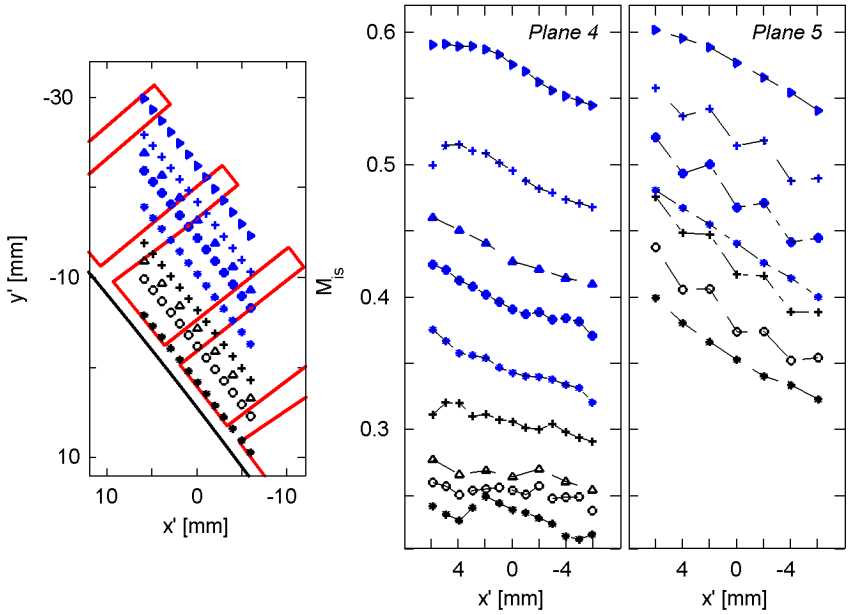

(b) *Circumferential Mach number distributions at planes 4 and 5, 'interrupted fins' configuration.*

Figure 5.31: *Mach number distributions downstream of 'interrupted fins' configuration.*

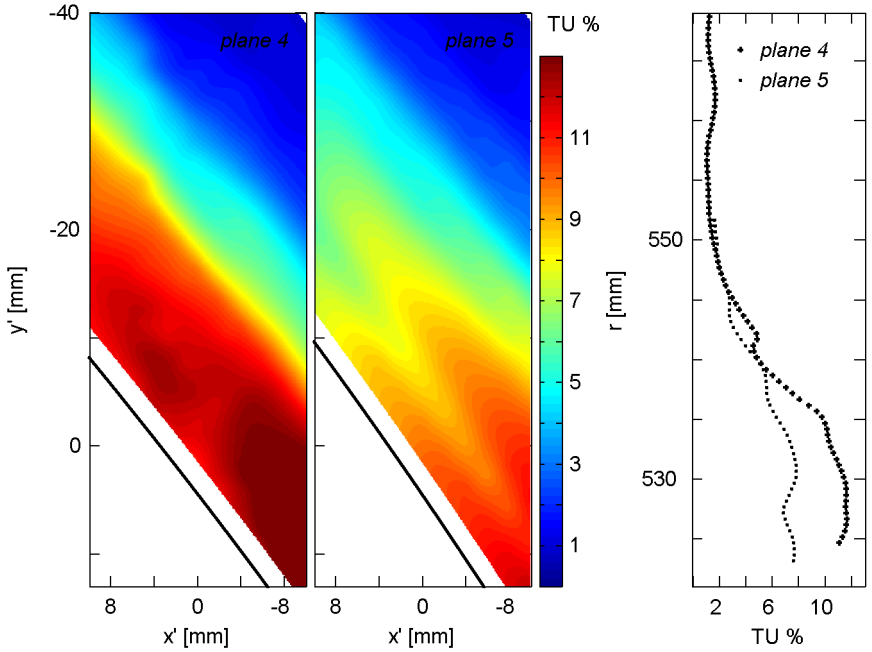

(a) *Turbulence intensity contours at planes 4 and 5, 'interrupted fins' configuration.*

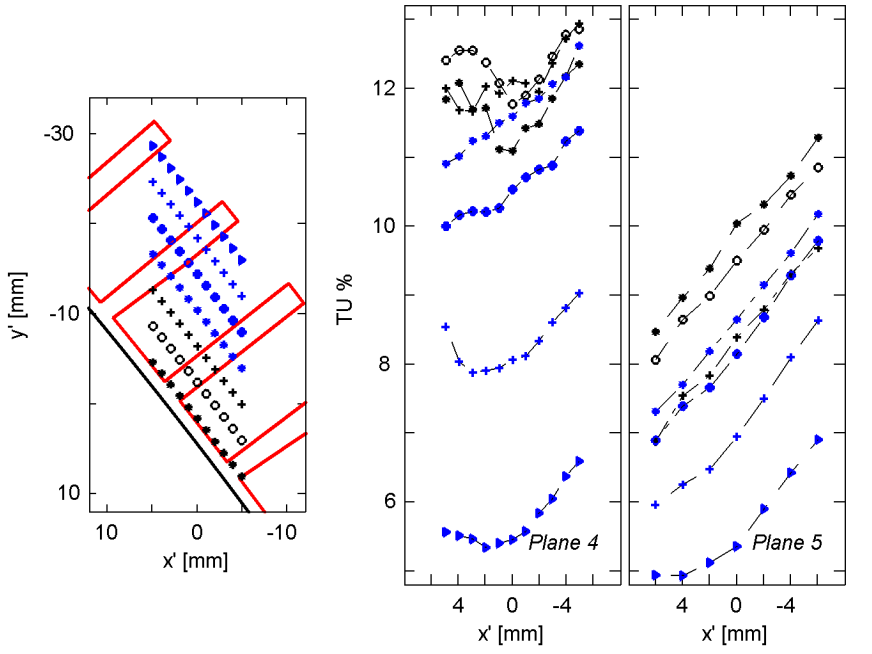

(b) *Circumferential distributions of turbulence intensity at planes 4 and 5, 'interrupted fins' configuration.*

Figure 5.32: *Turbulence intensity distributions downstream of 'interrupted fins' configuration.*

5.2.3.3 Flow temperature variations

The temperature field was investigated in order to identify perturbations on the thermal field caused by the fins, inherent to the turbulent compressible nature of the transonic bypass flow. Periodic variations in circumferential direction were observed downstream of the *continuous fins I* configuration. Downstream of the *interrupted fins* the magnitude and extent of the temperature modifications were larger, although periodic circumferential variations were not appreciated.

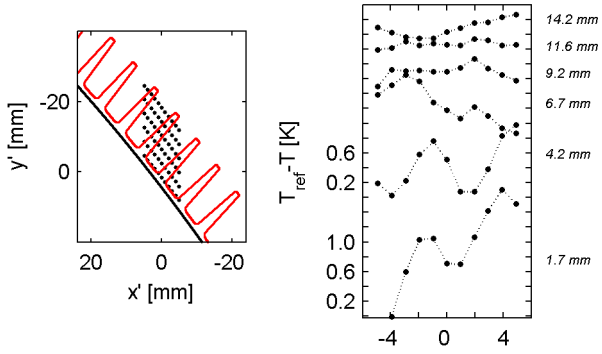

Figure 5.33: *High spatial resolution temperature measurements downstream of continuous fins at plane 4. Left: Measurement points and fins TE projection on* plane 4. *Right: Temperature deviations across fins wakes at different radial positions.*

Higher spatial resolution temperature measurements (evenly spaced each 1 mm in the local x' direction) were performed downstream of the *continuous fins I* at *plane 4*, in order to evaluate the amplitude of the circumferential variations and to analyze the nature of the temperature modifications. Total temperature deviations at different radial positions are represented in Fig.5.33. The mean component of the temperature differences at the different radial positions (with respect to the reference free flow temperature) has been removed to avoid superposition. The circumferential span covers at least one complete fin's pitch. Peak to peak oscillations of 1K were observed at 1.7 mm from the splitter surface, decreasing to 0.9 K and to about 0.6 K at 4.2 and 6.7 mm respectively in radial direction. At 9.2 mm temperature oscillations were within the same order of magnitude of the uncertainty on the temperature measurements and for higher positions a clear trend could not be further identified.

Total temperature non uniformities across wakes can be associated to different effects: heat exchange between flow and immersed body, mechanical energy dissipation into thermal energy, and unsteady energy redistributions inside vortical structures. The latest two effects are linked to entropy gen-

eration in turbulent mixing regions. Although numerous investigations on wake mixing processes have been reported, few authors have addressed the behavior of the total temperature in those regions. Carscallen et al. [120] first observed unexpected time average total temperature (energy) separation within the wakes downstream of a stator blade row in transonic flow and observed that the exit temperature contour mapped one to one with the total pressure loss coefficients. Recent investigations attempted to correlate the total temperature and loss coefficients to the unsteady entropy production and to analyze their dependence on the vortex shedding from the blades trailing edges [121–126]. Total temperature redistribution was also investigated by Ottolia and Sieverding behind turbine blades [127, 128]. Those studies confirmed the existence of vortex driven energy separation in the wake, resulting in abated total temperatures in the central zone with respect to the upstream total temperature, and discrete hot spots towards the edges of the wake at higher temperature than the incoming flow. This total temperature redistribution referred as the 'Eckert-Weise' effect was first observed downstream of a thermally insulated cylinder.

In order to justify if the temperature variations observed across the wakes of the heat exchangers are caused by energy separation or solid-fluid heat exchange, estimative energy balance calculations were performed. In the referred tests no external heat was provided to the fins, and flow inlet temperatures were about atmospheric conditions. The conductivity of the test section walls is as low as that of thermoplastics (about 0.19 W/mK), and the high conductivity aluminium fins were mounted on a plastic support with intermediate reinforced insulation including an air cavity. Thus, thermal equilibrium between the flow and the fins is assumed to be reached before the probe traverse measurements were initiated, during the setting of the operational conditions. Under those conditions heat transfer effects between fins and flow are believed to be low. Nevertheless heat transfer estimations were performed based on steady one-dimensional energy balances. Calculations made use of heat transfer fins characteristics obtained from the heat exchanger thermal characterization test campaigns.

The calculation was performed considering the energy balance between the inlet and the outlet of a control region comprising one fin pitch. The region analyzed covers one fin and half of the inter-fins channel width at each fin's lateral side, and extends along the fin length and height. The heat flux can be computed directly in terms of mean convective heat transfer, flow driving temperature, and mean fin temperature, Eq.5.1. Adiabatic heat transfer coefficient and adiabatic wall temperature distributions were obtained from the thermal heat exchanger characterization. Wall temperatures were provided by embedded thermocouples.

$$q = h_{aw} \cdot (T_{aw} - T_w) \tag{5.1}$$

The total heat exchange fluid-solid within the channel is determined by the

product of the heat flux and the wet solid area within the passage, $Q_{fin} = q \cdot A_w$. The mean flow temperature deficit can be computed considering the flow through the control region as indicated in Eq.5.2. The mass flow through the control volume and the flow heat capacity (C_p) were computed from pressure and temperature measurements at *plane 3*, at the entrance of the control domain.

$$\Delta T_{mean} = Q_{fin}/(C_p \cdot \dot{m}) \tag{5.2}$$

Estimated mean temperature deficits were about 0.23 ± 0.05 K. Further hypothesis allowed a rough estimation of the maximum temperature decay downstream of a fin caused by the heat exchange flow-fin. For this purpose it was assumed that the pitch-wise temperature profiles can be described by a Gaussian distribution centered at the wake core with an area equal to ΔT_{mean}. Hypothesis regarding the wake width and temperature deficit content on the wake were also required. Pitch-wise temperature profiles were measured at about 24 fin thickness downstream of the fins trailing edge in the flow direction. On the profiles represented in Fig. 5.33 it is not possible to clearly identify plateaus of temperature deviation between consecutive wakes. Thus, the wake width could be considered of the same order of the fin's pitch length. The maximum temperature decay as function of the mean temperature deficit, the temperature deficit content on the wake, and the wake width, is expressed by Eq.5.3. The standard deviation σ is defined by the ratio wake to fin-pitch width, and the coefficient z_1 defined for normal distributions in function of the percentage of temperature deficit contained within the wake. In order to estimate the maximum temperature variation that could be measured across de wakes if it would be caused purely by heat transfer solid-fluid, it is considered that a 99.9 % of the mean temperature deficit is contained in the wake (z_1=3.29).

$$\Delta T_{max} = \frac{\Delta T_{mean}}{\sigma\sqrt{2\pi}}, \qquad with \qquad \sigma = \frac{0.5\frac{wake}{finpitch}}{z_1} \tag{5.3}$$

$\frac{wake}{f.pitch}$ \ $\Delta T_{mean}[K]$	*0.18*	*0.23*	*0.28*
1.2	0.39	0.50	0.61
1.0	0.47	0.60	0.73
0.8	0.59	0.75	0.91

Table 5.2: *Maximum temperature deficit in the core of the wake depending on the wake width and in the mean temperature deficit.*

Maximum temperature deficits for different values of wake to fin's pitch width ratio (1.2, 1, 0.8) are shown in Table.5.2 for the estimated mean temperature deficit (0.23 ± 0.05 K). For a wake equal to the pitch, the maximum

ΔT measured on its center would correspond to 0.6 K. This ΔT_{max} would be lower if the recorded variations were provoked by consecutive fin wakes wider than the inter-fins space mixing at their limits, and higher in the case of thinner wakes (Table.5.2).

Estimated maximum temperature variations dictated solely by heat exchange between the flow and the fins are slightly lower than the temperature deviations measured for the continuous fins configuration. Maximum temperature variations due to solid fluid heat transfer increase if larger mean temperature deficits or narrower thermal wakes are considered. According to those results it could be assumed that both solid-fluid heat transfer and energy redistribution within the turbulent vortical structures might be contributing to the temperature variations measured downstream of the arrays of fins.

The temperature contour at the central region of *plane 4* downstream of the array of interrupted fins did not reflect circumferential periodic variations, but a radial pattern which, although smoother, can also be identified in the *continuous fins I* contour (Fig.5.26). The total temperature is decreased from its value at the closest circumferential traverse to the splitter, presenting a minimum at about 6 mm radial height. Up to about 11 mm the radial gradient of the temperature ratio is small compared with the gradient observed between this position and about 26-27 mm in radial direction from the splitter. At this position the temperature ratio presents a maximum, and the flow temperature is higher than the reference temperature. The radial total temperature evolution presents the same radial trend than the turbulence intensity with the exception of the peak of total temperature at relatively high radial positions. It can be observed that at the radial position of the maximum temperatures, the flow velocity is already similar to the free flow velocity and its radial gradient is very small. Thus, the flow temperature can be considered dominated by the turbulence of the flow, and although solid-fluid heat transfer may contribute to the temperature deficit in the wake, energy redistribution within the turbulent mixing region could explain the obtained temperature results.

5.2.4 Heat exchanger pressure loss evaluation

The evaluation of local flow perturbations in terms of non dimensional pressure losses allowed the direct comparison of the different heat exchanger aerodynamic performances, independently of the overall flow differences. Contours of pressure loss coefficients ($C_{p,i-j}$) were computed for a certain test configuration as total pressure loss balances between different test section positions (planes i, j) made non dimensional by the correspondent local dynamic pressures, Eq.5.4. Cell average interpolation routines were used to compare flow variables between different planes (section 4.2.4). Based on this definition, non dimensional pressure loss coefficients are invariable with the current values of inlet mass flow and Mach number. Because the Re

number varies less than 7% for all conditions, and turbulence and temperature is the same, flow dissipative effects can be considered invariable, and under equal test section geometry and surfaces rugosity, also friction losses are invariable for the current Re number range [129, 130].

$$C_{p,i-j} = \frac{\frac{P_{T,i}}{P_{ref}} - \frac{P_{T,j}}{P_{ref}}}{\frac{\gamma}{2}\frac{P_s}{P_{ref}}M^2} \tag{5.4}$$

Contours of pressure loss coefficients between *planes 1* and *2* ($C_{p,1-2}$), and between *planes 1* and *3* ($C_{p,1-3}$), computed based on the dynamic pressure distribution at *planes 2* and *3* respectively, were identical for the different test configurations. At *plane 2*, maximum pressure loss coefficients far of the inner wall were of 2%, corresponding to 4-5 mbar total pressure decrease from the inlet. Close to the hub values of $C_{p,1-2}$ increased up to 10% due to the secondary flows downstream of the inlet profiles and their interaction with the wall boundary layer. At *plane 3* non dimensional total pressure deficits were about 4% and rather uniform in all the domain far from the lateral walls. No increase of pressure losses was identified in the vicinity of the splitter wall. Since dynamic pressures were higher at *plane 3*, the correspondent total pressure losses were about 10, 7 and 5 mbar for *clean*, *continuous fins I*, and *interrupted fins* configurations.

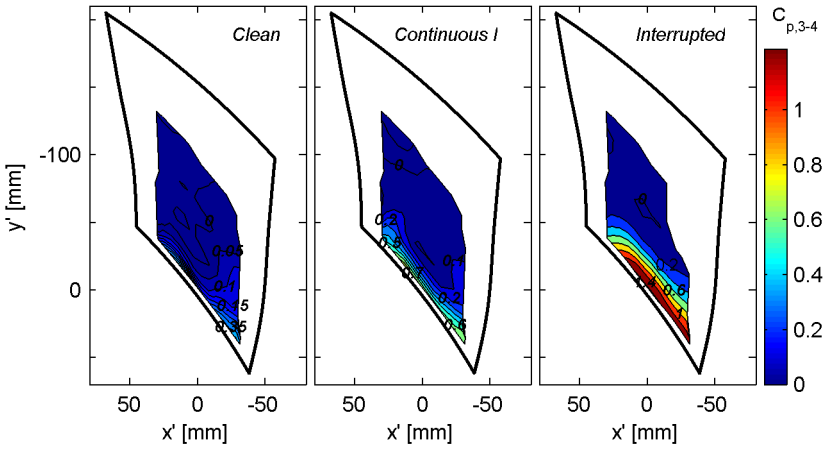

Figure 5.34: *Contours of pressure loss coefficients between planes 3 and 4, relative to the dynamic pressure at plane 3, for test configurations 'clean', 'continuous fins I' and 'interrupted fins'.*

Pressure losses introduced by the heat exchangers were evaluated in terms of non dimensional pressure balances between the two measurement planes bounding the fins ($C_{p,3-4}$), using as reference upstream dynamic pressure

distributions, *plane 3*. Contours are represented in Fig.5.34 for the configurations *clean*, *continuous fins I*, and *interrupted fins*. Pressure losses represented for the complete measurement domain at *plane 4* reflect the effects of the lateral walls and corner vortices at the limits of the domain in the circumferential direction. Far from the splitter, pressure loss coefficients remain uniform within 5% in all the cases. In the absence of fins, the boundary layer developing along the splitter is responsible of maximum pressure loss coefficients of 40%. In the *continuous fins I* configuration, pressure losses reach maximum values about 70% right over the splitter. Flow properties being cell averaged, the spatial resolution within the plots is limited to 5 mm, preventing the identification of the wakes circumferential profiles. Pressure loss coefficients are increased in the *interrupted fins* configuration to maximum values 2 times higher than the maximum of the *continuous fins I*, 1.4 times the upstream dynamic pressure.

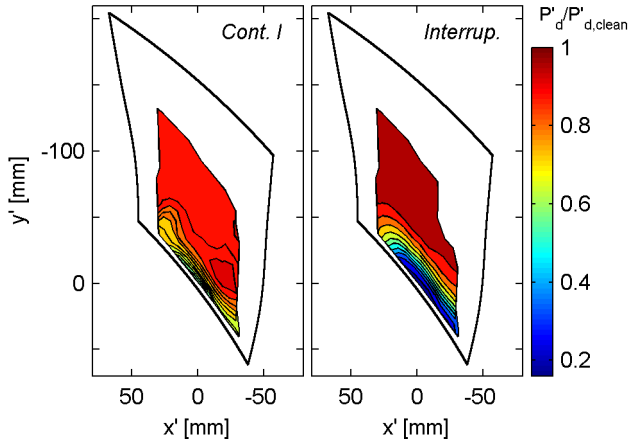

Figure 5.35: *Contours of ratio dynamic pressures in the presence of fins with respect to dynamic pressures in the 'clean' configuration, at 'plane 4'.*

The dynamic pressure distributions at *plane 3* used for the computation of the pressure loss coefficients $C_{p,3-4}$, were characterized by different mean values depending on the test configuration, but conserving the same relative distribution. Ratios of dynamic pressures with/without fins remained constant at about 0.88 within a 2% variation in the *continuous fins I* configuration, and at about 0.77 within a 4% for the *interrupted fins*. At *plane 4* in the absence of fins, the dynamic pressure is uniform within a 1%, with a slightly lower mean value than at *plane 3* except in the region affected by the splitter boundary layer. However, the arrays of fins forced the flow to redistribute, reducing the dynamic pressure in the region of the wakes, and increasing it to values higher than the correspondent at *plane 3* in the region over the fins, where dynamic pressures remained uniform within a 1%

as in the clean flow. Contours of ratios of dynamic pressure with/without fins at *plane 4* are represented in Fig.5.35. Values of the dynamic pressure ratio over the fins are close to 1, indicating that the mass flow per unit of area over the fins is similar for all the test configurations.

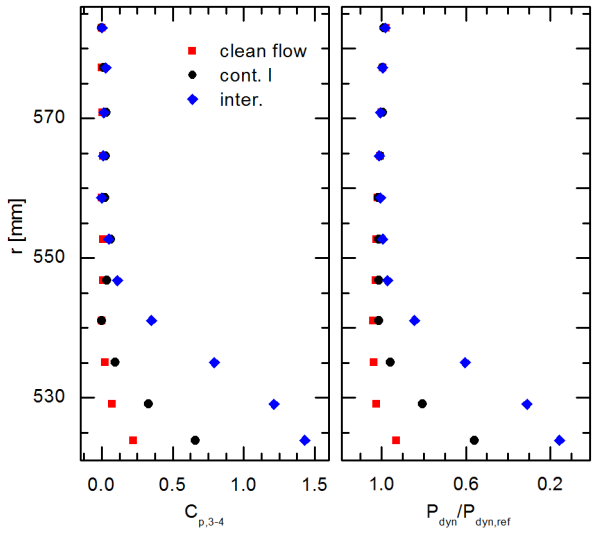

Figure 5.36: *Radial distributions of* $C_{p,3-4}$ *and* $P_{dyn,4}/P_{dyn,ref-4}$ *for the different geometries*

Radial profiles of pressure loss coefficients between *planes 3* and *4*, and dynamic pressures at *plane 4* made non dimensional with the correspondent value out of the wakes region, are represented in Fig.5.36. The pressure loss coefficient in the *continuous fins I* configuration decreased to about 10% at 15 mm (fins height) from the splitter . The radial depth of the pressure losses was higher in the *interrupted fins* configuration (fins height 17.5 mm) reflecting values of 80% and 40% at 13 and 20 mm from the splitter surface respectively. The radial profiles of dynamic pressure deficits present a similar evolution. The flow downstream of the *continuous fins I* losses about 30% of its free flow dynamic pressure over the splitter, which is nearly recovered at approximatively 15 mm. The deficit close to the splitter for the *interrupted fins* is about 85% and the dynamic pressure does not approach its free flow until a radial height of 25 mm.

The development along the splitter of the total pressure disturbances created by the fins is analyzed in Fig.5.37 in terms of total pressure deficits at *planes 4* and *5* with respect to the inlet, relative to the same total pressure deficits in the absence of fins, $Pr_{d,j}$ Eq.5.5. Contour plots are scaled with the maximum value of $Pr_{d,j}$ obtained for both planes and configurations,

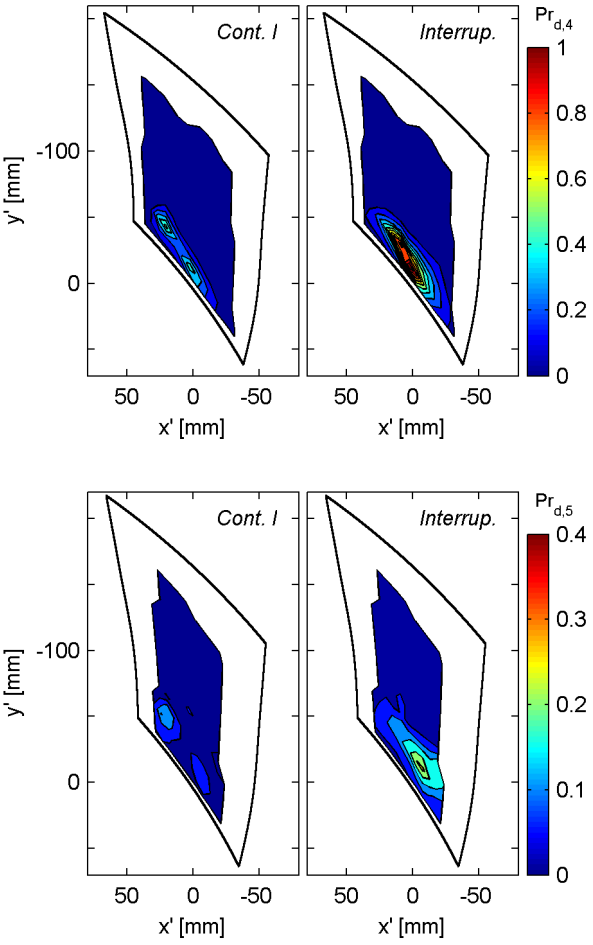

Figure 5.37: *Contours of total pressure deficit ratio with respect to the clean bypass flow. Top: plane 4. Bottom: plane 5.*

which corresponds to *plane* 4 and *interrupted fins*. Low ratios close to the splitter and lateral walls correspond to the region affected by pressure losses within the boundary layer in the *clean* configuration. Higher ratios indicate an increase of the total pressure deficit in the wakes of the fins. Maximum values obtained in the *interrupted fins* configuration are 60% higher than the those of the *continuous fins I*, at *plane* 4. Pressure deficit ratios computed following this procedure were equivalent for both *continuous fins I* and *continuous fins II* configurations. At *plane 5* in the case of the *continuous fins I*, the growing of the boundary layer in the *clean* configuration, in combination with the dissipation of the wakes towards the splitter, results in low pressure deficit ratios. However, ratios about 25% of the maximum values at *plane 4* are still visible for the *interrupted fins*.

Pressure losses ratio distributions computed for *continuous fins II* are equivalent to those of *continuous fins I*.

$$Pr_{d,j} = \frac{\left(\frac{P_{T,1}}{P_{ref}} - \frac{P_{T,j}}{P_{ref}}\right)_{fins}}{\left(\frac{P_{T,1}}{P_{ref}} - \frac{P_{T,j}}{P_{ref}}\right)_{clean}} \tag{5.5}$$

5.3 Bypass flow heat exchangers impact on turbofan engines

An estimative analysis of the impact of the type of heat exchangers investigated on current turbofan engines was performed based on their experimental aerodynamic and thermal characterizations.

5.3.1 Aerodynamic impact

Comparison of experimental measurements in the presence of the heat exchangers and in the conventional bypass flow permitted analyzing the aerothermal flow perturbations introduced by the different fin array configurations tested. In particular, total pressure balances between the flow upstream and downstream of the heat exchangers expressed in terms of non-dimensional pressure loss coefficients can be directly used to evaluate the global aerodynamic effects caused by this type of heat exchangers on the turbofan bypass flow. To this purpose we have considered the radial distributions of pressure loss coefficients between measurement *planes 3* and *4* ($C_{p,3\text{–}4}$), as well as the radial distributions representing the flow properties at *plane 3*. Mass flow averaged radial distributions of loss coefficients for the different test configurations were computed and extrapolated to the full annular bypass duct. The calculations were based on the real engine geometry in which the present investigation was focused, and were extended to higher bypass ratio engines based on the same core diameter. The increase of global bypass flow pressure losses with respect to the losses on the conventional configuration is represented in Fig. 5.38 for the test configuration *continuous fins*

I. Pressure losses for higher radial positions than the ones covered in the wind tunnel were considered constant and equal to 0.5%. For bypass ratios higher than 8 the total pressure loss increase is estimated to be lower than 45%. Estimated total pressure loss increases were significantly higher for the test configuration *interrupted fins*. For BPR higher than 9 the increase was lower than twice the pressure loss in the absence of heat exchangers, and about 2.7 times higher for BPR 8.

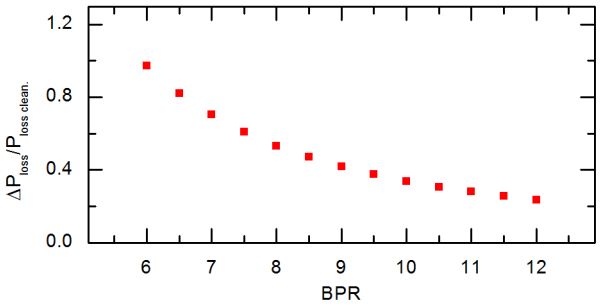

Figure 5.38: *Estimated bypass flow pressure loss increase with respect to conventional bypass flow losses, for 'continuous fins I' heat exchanger configuration and different BPR.*

This simplified calculation was evaluated based in a measurement plane close downstream of the heat exchanger. More accurate estimations can be obtained for a given engine considering the particular bypass duct geometry, in particular the length of the bypass duct between the inlet fan and the exit nozzle vanes, and the flow angle perturbations downstream of the heat exchanger. Results obtained for cruise flow regime at zero altitude can be extrapolated to different operational points of the flight envelope provided the influence of the variation of the flow parameters driving the dissipative effects is taken into account (viscosity, turbulence, Reynolds).

5.3.2 Thermal impact

From the thermal point of view, the cooling capacity and the thermal performance of finned heat exchangers were evaluated based on the results from the experimental thermal investigation, and information regarding oil circuit characteristics and cooling demands. High cooling solicitations are characteristic of take off conditions, which are aggravated in hot environments and at maximum engine power. For the estimation of the thermal performances of the heat exchanger, conductive heat fluxes within the heat exchanger were numerically resolved by means of finite element methods on a simplified 3D heat exchanger model, those used for the experimental characterization. The invariant descriptors h_{ad} and T_{ad} are representative of the convective heat transfer on the heat exchanger under the nominal flow conditions, and can

be used for heat flux analysis with different thermal boundary conditions. The boundary conditions on the air side imposed for the steady heat transfer simulations were the adiabatic heat transfer coefficients, both on the lateral and bottom surfaces, and a total flow temperature of 364K. At the oil side force convection was assumed, considering as typical values for the lubrication oil [10, 11]: oil at 433K, flow velocity 1 m/s, and heat transfer coefficient about 2000 W/m^{2}K.

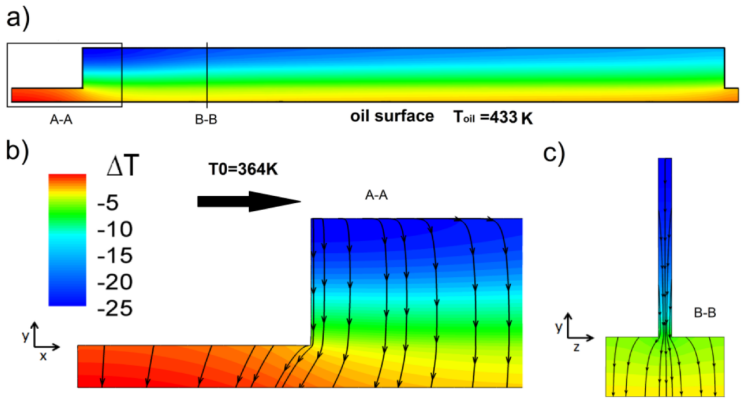

Figure 5.39: *Computed temperature variation on a fin with respect to the maximum temperature within the fin ($\Delta T = T - T_{max}$): a) on a longitudinal central cut of of the fin, b) detailed view (A-A) of the longitudinal cut, c) on a transversal cut (B-B) of the fin. Heat conduction vectors (with negative sign) are represented in b) and c).*

Figure 5.39 displays the temperature field within a heat exchanger fin in terms of temperature differences with respect to the maximum temperature attained in the solid domain, T_{max}=396K. The figure includes the temperature field on a longitudinal cut at the center of the fin (a), a detailed view of the longitudinal cut in the region of the fin leading edge (b), and the temperature distribution with a transversal fin cut (c). The heat flux vectors (of negative sign) are superimposed to the temperature field in the representations in (b) and (c). A large temperature gradient is observed along the fin height with maximum ΔT of 25 K registered at the fin leading edge. Gradients in longitudinal direction are small in comparison with vertical gradients.

The global heat flux released by the wet surfaces to the flow was computed by integration of the convective heat flux along the fin. The fin's thermal efficiency (Eq.5.6) can be calculated as the ratio between the heat flux fin/flow and the hypothetical heat flux that would be released if the temperature through the fin would be constant and equal to the base surface (T_b), resulting in the largest possible heat flux value. The base surface

was computed as the average over the full base surface exposed to the flow, while T_0 was the imposed total flow temperature. The fin efficiency for the thermal boundary conditions considered was 46%.

$$\eta = \frac{Q}{(T_b - T_0) * A_w * h} \tag{5.6}$$

The computed value of the heat flux oil/fin through the bottom of the heat exchanger allows to make some general estimations on the cooling capacity that the heat exchanger provides to the engine. The obtained surface average heat flux oil/fin was about 82 kW/m^2, which extrapolated to the full annulus and engine geometry investigated represents a total cooling capacity of 65 kW. The two major heat to oil contributions on a turbofan come from the loads to the lubrication oil circuit and the electrical heating. For a civil turbofan of 80 kN thrust a representative value of the lubrication oil heat loads can be considered about 55kW [10]. Among the mechanical components demanding the highest heat removal Streifinger mentioned the bearings (40%) and the gear boxes (32%). The component of the electrical system introducing highest thermal loads is the Integrated Drive Generator. Typical heat rejection values for a 90 kVA IDG can be estimated about 30 kW [10]. Considering the cooling capacity estimated from the numerical computations under the examined conditions, the heat exchanger could provide a 76% of the oil cooling demand required by the lubrication system and IDG during take off.

The efficiency and cooling capacity of the heat exchangers is function of the aerothermal properties of the bypass flow, which vary along the aircraft flight envelope due to the variation of altitude and flight velocity. The effects of altitude and flight velocity compete on their influence on the cooling capacity. Increasing the flow velocity at constant altitude causes an increase of the total bypass flow temperature and thus reduces the convective heat flux. However the convective heat transfer increases with the increase of velocity. With increasing flight level at constant velocity the air temperature decreases, however the lower air density and pressure reduces the convective capacity of the flow.

In order to estimate the sensitivity of the heat exchanger to different flight conditions a methodology was proposed that makes use an approximative correlation relating heat transfer coefficients for different flow properties, a turbofan engine model and the numerical heat conduction solver.

The adiabatic heat transfer coefficients determined from the experiments are not longer valid for changing flow conditions or flow properties. However, assuming for a turbulent flow a Nusselt number correlation with Reynolds and Prandtl numbers of the form $Nu \propto Re^{4/5} Pr^{1/3}$, the hypothesis expressed by Eq.5.7. can be made for the ratio of heat transfer coefficients during flight and those of the experiments, given than the geometrical characteristics are the same. The conventional definition of heat transfer coefficient was employed for the present estimative analysis, based on a bulk total

flow temperature as reference.

$$\frac{h_{eng}}{h_{exp}} = \frac{[(\frac{\rho V}{\mu})^{4/5} Pr^{1/3} K_f]_{eng}}{[(\frac{\rho V}{\mu})^{4/5} Pr^{1/3} K_f]_{exp}} \tag{5.7}$$

The bypass flow characteristics representative of the different operational points were derived from turbofan engine model, with a bypass ratio of 6, provided by the software GasTurb®. This model computes the aerothermal flow characteristics at different sections of the engine at design and off-design conditions. A certain flight envelope was imposed to determine the bypass flow properties at certain altitudes and velocities. The output of this program allowed estimating the new heat transfer coefficients based on the experimental results, and the characteristic flow temperature required to estimate the convective heat transfer heat exchanger/bypass flow.

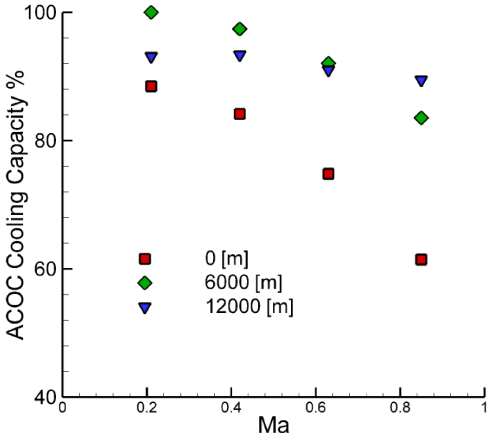

Figure 5.40: *Heat exchanger cooling capacity at different altitudes and flight Mach numbers with respect to maximum values computed.*

For the different flight conditions and correspondent heat transfer characteristics, the heat fluxes within the heat exchanger model were computed by means of the finite element solver. The thermal boundary conditions on the oil/heat exchanger boundary were kept constant, equal to those used for the experimental flow conditions. For each computation the heat flux oil/heat exchanger was obtained and used to compare the sensitivity of the cooling capacity to the flight conditions. The results are presented in Fig.5.40 where the values are normalized by the maximum cooling capacity computed.

At sea level the results show a cooling deficit with increasing flight speeds about 30% from Mach 0.2 to Mach 0.8, showing the major role of the increase of total flow temperature. The negative influence of flight velocity

vanishes with increasing flight altitudes. At the highest altitude considered, the cooling capacity is almost constant for the different Mach numbers.

This approximative sensitivity analysis confirms that the conditions experimentally reproduced were the most adverse from the point of view of the flow cooling capacity (cruise conditions and zero altitude). Thus, the validity of the design during the flight envelope is ensured if the performance derived from the experiments is satisfactory. It also proves the limited sensitivity of the heat exchanger during a commercial flight envelope. From comparison of results at 0 m-0.2 Mach, 6000 m-0.5 Mach and 1200 m-0.8 Mach, the cooling capacity variation is lower than 10% of the maximum cooling capacity computed during this analysis.

Chapter 6

Conclusions

The use of air/oil heat exchangers introducing minimum flow perturbations while maximizing the thermal exchange, represents an improvement on the lubrication oil thermal capacity. This would limit the detrimental effects of high fuel thermal loading, and would eliminate the need of existing plate/-tube heat exchangers with adverse aerodynamic effects. However it is with the development of future turbofans that the maximum thermal capacity in current oil system configurations becomes saturated and new heat removal solutions turn into imperative. The present research studied the aerothermal effects in surface integrated finned air/oil heat exchangers immersed in the bypass flow of a turbofan. Two main objectives have been pursued: the development of engine testing methods alternative to flight testing, and the analysis of the interaction between the transonic bypass flow and finned heat exchangers. The originality of both commitments provides genuine grounds for future developments in engine bypass flows and heat exchangers on high velocity flows, as well as design basis for high fidelity flow reproduction and experimental tools. The main achievements and findings obtained during this investigation are discussed in two blocks, addressing the two master goals.

The development of ground testing methods to investigate turbofan bypass flow involved the design of a new experimental facility able to reproduce the engine bypass flow environment. The main considerations justifying the wind tunnel design and methods employed can be synthesized in the following:

- The most critical conditions for the ACOC investigated, defined the type of flow to be reproduced: Cruise engine operational point at take off ambient conditions (zero altitude). To address the aerothermal phenomena of the transonic flow interaction with the heat exchangers, the precise replication at the correct Mach and Reynolds numbers of the three dimensional flow structure was the main design objective . Annular sector test sections represent an intermediate state between linear and annular test sections, allowing the replication of engine radial pressure gradients with testing costs comparable to those of linear test sections. The uniqueness of the present annular sector test section lies in the significantly larger dimensions of the research domain. An intermittent wind tunnel with atmospheric exhaust, driven by pres-

surized air at ambient conditions and controlled by a regulation valve at its inlet, met the design requirements.

- The described design methodology can be applied to any wind tunnel design when precise flow reproduction is required. The design followed different steps from zero-dimensional analysis of the complete wind tunnel to precise component optimization based on 2D and 3D CFD analysis. The applied zero dimensional modeling can also be used as a tool to predict overall wind tunnel performances.

- Special attention was focused on the optimization, by means of iterative CFD simulations, of the inlet guide vanes, the test section, and the exhaust duct. The strategy to reproduce a swirling 3D flow consists in considering the flow natural streamsurfaces as geometrical boundaries in a first approximation, and to subsequently optimize the solid boundaries to account for boundary layer growing and wall effects. This procedure was applied for the test section optimization in two steps: iterative axi-symmetric CFD analysis to define the hub and casing end-walls respecting the original splitter wall geometry; and from those flow results, iterative 3D CFD analysis optimizing the lateral walls.

Together with the wind tunnel design, the development of the most suitable measurement techniques for bypass flow characterization was essential to provide a ground engine testing alternative to flight testing. The measurement tools must provide high fidelity information for engine representative measurements. Hence developments were done in: specific design of the instrumentation; testing procedures; data reduction methods. The different probes were designed with the main objective to provide high fidelity measurements of the transonic three dimensional flow, while accounting for the constrains imposed by the wind tunnel operation (limited testing time) and geometry (blockage effects and probe accessibility), and the type of measurements aimed (maps of measurements with high spatial resolution). Special attention was paid to the development of two critical measurement techniques: multi-hole directional probes and fine wire thermocouple probes. The main outcomes are:

- Blockage effects caused by intrusive probes are a main concern in confined transonic flows. To study the influence of blockage on the measurements numerical 3D simulations were performed within the flow domain defined by the test section geometry, with and without the presence of a rake of five-hole probes. The position of the rake in the numerical domain corresponded to the section of minimum flow area. The analysis was performed for the most adverse test case, considering a rake introducing more area blockage than the rake used during the

test campaigns. Under those critical conditions, the total pressure error was estimated of the same order than the uncertainty on the total pressure measurements.

- The methodology used in this investigation for the data reduction of the five-hole probe measurements overcomes the limitations of the traditional procedures based on four non-dimensional parameters, i.e: failure when calibration maps are distorted due to manufacturing imperfections, or problems with one of the five pressure readings. The technique used, proposed by Yasa and Paniagua [71] and adapted to the present application, is a robust procedure able to deal with the previous limitations. It makes use of six non dimensional parameters, and it is based on a database of calibration points which are correlated one-by-one with each measurement data set. The sensitivity of the data reduction procedure to angle and Mach number variation based on the calibration database of the new five-hole probe was analyzed as well as the error associated to the method. It yielded errors lower than 0.4 deg. within the range ± 20 deg. and ± 30 deg. for pitch and yaw respectively.

- A new numerical methodology was proposed that outperforms previous experimental approaches to analyze the thermocouple response and the different sources of temperature error. The numerical procedure allows dissecting the influence of each error source, and provides an insight on the heat transfer balances and their driving parameters within the probe. The procedure can be applied for the design and characterization of new probes. The main advantages of the proposed methodology, in contrast with past experimental experiences, is the level of detail that can be achieved without the additional cost of sensors and set-up required to reproduce the test conditions, as well as the potential as a design tool. Geometrical/material optimization can be performed for a new design for a particular aerothermal application in less time and cost than current practices. Furthermore, the present procedure is suitable for probes exposed to harsh environments, onerous to be reproduced experimentally (hypersonic flows, combustor environments, accident modeling)

- The parameter l/l_c, collecting the influence of wire conductivity, length and diameter, and flow convective heat transfer, controls the temperature errors due to conductive heat fluxes between the thermocouple wires and their supports. Sensitivity analyses to the different parameters were performed providing general conclusions that can be used as design guidelines. Increasing wire conductivity and diameter increases the temperature error. Values of l/l_c lower than 5 must be avoided since in that case the temperature error has been demonstrated to be dominated by the characteristics and temperature conditions at the

support.

- The sensitivity of the thermocouple response time to design parameters was also evaluated. A numerical procedure was used to compute the transfer functions of different thermocouple configurations. In contrast with the conventional modeling of a thermocouple response by a first order system, it has been demonstrated that the order of the system modeling the response increases with the magnitude of the heat flux to the support, and thus with decreasing l/l_c values. For l/l_c values higher than 10, a second or third order response could be used for modeling the temperature evolution without loss in precision.

The aerothermal interaction of bypass flows with finned heat exchangers was experimentally characterized in the new test rig. Experimental and data reduction procedures were developed, providing an extensive flow database to analyze the flow modifications caused by the fins, and their cooling capacity. The main outcomes can be summarized in the following:

- A methodology was proposed to evaluate the convective thermal characteristics of the present type of heat exchangers. The methodology is based on experimental and numerical procedures, and can be applied to complex geometries and different experimental environments provided optical access is available. Surface temperature measurements are performed by infrared temperature imaging and processed by means of a three dimensional inverse heat conduction methodology. The procedure provided the adiabatic heat transfer convective characteristics that, as invariant descriptors for the flow conditions tested, were used with different thermal boundary conditions to analyze the cooling capacity of the heat exchangers.

- Comparison of flow measurements in the clean bypass flow and in the presence of three heat exchanger designs allowed understanding the different flow behaviors and quantifying the flow perturbations. The influence of the heat exchangers on the upstream flow conditions was limited to a small deviation towards the region over the fins. Downstream of the heat exchangers the flow was decelerated within the wakes and over accelerated in the part of the stream bypassing the fins. Significant differences were observed mainly between continuous and staggered arrays:
  - Two different geometries of continuous fins were tested with same fins height but different orientation and transversal section. The magnitude of the perturbations introduced was similar in both cases, and also the radial depth of the perturbations, equal to their height. Maximum flow deviations with respect to the clean flow were measured over the splitter and decreased rapidly in radial direction. However, circumferential periodic variations of

the flow variables corresponding to the individual fin wakes were identified exclusively downstream of the configuration with lower swirl angle. For the array with higher swirl angle, mixing between individual channel flows was observed, leading to slight higher losses. In the former configuration, the wakes patterns were seen to diffuse towards the splitter as the flow evolved downstream, resulting in a small increase of total pressure losses with respect to the clean flow affected by the growing of the splitter boundary layer.

  - The array of staggered fins showed significantly higher perturbations than the continuous fins, with high turbulent wakes and separated flow. The radial depth of the perturbations was higher than the fins' height and their strength still significant while developing downstream along the splitter.

- For the design of heat exchangers introducing minimum aerodynamic penalties, it is essential to avoid massive flow separation and large turbulent structures. Continuous fins demonstrated superior performances to this goal, even for fins orientations not matching the flow direction. For an engine with BPR of 8, the increase of pressure losses associated to the use of finned heat exchangers with respect to estimated losses on the absence of the fins, is lower than 45%.

- Thermal analysis based on the convective heat transfer results showed that for the flow conditions tested, arrays of continuous fins could provide about the 76% of the lubricant and IDG oil cooling demand during take off of a conventional civil turbofan of 80 kN thrust. Extrapolation of the thermal behavior to the different bypass flow conditions during a typical commercial aircraft mission, showed a low sensitivity of the cooling capacity to the flight envelope. The experimental environment was demonstrated to represent the most adverse conditions for the thermal performances, ensuring the validity of a design with satisfactory experimental cooling capabilities.

This work provides a significant scholar contribution relevant to the aerothermal investigation of surface finned heat exchangers on turbofan bypass flows, vital for the development of future aeroengines. The potential of the thermal capabilities of this new concept to cover the increasing cooling demand of engine developments was demonstrated, as well as the possibility to minimize its aerodynamic penalties through an optimized design.

List of Figures

List of Tables

Bibliography

[1] J. Kurzke. Preliminary Design. In *Aeroengine design: From state of the art turbofans towards innovative architectures, LS*, April 9-12, 2013. 1

[2] N. Tantot. From turbofan to innovative architectures. In *Aeroengine design: From State of the art of turbofans towards innovative architectures, LS*, April 9-12, 2013. 1

[3] C. F. McDonald and D. G. Wilson. The utilization of recuperated and regenerated engine cycles for high-efficiency gas turbines in the 21st century. *Applied Thermal Engineering*, 16, Issues 8-9:635–653, 1996. 1

[4] R. Andriani and U. Ghezzi. Influence of Heat Recovery and Intercooling on Turboprop Engine Behaviour. *International Journal of Turbo & Jet-Engines*, 25:259–267, 2008.

[5] S. Boggia and K Rüd. Intercooled recuperated aero engine. *DGLR Paper*, 179:2004, 2004.

[6] G. Wilfert, J. Sieber, A. Rolt, N. Baker, A. Touyeras, and S. Colantuoni. New environmental friendly aero engine core concepts. *ISABE 2007*, 2007. 1

[7] Andreas Linke-Diesinger. *Systems of commercial turbofan engines: an introduction to systems functions*. Springer, 2008. 2

[8] C. Zähringer, K. Stastny, and S. Ardey. Towards the Powerhouse for More Electric Aircraft–Dedicated Engine Concepts. In *19th International Symposium on Air Breathing Engines (ISABE 2009) Proceedings*, 2009. 2

[9] Rolls Royce. *The Jet Engine.* Rolls-Royce, 2005. 2

[10] H. Streifinger. Fuel/Oil System Thermal Management in Aircraft Turbine Engines. In *RTO-Applied Vehicle Technology Panel, Symposium on Design Principles and Methods for Aircraft Gas Turbine Engines*, Toulouse, 1998. 3, 130, 131

[11] M. Flouros and H. Streifinger. Lubrication Systems for Aircraft Gas Turbines Engines, New Component Developments for Future Applications. In *Lubrication Systems for Aircraft Gas Turbine Engines , Biarritz, France, STO-MP-AVT-188*, 2012. 3, 130

[12] C. E. Hughes. Aerodynamic performance of scale-model turbofan outlet guide vanes designed for low noise. *AIAA Paper*, 374:2002, 2002. 3

[13] R. P. Woodward, C. E. Hughes, and G. G Podboy. Aeroacoustic analysis of fan noise reduction with increased bypass nozzle area. In *11 th AIAA/CEAS Aeroacoustics Conference(26 th Aeroacoustics Conference), Monterrey, California*, pages 1–27, 2005. 3

[14] J. Yin, R. Hales, and P. Pilidis. 2-shaft high-bypass ratio turbofan performance calculation using a new 2-D fan model. In *37th AIAA/ASME/SAE/ASEE Joint Propulsion Conference, Salt Lake City, Utah*, 2001. 3

[15] W. N. Dawes. A comparison of the measured and predicted flow field in a modern fan-bypass configuration. *Journal of Turbomachinery*, 115:273, 1993. 3

[16] E. M. Sparrow and V. B. Grannis. Pressure Drop Characteristics of Heat Exchangers consisting of Arrays of Diamond-Shaped Pin Fins. *International Journal of Heat and Mass Transfer*, 34:589–600, 1991. 4

[17] V. B. Grannis and E. M. Sparrow. Numerical Simulation of Fluid Flow Through an Array of Diamond-Shaped Pin Fins. *Numerical Heat Transfer, Part A: Applications*, 19:381–403, 1991. 4

[18] D. E. Metzger, C. S. Fan, and S. W. Haley. Effects of Pin Shape and Array Orientation on Heat Transfer and Pressure Loss in Pin Fin Arrays. *Journal of Engineering for Gas Turbines and Power*, 106:252–257, 1984. 4

[19] T. Ota and H. Nishiyama . Heat Transfer and Flow Around an Elliptic Cylinder. *International Journal of Heat and Mass Transfer*, 27:1771–1779, 1984. 4

[20] Q. Li, Z. Chen, U. Flechtner, and H. J. Warnecke. Heat Transfer and Pressure Drop Characteristics in Rectangular Channels with Elliptic Pin Fins. *International Journal of Heat and Fluid Flow*, 19:245–250, 1998. 4

[21] Z. Chen, Q. Li, D. Meier, and H. J. Warnecke. Convective Heat Transfer and Pressure Loss in Rectangular Ducts with Drop-shaped Pin Fins. *Heat and Mass Transfer*, 33:219–224, 1997. 4

[22] E. M. Sparrow and T. J. Beckey. Pressure Drop Characteristics for a Shrouded Longitudinal-Fin Array with Tip Clearance. *ASME Journal of Heat Transfer*, 103:393–395, May 1981. 4

[23] R. S. Lee, H. C. Huang, and W. Y. Chen. A Thermal Study of Extruded Type Heat Sinks in Considering Air Flow Bypass Phenomenon. In *Proc. Sixth IEEE Semi-Therm Symposium*, pages 95–102, 1990. 4

[24] R. A. Wirtz, W. Chen, and R. Zhou. Effect of Flow Bypass on the Performance of Longitudinal Fin Heat Sinks. *ASME Journal of Electronic Packaging*, 116:206–211, 1994. 4

[25] H. Jonsson and B. Moshfegh. Modeling of the Thermal and Hydraulic Performance of Plate Fin, Strip Fin, and Pin Fin Heat Sinks - Influence of Flow Bypass. In *Proc. 2000 Intersociety Conf. on Thermal Phenomena (ITherm 2000)*, pages 185–192, Las Vegas, May 2000. 4

[26] S. Lee. Optimun Design and Selection of Heat Sinks. In *IEEE Transactions on Components, Packaging and Manufacturing Technologies*, volume 18, pages 812–817, December 1995. 4

[27] R. Simons and R. Schmidt. A simple Method to Estimate Heat Sink Air Flow Bypass. *Electronics Cooling*, 3(2):36–37, May 1997.

[28] M. A. Butterbaugh and S. S. Kang. Effect of Airflow Bypass on the Performance of Heat Sinks in Electronic Cooling. *Advances in Electronic Packaging*, 10:843–848, 1995. 4

[29] D. Bajusz, A. Cornet, J. Friedel, and N. Raimarckers. Air-Oil Heat Exchanger placed at the Location of the Air Separator Nose of a Turbojet, and a Turbojet Including such an Air-Oil Heat Exchanger. TechSpace Aero S.A., Milmort (BE), US2009/0165995A1, Jul. 2, 2009. 4

[30] A. Cornet, N. Raimarckers, and D. Bajusz. Heat Exchange System in a Turbomachine. TechSpace Aero S.A., Milmort (BE), Pub. No.: US 2009/0159246 A1, Jun. 25, 2009.

[31] B. Olver, A. Ciampa, R. Marrano, R. Trepanier, S. Lamarre, M. Bernard, and P. Germain. Turbofan Bypass Duct Air Cooled Fluid Cooler Installation. Pratt & Whitney Canada Corp. (CA), Pub. No.: US 2008/0053059 A1, Mar. 6, 2008.

[32] M. G. Anderson, W. E. Alford, M. L. Trego, R. Haugland, and A. K. Winstanley. Cooling Systems for Use on Aircraft. HoneyWell International, INC. Morristown, NJ (US), Pub. No.: US 2008/0314047 A1, Dec. 25, 2008.

[33] T. Wakeman. Compact Air-to-Air Heat Exchanger for Jet Engine Application. The United State of America as represented by the Secretary of the Air Force, Washington, D.C. (US), Pub. No.: US 004187675, Feb. 12, 1980.

[34] E. Elovic. Cooling Air Cooler for a Gas Turbofan Engine. General Electric Company, Cincinnati, Ohio (US), Pub. No.: US 004254618, Mar. 10, 1981.

[35] A. Vermejan, P. Daiber, S. Mortosa, and M. Taylor. Gas Turbine Engine Fan Cooled Heat Exchanger. General Electric Company, Cincinnati, Ohio (US), Pub. No.: US005269135A.

[36] V. Bruno, B. Olver, and A. Logan. Bypass Duct Fluid Cooler. Pratt & Withney Canada Corp., Longueuil (CA), Pub. No.: US 007377100 B2, May 27, 2008. 4

[37] H. J. Gladden and J. W. Gauntner. Experimental verification of film-cooling concepts on a turbine vane. ASME Paper 75-WA/GT-21, NASA. Glenn Research Center, 1975. 9

[38] S. H. Wiers and T. H. Fransson. A new Annular Sector Cascade test facility to investigate Steady State Cooling Effects. In *Measuring Techniques for Transonic and Supersonic Flows in Cascades and Turbomachines*, 1998. 9

[39] S. H. Wiers and T. H. Fransson. Experimental Investigation of the Periodicity in a sector of an Annular Turbine Cascade. In *Measuring Techniques for Transonic and Supersonic Flows in Cascades and Turbomachines*, 2000.

[40] S. H. Wiers, T. H. Fransson, and U. Radeklint. Flow Field Measurements in a Cold Flow Annular Sector Turbine Cascade Test Facility and an Annular Sector Cascade Test Facility Operating at Near-Engine Conditions. In *ASME TURBOEXPO*, 2001. 9

[41] D. M. Vogt and T. H. Fransson. A new turbine cascade for teromechanical testing. In *16th Symposium on Measuring Techniques in Transonic and Supersonic Flows in Cascades and Turbomachines, Cambridge, UK*, 2002. 9

[42] T. Povey, T. V. Jones, and M. L.G. Oldfield. On a Novel Annular Sector Cascade Technique. *Journal of Turbomachinery*, 129:175–183, 2007. 9, 23

[43] S. Luque and T. Povey. A Novel Technique for Assessing Turbine Cooling System Performance. *Journal of Turbomachinery*, 133(3):031013 (9 pages), November 2010. 9

[44] A. Pope and K. L. Goin. *High-Speed Wind Tunnel Testing.* John Wiley & Sons, Inc., 1965. 12

[45] Alan Pope and J. J. Harper. *Low Speed Wind Tunnel Testing.* John Wiley & Songs, 1966.

[46] R. C. Pankhurst and D. W. Holder. *Wind Tunnel Technique*. Sir Isaac Pitman and Sons, 1952. 12, 23

[47] *Aerodynamics of Wind Tunnel Circuits and their Components*, AGARD CP 585, 1997. 12

[48] W. T Eckert, K. W. Mort, and J. Jope. Aerodynamic Design Guidelines and Computer Program for Estimation of Subsonic Wind Tunnel Performance. Technical Report D-8243, NASA, 1976.

[49] J. Lukasiewicz. Development of Intermittent Wind Tunnel Technique. Technical report, National Aeronautical Establishment Ottawa, Canada, 1954. 12

[50] ESA. *ESPSS EcosimPro Libraries User Manual*. 13, 16

[51] G. B. Schubauer, W. G. Spangernberg, and P. S. Klebanoff. Aerodynamis Characteristics of Damping Screens. Technical report, NACA TN 2001, 1950. 14

[52] R. I. Loehrke and H. M. Nagib. Experiments on Management of Freestream Turbulence. Technical report, AGARD Report 598, September 1972.

[53] H. L. Dryden and I. H. Abbot. The Design of Low Turbulence Wind Tunnels. Technical report, NACA Report 940, 1949. 14

[54] Y. T. Fung, G. S. Settles, and A. Ray. Microprocessor Control of High Speed Wind Tunnel Stagnation Pressure. *AIAA*, 2:429–435, 1988. 17

[55] C. H. Sieverding. Turbine Blade Design. Technical report, von Karman Institute for Fluid Dynamics, 2004. 18

[56] David Japikse. *Turbomachinery Diffuser Design Technology*. Concepts Eti; 2nd edition, 2000. 23

[57] B. Bottin. From Subsonic to Continuous Supersonic Wind Tunnels: Similarity laws, tunnel types and components, design consideration. CN 151, von Karman Institute for Fluid Dynamics, Rhode Saint Genese, Belgium, May 1998. 23

[58] D. W. Bryer and R. C. Pankhurst. Pressure Probe Methods for Determining Wind Speed and Flow Direction. Technical report, National Physical Laboratory, 1971. 30

[59] R. G. Dominy and H. P. Hodson. An Investigation of factors influencing the calibration of 5-hole cone and pyramid probes. *ASME Journal of Turbomachinery*, 115, n 3:531–519, 1993. 30, 31

[60] Gaillard, R. Calibration and use of an ONERA miniature five hole probe. In *Proc. of the 7th Sym. on Measuring Techniques for Transonic and Supersonic Flows in Cascades and Turbomachines*, 1983. 30

[61] S. Mukhopadhya, A. Dutta, A. N. Mullick, and B. Majumdar. Effect of Filve-hole Probe Tip Shape on its Calibration. *Journal of the Aeronautical Society of India*, 53, 4:271–277, 2001. 30

[62] E. M. Houtman and W. J. Bannink. Calibration and measuring procedure of a five hole hemispherical head probe in compressible flow. Technical report, TU. Delft Report. LR-585, 1989. 30

[63] G. Paniagua Prez. *Investigation of the Steady and Unsteady Performance of a Transonic HP Turbine*. PhD thesis, Universit Libre de Bruxelles, 2002. 31

[64] U. W Schaub, R. G. Williamson, J. P. Huot, and S. H. Moustapha. An Experimental Assesment of the Influence of Downstream Conditions on the Performance of a Transonic Turbine Nozzle of High Turning. *Journal of Turbomachinery*, 112, 1990. 32

[65] T. Depolt, F. Vinnemaier, and W. Koschel. Investigation of Minimazing Blockage Effects of Multi-hole Pressure Probes in Transonic Flow. In *Measuring Techniques for Transonic and Supersonic Flows in Cascades and Turbomachines*, 1990.

[66] S. P. Harasgama and K. S. Chana. Turbine Nozzle Guide Vane Exit Area Traversing in a Short Duration Light Piston Test Facility. In *Measuring Techniques for Transonic and Supersonic Flows in Cascades and Turbomachines*, 1990. 32

[67] J. Roux. *Experimental investigation of nozzle guide vanes in a sector of an annular cascade*. Licentiate thesis, ISBN 91-7283-672-5, KTH, Superseded Departments, Energy Technology, Stockholm, 2004. 34

[68] C. R. Gossweiler, P. Kupferschmied, and G. Gyarmathy. On fast-response probes: part 1technology, calibration, and application to turbomachinery. *ASME Journal of Turbomachinery*, 117 (4):611–617, 1995. 34

[69] A. J. Pisasale and N. A. Ahmed. Theoretical calibration for highly three-dimensional low-speed flows of a five-hole probe. *Measurement Science & Technology*, 13:1100–7, 2002. 34

[70] I. M. Milanovic and I. M. Kalkhoran. Numerical calibration of a conical five-hole probe for supersonic measurements. *J. Measurement Sci. Tech.*, 11(12):1812–8, 2000. 34

[71] T. Yasa and G. Paniagua. Robust procedure for multi-hole probe data processing. *Flow Measurement and Instrumentation*, 26:46–54, 2012. 34, 35, 137

[72] T. J. Dudzinski and L. N. Krause. Flow Direction Measurement with Fixed Position Probes. Technical report, NASA TM X-1904, 1969. 34

[73] B. A. Reichert and B. J. Wendt. A new algorithm for five-hole probe calibration data reduction and uncertainty analysis. Technical report, NASA Technical Memorandum 106458, 1994. 34

[74] R. W. Gallington. Measurement of very large flow angles with non-nulling seven-hole probe. In *Air Force Academy Aeronautics Digest,*, 1980. 34

[75] K. M. Arguelles Diaz, J. M. Fernandez Oro, E. Blanco Marigorta, and R. Barrio Perotti. Head geometry effects on pneumatic three-hole pressure probes for wide angular range. *Flow Measurement and Instrumentation*, 21:330–339, 2010. 34

[76] J. P Solano, V. Pinilla, G. P. Paniagua, S. Lavagnoli, and T. Yasa. Aero-thermal investigation of a multi-splitter axial turbine. *International Journal of Heat and Fluid Flow*, 32, Issue 5(ISSN: 0142-727X):1036–1046, October 2011. 44

[77] L. Villafañe, G. P. Paniagua, M. Kaya, D. Bajusz, and S. Hiernaux. Development of a transonic wind tunnel to investigate engine bypass flow heat exchangers. *Proc. IMechE, Part G: J. Aerospace Engineering*, 225, Issue 8:902–914, 2011. 46

[78] R. Vázquez and J. M Sánchez. Temperature measurement systems for low pressure ratio turbine testing. In *Proceedings of ASME Turbo Expo 2003, Power for Land, Sea, and Air*, June 16-19, 2003, Atlanta, Georgia, USA. 44

[79] G. E. Glawe, R. Holanda, and L. N. Krause. Recovery and radiation corrections and time constants of several sizes of shielded and unshielded thermocouple probes for measuring gas temperature. Technical report, Lewis Research Center, Cleveland, Ohio, 1978. 45, 46, 48

[80] J. Rom and Y. Kronzon. Small shielded thermocouple total temperature probes. Technical report, Institute of Technology, Israel, 1967. 46, 48

[81] T. M. Stickney. Recovery and time-response characteristics of six thermocouple probes in subsonic and supersonic flow. Technical Report NACA TN 3455, Lewis Flight Propulsion Laboratoty, Cleveland Ohio, 1955.

[82] D. Bradley and K. J. Matthews. Measurement of high gas temperatures with fine wire thermocouples. *Journal of Mechanical Engineering Science*, 10, Issue 4:299–305, October 1968.

[83] G. P Paniagua, R. Dénos, and M. Oropesa. Thermocouple probes for accurate temperature measurements in short duration facilities. In *Proceedings of ASME Turbo Expo 2002*, number GT-2002-30043, June 3-6, 2002. 45, 51

[84] M. D. Scadron and I. Warshawsky. Experimental determination of time constants and Nusselt numbers for bare wire thermocouples in high velocity air streams and analytic approximation of conduction and radiation errors. Technical Note NACA TN 2599, Lewis Flight Propulsion LAboratory, Cleveland, Ohio, 1952. 45, 51, 55

[85] S. J. Park and S. T. Ro. A new method for measuring time constants of a thermocouple wire in varying flow states. *Exp. in Fluids*, 21:380–386., 1996. 45

[86] M. N. R. Nina and G. P. Pita. Measurements of fluctuating gas temperatures using compensated fine wire thermocouples. In *Proc. 65th Propulsion and Energetic Panel Symposium. AGARD Conf. Bergen (Norway)*, 1985. 45

[87] C. Petit, P. Gajan, J. C. Lecordier, and P. Paranthoen. Frequency response of fine wire thermocouple. *J. Phys. E: Sci. Instrum*, 15:760–764, 1982. 45, 47, 60

[88] R. Talby, F. Anselmet, and L Fulachier. Temperature fluctuation measurements with fine thermocouples. *Exp. in Fluids*, 9:115–118, 1990. 45

[89] L. J. Forney and G. C. Fralick. Two wire thermocouple: Frequency response in constant flow. *Review of. Sci. Instruments*, 65, Issue 10:3252–3257, 1994. 45

[90] K. Farahmand and J. W. Kauffman. Experimental measurement of fine thermocouple response time in air. *Exp. Heat Transfer*, 14:107–118, 2001. 45

[91] Xu Qiang. Dynamic calibration of a fine-wire thermocouple using a rocket plume: assessment of the procedure. *Meas. Sci. Technology*, 14:1381–1386, 2003. 45

[92] A. Zeisberger. Total temperature probes for turbine and combustor apllications. In *20th ISABE Conference*, 2007. 45

[93] J. Nanigian and D Nanigian. A unique thermocouple to measure the temperatures of squibs, igniters, propellants and rocket nozzels. SPIE Paper 6222-3. Technical report, NANMAC Corporation, 11 Mayhew St., Framingham, MA USA 02701, 2006. 46

[94] H. I. H. Saravanamuttoo. Recommended practices for measurement of gas path pressures and temperatures for performance assessment of aircraft turbine engines and components. Advisory Report 245, AGARD Advisory Report No. 245, 1990. 46

[95] R. J. Moffat. Gas temperature measurement. *Temperature; Its Measurement and Control in Science and Industry. Applied Methods and Instruments*, 3, Part 2:553–571, 1961. 46, 52, 53, 54, 55

[96] H. C. Hottel and A. Kalitinsky. Temperature measurements in high velocity air streams. *Trans. ASME*, 67:A–25, 1945. 46, 52

[97] R. C. Warren. Design of thermocouple probes for measurement of rocket exhaust plume temperatures. Technical report, DSTO Aeronautical and Maritime Research Laboratory, Melbourne, 1994. 46

[98] L. G. Blevins and W. M. Pitts. Modeling of bare and aspirated thermocouples in compartment fires. *Fire Safety Journal*, 33:239–259, 1999. 46

[99] F. PJ. Incropera and D. P. DeWitt. *Fundamentals of Heat and Mass Transfer, 4th ed.* Prentice-Hall, Englewood Cliffs, NJ, 1999. 47

[100] A. Haas. Assessment and validation of intermittency transport equations for modeling hypersonic transition with CooldFluid and CFD++. Technical report, von Karman Institute for Fluid Dynamics, 2010. 49

[101] F. S. Simmons. Recovery corrections for butt welded stright wire thermocouples in high velocity, high temperature gas streams. Technical report, NACA RM-E54G22a, 1954. 52

[102] G. Glawe, F. S. Simmons, and T. M. Stickney. Radiation and recovery corrections and time constants of several chromel-alumel thermocouple probes in high temperature high velocity gas streams. Technical report, NACA TN-3766, 1956. 52

[103] A. J. Yule, D. S. Taylor, and N. A. Chigier. Thermocouple signal processing and on-line digital compensation. *Journal of Energy*, 2, Issue 4:223–231, 1978. 60

[104] D. C. Collis and M. J. Williams. Two dimensional convection from heated wires at low reynolds number. *Journal of Fluid Mechanics*, 6:357–384, 1959. 62, 69

[105] G. Paniagua and R. Dénos. Digital compensation of pressure sensors in the time domain. *Experiments in Fluids*, 32, Issue 4:417–424, 2002. 62

[106] R. Storn and K. Price. Differential evolution a simple and efficient heuristic for global optimization over continuous spaces. *Journal of Global Optimization*, 11:341359, 1997. 70

[107] R. J. Moffat. Whats new in convective heat transfer? *International Journal of Heat and Fluid Flow*, 19, 2:90–101, April 1998. 73

[108] D. E. Smith, J. V. Bubb, O. Popp, III Grabowski, T. E. Diller, J. A. Schetz, and W. F. Ng. Investigation of Heat Transfer in a Film Cooled Transonic Turbine Cascade, Part I: Steady Heat Transfer. In *ASME Paper, 2000-GT-0203*, 2000. 73

[109] V. Pinilla, J. P. Solano, G. Paniagua, and R. Anthony. Adiabatic wall temperature evaluation in a high speed turbine. *Journal of Heat Tranfer*, 134. Issue 9:1–9, September 2012. 73

[110] S. J. Thorpe, S. Yoshino, R. W Ainsworth, and N. W. Harve. Improved fast-response heat transfer instrumentation for short-duration wind tunnels. *Measurement Science and Technology*, 15, 9, 2004. 74

[111] T. V. Jones and Dep. of Engineering Science University of Oxford 1973. Schultz, D. L. Technical report. Heat transfer measurements in short-duration hypersonic facilities. AGARDograph 165, Department of Engineering Science, University of Oxford, Gt. Britain, 1973. 75

[112] J. F. L. Sousa, S. Lavagnoli, G. Paniagua, and L. Villafañe. Three-dimensional (3D) inverse heat flux evaluation based on infrared thermography. *Quantitative InfraRed Thermography Journal*, pages 1–15, 2012. 75, 78

[113] T. Astarita and G. Carlomagno. *Infrared Thermography for Thermo-Fluid-Dynamics*. Springer, 2012. ISBN 978-3642295072. 77

[114] M. J. Colaço, H. Orlande, and G. S. Dulikravich. Inverse and Optimization Problems in Heat Transfer. *J. of Braz. Soc. of Mech. Sci. & Eng.*, 28, N. 1:1–24, 2006. 77

[115] H. R. B. Orlande. Inverse Problems in Heat Transfer: New trends on Solution Methodologies and Applications. *Journal of Heat Transfer*, 134 (3), 2012. 77

[116] O. M. Alifanov. *Inverse Heat Transfer Problems*. Springer, 1994. 77, 78

[117] Y. Jarny, M. N. Ozisik, and J. P. Bardon. A general optimization method usind adjoint equation for solving multidimensional inverse heat conduction. *Int. J. Heat Mass Transfer*, 34:2911–2919, 1991. 77

[118] J. Sousa, L. Villafañe, and G. Panigua. Thermal analysis and modeling of surface heat exchangers operating in the transonic regime. *Energy (Acepted for publication)*. 80

[119] R. Dvorak . Transonic Flow Separation in Closed Curved Channels. Tech. Report AD-A280 728/7, Air Force, 1994. 94

[120] W. E. Carscallen and P. H. Oosthuizen. The effect of secondary flow on the redistribution of the total temperature field downstream of a stationary turbine cascade. In *AGARD CP-469*, 1990. 121

[121] W. E. Carscallen and J. P. Gostelow. Observations of vortex shedding in the wake from transonic turbine nozzle vanes. In *Proceedings of the 5th International Symposium on Transport Phenomena and Dynamics of Rotating Machinery, Kaanapali, Hawaii*, 1994. 121

[122] W. E. Carscallen, T. C. Currie, S. I. Hogg, and J. P. Gostelow. Measurement and computation of energy separation in the vortical wake flow of a turbine nozzle cascade. *Journal of Turbomachinery*, 121:703–708, 1999.

[123] W. E. Carscallen, J. P. Gostelow, D. R. Buttsworth, and T. V. Jones. Wide bandwidth stagnation temperature measurements in vortical flows behind turbine vanes . In *International Congress on Instrumentation in Aerospace Simulation Facilities, ICIASF 97 Record.*, 1997.

[124] J. R. Ackerman, J. P. Gostelow, A. Rona, and W. E. Carscallen. Energy separation and base pressure in the wake of a circular cylinder. In *Proceedings of the 32nd Fluid Dynamics Conference and Exhibit, St. Louis, MO, USA, 24-26 June,*, 2002.

[125] J. P. Gostelow, M. F. Platzer, and W. E. Carscallen. On Vortex Formation in the Wake Flows of Transonic Turbine Blades and Oscillating Airfoils. *Journal of Turbomachinery*, 128, Issue 3:528–535, 2005.

[126] J. P. Gostelow, A. Mahallati, W. E. Carscallen, and A. Rona. Encounters with Vortices in a Turbine Nozzle Passage. *International Journal of Rotating Machinery*, 2012. 121

[127] D. Ottolia. Investigation of energy separation in turbine blade wake flow. Technical report, VKI Report, 1999. 121

[128] C. H. Sieverding, D. Ottolia, C. Bagnera, A. Comadoro, J. F. Brouckaert, and J. M Desse. Unsteady Turbine Blade Wake Characteristics . *Journal of Turbomachinery*, 126:551–560, 2004. 121

[129] D. S. Miller. *Internal Flow Systems.* BHRA Fluid Engineering, 1978. 124

[130] A. J. Ward-Smith. *Pressure losses in ducted flows.* Butterworths, 1971. 124